

DETAILED DESIGN OF
SHELL-AND-TUBE HEAT EXCHANGERS
USING CFD

A THESIS SUBMITTED TO
THE GRADUATE SCHOOL OF NATURAL AND APPLIED SCIENCES
OF
MIDDLE EAST TECHNICAL UNIVERSITY

BY

ENDER ÖZDEN

IN PARTIAL FULFILLMENT OF THE REQUIREMENTS
FOR
THE DEGREE OF MASTER OF SCIENCE
IN
MECHANICAL ENGINEERING

SEPTEMBER 2007

Approval of the thesis:

**DETAILED DESIGN OF SHELL-AND-TUBE HEAT EXCHANGERS
USING CFD**

submitted by **ENDER ÖZDEN** in partial fulfillment of the requirements for the degree of **Master of Science in Mechanical Engineering, Middle East Technical University** by,

Prof. Dr. Canan Özgen
Dean, Graduate School of **Natural and Applied Sciences**

Prof. Dr. Kemal İder
Head of Department, **Mechanical Engineering Dept., METU**

Asst. Prof. Dr. İlker Tari
Supervisor, **Mechanical Engineering Dept., METU**

Examining Committee Members:

Prof. Dr. M. Haluk Aksel
Mechanical Engineering Dept., METU

Asst. Prof. Dr. İlker Tari
Mechanical Engineering Dept., METU

Asst. Prof. Dr. Almıla G. Yazıcıoğlu
Mechanical Engineering Dept., METU

Asst. Prof. Dr. Cüneyt Sert
Mechanical Engineering Dept., METU

Asst. Prof. Dr. Ayhan Yilmazer
Nuclear Energy Engineering Dept., Hacettepe University

Date: 06/09/2007

I hereby declare that all information in this document has been obtained and presented in accordance with academic rules and ethical conduct. I also declare that, as required by these rules and conduct, I have fully cited and referenced all material and results that are not original to this work.

Name, Last name : Ender Özden

Signature :

ABSTRACT

DETAILED DESIGN OF SHELL-AND-TUBE HEAT EXCHANGERS USING CFD

Özden, Ender

M.Sc., Department of Mechanical Engineering

Supervisor: Asst. Prof. Dr. İlker Tari

September 2007, 113 pages

Traditionally Shell-and-tube heat exchangers are designed using correlation based approaches like Kern method and Bell-Delaware method. With the advances in Computational Fluid Dynamics (CFD) software, it is now possible to design small heat exchangers using CFD. In this thesis, shell-and-tube heat exchangers are modeled and numerically analyzed using a commercial finite volume package. The modeled heat exchangers are relatively small, have single shell and tube passes. The leakage effects are not taken into account in the design process. Therefore, there is no leakage from baffle orifices and no gap between baffles and the shell. This study is focused on shell side flow phenomena. First, only shell side is modeled and shell side heat transfer and flow characteristics are analyzed with a series of CFD simulations. Various turbulence models are tried for the first and second order discretization schemes using different mesh densities. CFD predictions of the shell side pressure drop and the heat transfer coefficient are obtained and compared with correlation based method results. After selecting the best modeling approach, the sensitivity of the results to the flow rate, the baffle spacing and baffle cut height are investigated. Then, a simple double pipe heat

exchanger is modeled. For the double pipe heat exchanger, both the shell (annulus) side and the tube side are modeled. Last, analyses are performed for a full shell-and-tube heat exchanger model. For that last model, a small laminar educational heat exchanger setup is used. The results are compared with the available experimental results obtained from the setup. Overall, it is observed that the flow and temperature fields obtained from CFD simulations can provide valuable information about the parts of the heat exchanger design that need improvement. The correlation based approaches may indicate the existence of a weakness in design, but CFD simulations can also pin point the source and the location of the weakness.

Keywords: Computational Fluid Dynamics (CFD), shell-and-tube heat exchanger

ÖZ

HESAPLAMALI AKIŞKANLAR DİNAMIĞI YÖNTEMİ İLE GÖVDE-BORU TİPİ ISI DEĞİŞTİRİCİLERİNİN AYRINTILI TASARIMI

Özden, Ender

Yüksek Lisans, Makina Mühendisliği Bölümü

Tez Yöneticisi: Y. Doç. Dr. İlker Tarı

Eylül 2007, 113 Sayfa

Gövde-boru tipi ısı değıştirci tasarımı geleneksel olarak Kern yöntemi ve Bell-Delaware yöntemi gibi bağıntı temelli yaklaşımlar ile gerçekleştirilmektedir. Hesaplamalı Akışkanlar Dinamiği (HAD) yazılımlarında gerçekleşen gelişmelerle birlikte, küçük ısı değıştirciler HAD kullanılarak tasarlanabilmektedir. Bu tezde, sonlu hacim tekniği kullanan, ticari bir HAD yazılımı kullanarak gövde-boru tipi ısı değıştirci modellenmiş ve sayısal analizi yapılmıştır. Modellenen ısı değıştirciler göreceli olarak küçüktür ve tek gövde ve boru geçişi vardır. Tasarım sırasında sızıntı etkileri göz önünde bulundurulmamıştır. Plaka deliklerinde ve plaka-gövde arasında gerçekleşen sızıntı ihmal edilmiştir. Bu çalışma gövde tarafı akış olgusu üzerine yoğunlaşmıştır. Öncelikle, sadece gövde tarafı modellenmiş ve gövde tarafı ısı taşınım katsayısı ve akış özellikleri sistemli HAD analizleri ile incelenmiştir. Çeşitli türbülans modelleri, iki farklı eleman yoğunluğu kullanılarak birinci ve ikinci dereceden çözüm için denenmiştir. Gövde kısmı basınç düşümü ve ısı taşınım katsayısı için HAD sonuçları bağıntı temelli yöntem sonuçları ile karşılaştırılmıştır. En uygun modelleme kriterleri seçildikten sonra, akış debisi, plaka aralığı ve plaka yüksekliğinin sonuçlar üzerindeki etkisi incelenmiştir. Daha sonra plakasız, çift

borulu, basit bir ısı deęiřtirici modellenmiřtir. ift borulu ısı deęiřtirici iin hem gvde hem de boru kısmı modellenmiřtir. Son olarak, komple bir gvde-boru tipi ısı deęiřtirici iin analiz yapılmıřtır. Kk, laminar, eęitim amalı dzenek model olarak kullanılmıřtır. Sonu olarak, HAD analizlerinden elde edilen akıř ve sıcaklık bilgileri ısı deęiřtirici tasarımında geliřtirme isteyen noktaların belirlenmesi doęrultusunda deęerli bilgiler verebilmektedir. Baęıntı temelli yaklařımlar tasarımda var olan zayıf noktaları belirtmekte, fakat HAD simlasyonları tasarımda var olan zayıf noktaların yerlerini de belirtmektedir.

Anahtar Szckler: Hesaplamalı Akıřkanlar Dinamięi (HAD), gvde-boru tipi ısı deęiřtiriciler

To My Family

ACKNOWLEDGEMENTS

The author wishes to express his deepest gratitude to his supervisor Asst. Prof. Dr. İlker Tarı for his close guidance, invaluable supervision, encouragements and insight throughout the study.

I wish to express my sincere appreciation to Prof. Dr. Haluk Aksel for his understanding and help about using CFD laboratory.

The author would like to thank CFU International Trade & Services Co. LTD. members, for their cooperation in supplying data for the sample experimental data set for the miniature shell-and-tube heat exchanger.

The author would also like to thank his colleagues Mr. Hakan Mencek, Mr. Güneş Nakiboğlu, Mr. Ali Özgü Nursal, Mr. Emre Orhan and Mr. Bercan Siyahhan for their practical helps throughout the study.

The author gratefully thanks to his family for their continuous encouragement, understanding and support.

TABLE OF CONTENTS

ABSTRACT	iv
ÖZ	vi
DEDICATION	viii
ACKNOWLEDGEMENTS	ix
TABLE OF CONTENTS	x
LIST OF TABLES	xii
LIST OF FIGURES	xiv
LIST OF SYMBOLS	xvi
LIST OF ABBREVIATIONS	xxi
CHAPTER	
1. INTRODUCTION	1
1.1 Basic Design Procedure of a Heat Exchanger	3
1.2 Literature Survey	5
1.2.1 Porous Medium Model	6
1.2.2 Previous Studies.....	8
1.3 Analytical Calculation Methods	10
1.4 Motivation and Thesis Goals	11
1.5 Brief Outline	11
2. THEORETICAL BACKGROUND AND CFD MODELING.....	13
2.1 Governing Equations	13
2.2 CFD Modeling	14
2.2.1 Pre-Processing	15
2.2.2 Solver Execution	19
2.2.3 Post-Processing.....	25
3. HEAT EXCHANGER MODELING	27
3.1 Introduction.....	27
3.2 Sensitivity of the Results to Turbulence Model and Discretization .	27
3.2.1 Mesh Selection.....	28

3.2.2	Boundary Conditions	30
3.2.3	Turbulence Model	31
3.2.4	Other Modeling Choices.....	32
3.2.5	Results and Discussion	32
3.3	Effect of Baffle Spacing on Pressure Drop and Heat Transfer	40
3.3.1	Pre-processing	41
3.3.2	Results and Discussion	41
3.4	Effects of Baffle Cut on Pressure Drop and Heat Transfer	52
3.5	Double Pipe Heat Exchanger Design.....	56
3.5.1	Mesh Selection.....	58
3.5.2	Boundary Conditions	59
3.5.3	Other Modeling Choices.....	60
3.5.4	Results and Discussion	60
3.6	Conclusion.....	70
4.	FULL HEAT EXCHANGER SIMULATION	71
4.1	Introduction.....	71
4.2	Model Details	72
4.2.1	Mesh Selection.....	73
4.2.2	Boundary Conditions	75
4.2.3	Other Modeling Choices.....	76
4.2.4	Results and Discussion	76
5.	CONCLUSION	82
5.1	Comments on the Results.....	82
5.2	Recommendations for Future Work	83
	REFERENCES	85
	APPENDICES	
A.	Theoretical background about turbulence models	89
B.	Water Properties in the Simulation Range	94
C.	Details of non-uniform velocity profile	97
D.	Sample heat transfer coefficient calculation	99
E.	Sample analytical calculations	100
F.	Double pipe calculations	110

LIST OF TABLES

Table 3-1 Design parameters and fixed geometric parameters	28
Table 3-2 Meshing Details.....	29
Table 3-3 Results of the CFD analysis for different turbulence models and discretization order for $N_b = 6$	34
Table 3-4 Results of the analytical calculations for $N_b = 6$	37
Table 3-5 Percent differences between analytical calculations and CFD analysis	38
Table 3-6 Design parameters and fixed geometric parameters	41
Table 3-7 Results of the CFD analysis for $N_b = 6, 8, 10$ and 12	42
Table 3-8 Results of the analytical calculations for $N_b = 6, 8, 10$ and 12	43
Table 3-9 Percent differences between analytical calculations and CFD analysis for $N_b = 6, 8, 10$ and 12	44
Table 3-10 Results of the CFD analysis for $B_c = 25\%$	53
Table 3-11 Results of the analytical calculations for $B_c = 25\%$	54
Table 3-12 Percent differences between analytical calculations and CFD analysis for $B_c = 25\%$ and $B_c = 36\%$	55
Table 3-13 Predetermined geometric parameters	56
Table 3-14 Design parameters	58
Table 3-15 Mesh details.....	59
Table 3-16 Results of the CFD analysis for double pipe heat exchanger (for annulus mass flow rate of 1.39 kg/s)	61
Table 3-17 Results of the CFD analysis for double pipe heat exchanger (for annulus mass flow rate of 0.7 kg/s)	62
Table 3-18 Results of the CFD analysis for double pipe heat exchanger (without inlet and outlet nozzles).....	69
Table 4-1 Technical and geometrical details of the heat exchanger	72

Table 4-2 Sample experimental data of the miniature heat exchanger (The ambient temperature is not reported)	74
Table 4-3 Meshing details	74
Table 4-4 Comparison of Results of the Experimental data and CFD results ..	77

LIST OF FIGURES

Figure 1-1 Typical shell-and-tube-heat exchanger (adapted from [1]).....	2
Figure 1-2 Diagram indicating leaking paths for flow bypassing the tube matrix, through both the baffle clearances between the tube matrix and shell (adapted from [2]).....	3
Figure 1-3 Basic logic structure for process heat exchanger design.....	4
Figure 1-4 Sample control volume with tubes (adapted from [7]).....	6
Figure 2-1 The heat exchanger model with six baffles	16
Figure 2-2 Mesh from a vertical cut-plane.....	17
Figure 2-3 Boundary condition types	19
Figure 2-4 Node combining to form coarse grid cells	24
Figure 3-1 Grid examples: a) structured grid, b) unstructured grid (adapted from [20]).....	30
Figure 3-2 Example of a hex-core type tet-hybrid mesh (adapted from [20]).	30
Figure 3-3 Comparison of outlet temperature values	35
Figure 3-4 Comparison of heat transfer coefficient values	35
Figure 3-5 Comparison of shell side pressure drop values	36
Figure 3-6 Comparison of total heat transfer rate values.....	36
Figure 3-7 Bell-Delaware recommended segmental baffle cut values as a function of B/D_s ratio. SBC: segmental baffle cuts in no-phase-change flow; CV: baffle cuts applicable to condensing vapors (adapted from [15]).	40
Figure 3-8 Velocity (m/s) path lines for 6 baffles (1 kg/s mass flow rate).....	45
Figure 3-9 Velocity (m/s) path lines for 8 baffles (1 kg/s mass flow rate).....	46
Figure 3-10 Velocity (m/s) path lines for 10 baffles (1 kg/s mass flow rate) ..	46
Figure 3-11 Velocity (m/s) path lines for 12 baffles (1 kg/s mass flow rate) ..	47
Figure 3-12 Detailed representation of velocity (m/s) path lines for 6 baffles case.....	48

Figure 3-13 Velocity profile of the line passing through mid-plane of the compartment between first and second row of the tubes (for $N_b=6$)	49
Figure 3-14 Detailed representation of velocity (m/s) path lines for 8 baffles case.....	50
Figure 3-15 Velocity profile of the line passing through centers of the tubes of the first row (for $N_b=8$)	50
Figure 3-16 Velocity profile of the line passing through centers of the tubes of the first row (for $N_b =12$)	51
Figure 3-17 Velocity profile of the line passing through mid-plane of the compartment between first and second row of the tubes (for $N_b=12$)	52
Figure 3-18 Double pipe heat exchanger	60
Figure 3-19 Velocity (m/s) path-lines for analysis A-1	64
Figure 3-20 Velocity vectors (m/s) from middle of the annulus.....	65
Figure 3-21 Velocity data versus annulus diameter	66
Figure 3-22 Locations of the velocity data lines	66
Figure 3-23 Double pipe heat exchanger without inlet nozzles	68
Figure 4-1 Miniature shell-and-tube heat exchanger (adapted from [28])	71
Figure 4-2 Schematic diagram of the heat exchanger (adapted from [28])....	73
Figure 4-3 Boundary conditions.....	75
Figure 4-4 Temperature distributions for the two flow arrangements.....	78
Figure 4-5 Velocity (m/s) path lines for the co-current case	79
Figure 4-6 Velocity (m/s) path lines for the counter-current case	80
Figure 4-7 Velocity profiles at the shell inlet.....	81
Figure B-1 Density of water versus temperature	94
Figure B-2 Thermal conductivity of water versus temperature	95
Figure B-3 Viscosity of water versus temperature	95
Figure B-4 Specific heat capacity of water versus temperature	96
Figure B-5 Viscosity of water versus temperature (for ten intervals)	96

LIST OF SYMBOLS

x,y,z	Primary Cartesian coordinates (m)
Δp_{bi}	Pressure drop in an equivalent ideal tube bank (Pa)
Δp_c	Pressure drop in interior cross flow section (Pa)
Δp_e	Pressure drop in the entrance and exit sections (Pa)
Δp_f	Frictional pressure drop (Pa)
Δp_n	Nozzle pressure drop (Pa)
Δp_t	Total pressure drop (Pa)
Δp_w	Pressure drop in the window (Pa)
ΔT	Temperature difference (K)
ΔT_{lm}	Log mean temperature difference (K)
A	Surface area of a given control volume (m ²)
A_c	Cross flow area (m ²)
A_f	Area open to fluid flow (m ²)
A_{ff}	Surface area open to fluid flow (m ²)
A_n	Nozzle area (m ²)
A_o	Total heat transfer surface of the heat exchanger (m ²)
A_s	Bundle cross-flow area at the center of the shell (m ²)
A_{ss}	Surface area blocked by the solid (m ²)
B	Central baffle spacing (m ²)
B_c	Baffle cut (%)
C	Tube clearance (m)
C_{bh}	Constant of correction factor for bundle bypass effects for heat transfer
C_{bp}	Constant of correction factor for bundle bypass effects for pressure drop
c_p	Specific heat capacity (J/kg K)
d	Distance from the wall for near wall treatment (m)
D_e	Equivalent diameter (m)

D_{ctl}	The diameter of the circle through the centers of the tube located within the outermost tubes (m)
D_h	Hydraulic diameter (m)
D_i	Annulus diameter (m)
d_i	Tube inner diameter (m)
d_o	Tube outer diameter (m)
D_{otl}	The tube bundle circumscribed circle (m)
D_s	Shell size (m)
f	Friction factor
F	LMTD Correction factor
F_c	The fraction of number of tubes in pure cross flow between the baffle cut tips
f_i	The friction coefficient for an ideal tube bank
f_s	Surface permeability
F_{sbp}	The fraction of the bypass area to the overall cross flow area
f_v	Volumetric porosity
F_w	The fraction of number of tubes in one baffle window
G_b	Generation of turbulence due to buoyancy
g_i	Component of the gravitational vector in the direction i
G_k	Production of turbulence kinetic energy due to mean velocity gradients
G_s	Shell side mass velocity (kg/m ² s)
h	Heat transfer coefficient (W/m ² K)
h_{id}	The ideal tube bank-based heat transfer coefficient (W/m ² K)
J_l	Correction factors for baffle leakage effects for heat transfer
J_b	Correction factors for bundle bypass effects for heat transfer
J_c	Segmental baffle window correction factor
j_i	The Colburn j -factor
J_r	Heat transfer correction factor for adverse temperature gradient
J_s	Heat transfer correction for unequal baffle spacing at inlet and outlet
L	Heat exchanger length (m)
k	Thermal conductivity (W/m K)
	Kinetic energy of turbulent fluctuations per unit mass
L_{bb}	Shell diameter to tube bundle bypass clearance is (diametral) (m)

L_i	The ratio of inlet baffle spacing to central baffle spacing
L_o	The ratio of outlet baffle spacing to central baffle spacing
L_{sb}	Shell to baffle clearance (m)
L_{tb}	The clearance between tube outside diameter and baffle hole (m)
L_{wp}	The effective distance of penetration (m)
m	Mass flow rate (kg/s)
m_w	Shell-side flow mass velocity through segmental baffle window (kg/s)
N_b	Number of baffles
N_t	Number of tubes
N_{ic}	Number of tubes in cross-flow
N_{icc}	The number of effective rows crossed in one cross flow section
N_{icw}	The effective number of tube rows crossed
N_{tw}	The number of tubes in the window
Nu_b	Nusselt number
p	Pressure term
Pr_b	Prandtl number
Pr_t	Turbulent Prandtl number for energy
P_T	Tube pitch (m)
P_{Teff}	Effective tube pitch (m)
q	Heat transfer rate (W)
Q	Volumetric flow rate (m ³ /s)
Q_a	Heat absorbed (kW)
Q_e	Heat emitted (kW)
R	The gas constant (J/K mol)
R	Radius of the pipe (m)
R_l	Correction factors for baffle leakage effects for pressure drop
R_b	Correction factors for bundle bypass effects for pressure drop
Re	Reynolds number
R_s	Pressure drop correction factor for unequal baffle spacing
S	Scalar measure of the deformation tensor
S_b	The bypass area within one baffle (m ²)

S_e	Energy source term in energy equation
S_m	Cross flow area (m ²)
S_{Mx}	Momentum source term in the x direction
S_{My}	Momentum source term in the y direction
S_{Mz}	Momentum source term in the z direction
S_{sb}	Shell to baffle leakage area (m ²)
S_{tb}	Tube to baffle hole leakage area for one baffle (m ²)
S_w	Cross flow area through one baffle window (m ²)
S_{wg}	The gross window flow area (m ²)
S_{wt}	The segmental baffle window area occupied by the tubes (m ²)
T	Temperature (K)
T_{sav}	Average temperature of the shell-side (K)
U	Heat transfer coefficient (W/m ² K)
u	Velocity components in the x-direction
u_m	Average velocity in the tube side (m/s)
u_n	Average nozzle velocity (m/s)
u_n	The average velocity at the nozzle (m/s)
V	Control volume
v	Velocity components in the y-direction
V_c	Velocity at the centerline of the pipe (m/s)
V_f	Volume occupied by the solid in the control volume
V_s	Volume occupied by the fluid in the control volume
V_z	Axial velocity
w	Velocity components in the z-direction
ε	Viscous dissipation rate (m ² /s ³)
θ_{ctl}	The angle intersecting the circle through the centers of the outermost tubes (°)
θ_{ds}	The centiangle of the baffle cut intersection with the inside shell wall (°)
θ_{tp}	Tube layout characteristic angle (°)
μ	Dinamic viscosity (Pa s)
μ_t	Turbulent viscosity (Pa s)
μ_w	Dinamic viscosity at wall temperature (Pa s)

ν	Molecular viscosity (m ² /s)
ρ	Density (kg/m ³)
$T_{h,i}$	Hot side inlet temperature (K)
$T_{h,o}$	Hot side outlet temperature (K)
$T_{c,i}$	Cold side inlet temperature (K)
$T_{c,o}$	Cold side outlet temperature (K)
$C_{1\varepsilon}, C_{2\varepsilon}, C_{3\varepsilon}, C_{\mu}, C_1, C_2, \sigma_v$	Constants of transport equations
$C_{b1}, C_{b2}, C_{w1}, C_{w2}, C_{w3}, C_{v1}, \kappa$	Closure coefficients of transport equations
S_ε, S_k, S_v	User defined source terms of transport equations
f_{v1}, f_{v2}	Viscous damping function
Ω_{ij}	Mean rate-of-rotation tensor
σ_k	Turbulent Prandtl numbers for k
σ_ε	Turbulent Prandtl numbers for ε
β	Coefficient of thermal expansion
λ	Viscosity coefficient
Φ	Dissipation function
ϕ	Scalar symbol
\vec{F}_s	The surface force (N)
\vec{F}_b	The body force (N)
\vec{V}	Velocity vector
\vec{n}	The local unit normal vector to the surface

INDICES

h	hot
c	cold
i	inlet
o	outlet

LIST OF ABBREVIATIONS

CFD	Computational Fluid Dynamics
CPU	Central Processing Unit
FAS	Full Approximation Storage
FMG	Full Multigrid Initialization
LMTD	Log Mean Temperature Difference
RAM	Random Access Memory
RCM	Reverse Cuthill-McKee Method
SBC	Segmental Baffle Cuts
TEMA	The Tubular Exchanger Manufacturers Association

CHAPTER 1

INTRODUCTION

Shell-and-tube heat exchangers are used in a wide range of industrial applications. Their design process may be very complex due to various possible geometric arrangements of the shell side and resulting complicated flow structures. The Tubular Exchanger Manufacturers Association (TEMA) have been standardized various shell-and-tube heat exchanger components. A shell-and tube heat exchanger is divided into three main parts: the front head, the shell and the rear head. Various front and rear head types and shell types have been standardized by TEMA. Each part of the exchangers is described by letter codes. In a shell-and-tube heat exchanger design process, the TEMA standards are used together with the correlation based approaches. The TEMA standards and the standardized correlation based design methods somewhat simplifies the design process.

A shell-and-tube heat exchanger consists of a bundle of round tubes installed in a cylindrical shell. One fluid flows through the tubes, and the other fluid flows through the shell, over the tubes. Baffles are placed inside the shell to change the direction of the shell-side fluid, and to form cross-flow zones. In the TEMA standards, the most common type of shell is the E-type due to its simple geometry and ease of manufacturing. A schematic figure of a single tube pass E-type shell-and-tube heat exchanger with vertical baffles is shown in Figure 1-1 [1]. In the E-type shell, there is a single pass on the shell-side; the shell fluid enters at one end of the shell and leaves at the other end.

The shell side flow is very complicated in shell-and-tube heat exchangers due to many different leakage paths between the different flow zones. For single tube

pass shell-and-tube heat exchangers, four different streams are identified in the shell side as indicated in Figure 1-2 [2]. Stream B is the main cross flow stream in the shell flowing through the window zones. Because of the mechanical clearances, there are three different leakage streams present in the shell. Stream A is the baffle to tube leakage; the leakage flow through the clearance between the tubes and the baffle. Stream C is the bundle bypass stream which flows between the outermost tubes of the tube bundle and the shell. Stream E is the baffle to shell leakage; the leakage flow through the gap between the baffle and the shell. Streams A, C, and E are not as effective on the heat transfer as Stream B. Streams A and C are quite efficient, since the shell-side fluid is in contact with the tubes. On the other hand, Stream E encounters no heat transfer at all, since it flows through the baffles and the shell, where there are no tubes [3]. For different shell designs and sizes, importance of these flow paths may vary.

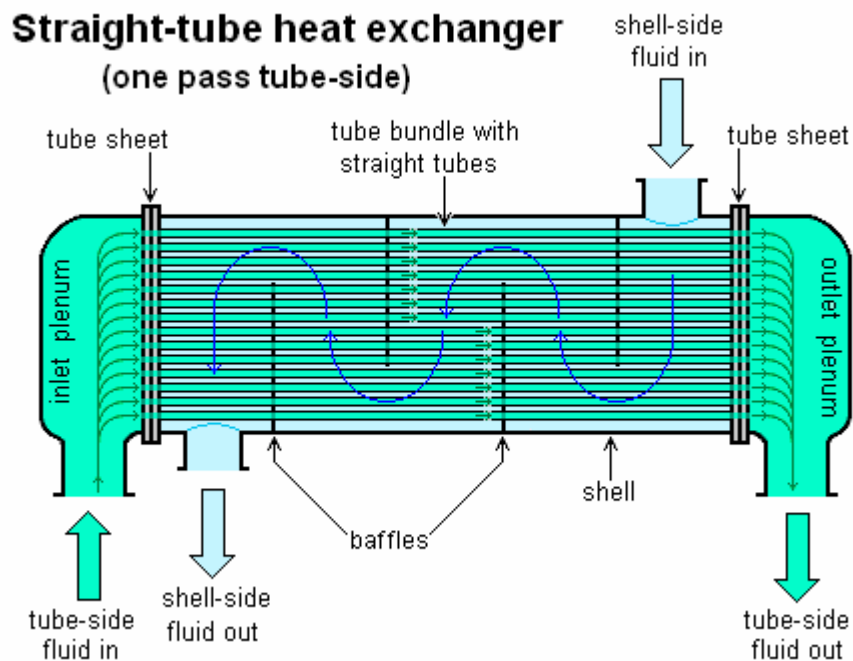


Figure 1-1 Typical shell-and-tube-heat exchanger (adapted from [1])

One should note that Figure 1-2 ideally represents the flow structure of the shell side flow. Actual flow streams mix and form different flow structures. Information about the turbulent flow structures on the shell-side is limited in the literature; as a result, shell-side flow analysis cannot be carried out exactly [4]. By using experimental testing, flow visualization techniques or Computational Fluid Dynamics (CFD) techniques the flow characteristics in a shell-and-tube heat exchanger could be visualized. Also, these methods may help to improve the quality of the final design.

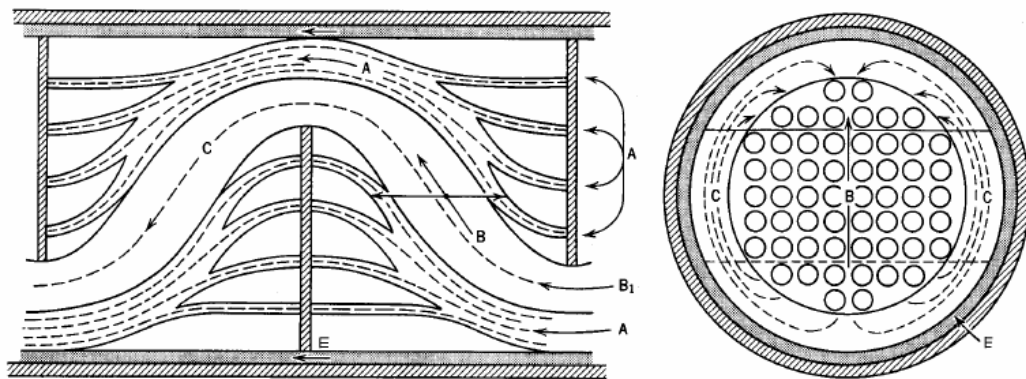


Figure 1-2 Diagram indicating leaking paths for flow bypassing the tube matrix, through both the baffle clearances between the tube matrix and shell (adapted from [2])

Although, the shell-and-tube heat exchanger design process is complex, if the basic design procedure discussed in the following part is carried out in an organized manner, it may not be as complicated as expected.

1.1 Basic Design Procedure of a Heat Exchanger

In general, a selected shell-and-tube heat exchanger must satisfy the process requirements within the design limitations. In Figure 1-3, the basic logical structure of the design steps of heat exchangers is presented. And the details of the basic logical structure are discussed below.

- First step is the problem identification. The design problem must be identified completely. Inlet and outlet temperatures, and pressures of the streams, flow rates, and fluid states must be determined in detail.
- Next step is the selection of the basic configuration of the heat exchanger.
- Then, the heat exchanger design parameters are tentatively selected. Preliminary estimate of the heat exchanger size can be made.
- Next step is the rating of the design. Rating is the computational process in which the thermal performance and the pressure drops for both streams are determined.
- After the rating step is completed, the next step is the evaluation of the design. In this step, pressure drops, outlet temperature values and the heat duty of the heat exchanger is examined. If the examined parameters are not acceptable, the design parameters should be modified. The design should be rated again until the required design criteria are met.
- And the final step is the mechanical design and costing.

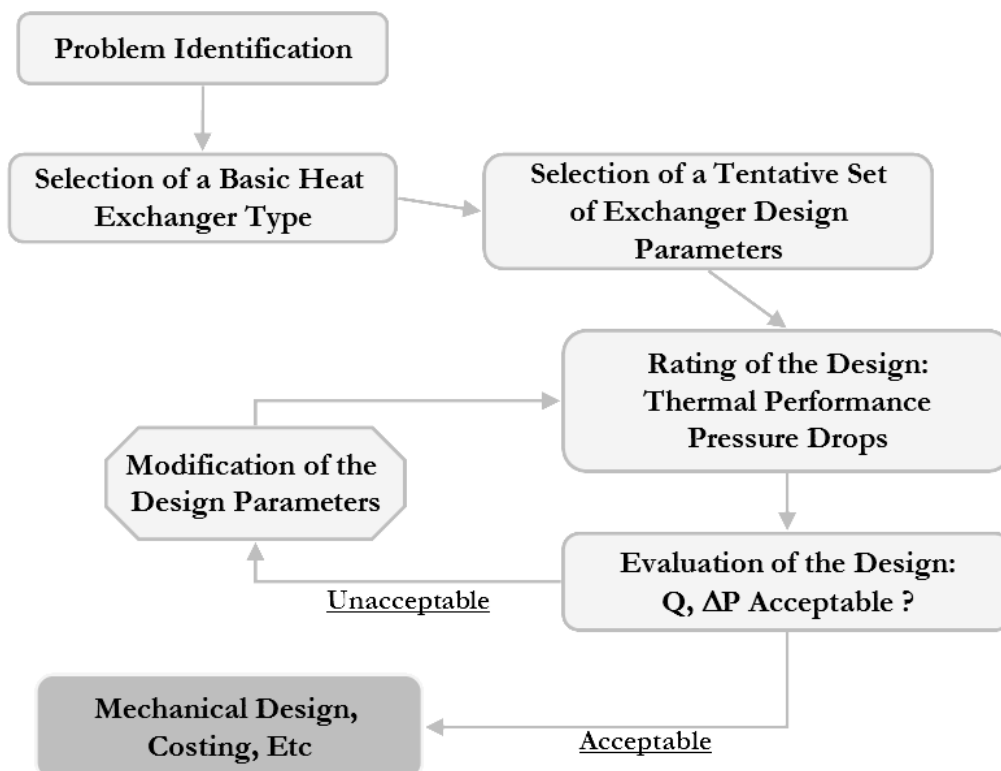


Figure 1-3 Basic logic structure for process heat exchanger design

1.2 Literature Survey

Detailed knowledge of flow phenomena is required in the design process of heat exchangers. By using experimental testing or computational techniques, this information can be obtained. But, experimental testing is usually very expensive and time consuming when compared with computational methods. Additionally, flow visualization techniques can also be used together with turbulence measurements during the design process. Nevertheless, in heat exchangers, it is very difficult to perform flow visualization. Among the computational methods, CFD techniques can assist as cost-effective research tools in shell-and-tube heat exchanger.

However, modeling shell-side fluid flow in a shell-and-tube heat exchanger is computationally very expensive. With increasing computational power of desktop computers, CFD simulations are getting faster. On the other hand, using ordinary computers, it is still very hard to perform simulations for a detailed model. In the previous works, simplified models of shell-and-tube heat exchangers are used.

Symmetry is one of the simplification methods that can be used in the shell-and tube heat exchanger design. Radial symmetry behavior of a tube arrangement in the shell geometry is one of the choices of simplification. Although, the bundle geometry has a radial symmetry, because of the presence of baffles, the flow phenomenon in the shell side is not radially symmetric. Moreover, because of the inlet and outlet nozzles the shell side flow is completely different at the inlet and exit compartments of the shell. Therefore, it is not possible to use radial symmetry. Only bilateral symmetry of the shell along the axis of inlet and outlet nozzles can be used.

In the previous works, large scale shell-and-tube heat exchangers are modeled by using simplifications. Without any simplification, a small sized industrial type shell-and tube heat exchanger with 500 tubes and 10 baffles would require at least 150 million computational elements, to resolve the geometry [5]. However, by using an ordinary computer, it is not possible to model such a geometry. The simulation

requires approximately 120 Gigabytes of Random Access Memory (RAM); since every computational element approximately requires 800 bytes of RAM during the solution process in CFD simulations [6]. In brief, the porous medium model, which is the common simplification method, is used in the previous works.

1.2.1 Porous Medium Model

Porous medium model is developed by using a distributed resistance approach, surface permeability and volumetric porosity. In this method, it is assumed that the space within the heat exchanger is homogeneously filled with a fluid and a resistance to fluid motion is distributed on a fine scale in the fluid domain. Presence of the tube bundle and flow baffles are included in the continuum Navier-Stokes equations by using this approach. By using this method, a single computational cell may have multiple tubes. For instance, the sample control volume given in Figure 1-4 might be a computational cell. Therefore, shell side of the heat exchanger is modeled by a relatively coarse grid. Available pressure drop and heat transfer correlations for tube banks can be used in this approach.

In Figure 1-4, there are a finite number of solid structures within the control volume of the V . A is the surface area of the control volume.

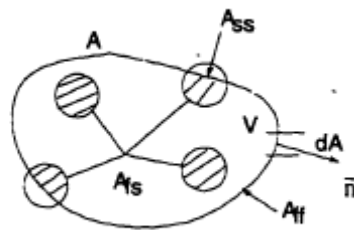


Figure 1-4 Sample control volume with tubes (adapted from [7])

Volumetric porosity is the fraction of the volume occupied by the fluid and defined by the following equation:

$$f_v = \frac{V_f}{V_f + V_s} \quad (1.1)$$

where f_v is a scalar quantity. V_f is the volume occupied by the fluid and V_s is the volume occupied by the solid in the control volume.

Surface permeability is the fraction of surface area open to fluid flow and defined as follows:

$$f_s = \frac{A_{ff} \cdot \vec{n}}{(A_{ff} + A_{ss}) \cdot \vec{n}} \quad (1.2)$$

where A_{ff} is the surface area open to fluid flow; A_{ss} is the surface area blocked by the solid and \vec{n} is the local unit normal vector to the surface. Also, volume occupied by the fluid V_f and the surface area open to fluid flow A_f are defined as follows:

$$V_f = \int_V f_v dV \quad (1.3)$$

$$A_f = \int_A f_s dA \quad (1.4)$$

For a given control volume, general integral balance equation can be expressed as:

$$\int_{V_f} \frac{\partial}{\partial t} (\rho\phi) dV + \int_{A_f} \rho\phi \vec{V} \cdot \vec{n} dA = - \int_{A_f} \vec{n} \cdot \vec{F}_s dA + \int_{V_f} \rho \vec{F}_b dV \quad (1.5)$$

where ϕ is the conserved quantity, \vec{F}_s is the surface force, \vec{F}_b is the body force and \vec{V} is the velocity vector. After substituting Equations 1.3 and 1.4 into 1.5:

$$\int_V \frac{\partial}{\partial t} (\rho\phi) f_v dV + \int_A \rho\phi \vec{V} \cdot \vec{n} f_s dA = - \int_A \vec{n} \cdot \vec{F}_s f_s dA + \int_V \rho \vec{F}_b f_v dV \quad (1.6)$$

By using Gauss divergence theorem and separating diffusion effects; equation (1.6) can be simplified as:

$$\frac{\partial}{\partial t} (\rho f_v \phi) + \nabla \cdot (f_s \rho \phi \vec{V}) = - \nabla \cdot (f_s \vec{F}_s) + \vec{F}_b \rho f_v \quad (1.7)$$

If it is assumed that surface permeability is equal to volumetric porosity, and, $F_b = 0$, $F_s = 0$ and $\phi = 1$; Equation 1.7 simply reduces to continuity equation.

The momentum and enthalpy equations are obtained from Equation 1.7 by substituting corresponding F_b , F_s and ϕ values.

1.2.2 Previous Studies

In several studies, the porous medium approach is used. Sha et al. [8], Prithiviraj and Andrews [5, 9], Prithiviraj [7], Stevanovic et al. [10], He et al. [11], and Andrews and Master [12] have used this approach in their studies.

Sha et al. [8] developed a multidimensional, thermal-hydraulic model for the analysis of shell-and-tube heat exchangers. Shell side is modeled using surface permeability, porosity and distributed resistance approach. Tube side flow is considered as multi channel, parallel flow between two common inlet and exit plenums. The developed analytical model was tested by three sets of experimental data. The comparisons between analytical predictions and the experimental data were found satisfactory.

Prithiviraj and Andrews [5, 9] developed a three dimensional, implicit, control volume based computer code for modeling shell-and-tube heat exchangers. In this work, distributed resistance approach is used with surface permeability and volumetric porosity. For tube banks, available pressure drop and heat transfer correlations are also included in developed model. Heat exchanger sub-models are developed, to completely resolve the heat exchanger geometry. Presence of tubes, turbulence generation and dissipation by tubes, leakage through baffle-shell and baffle-tube clearances, are separately modeled in this work. Baffle, tube and nozzle geometries are not represented as a shape within a computational shell. They are represented in terms of areas. A modified version of $k-\varepsilon$ turbulence model is used with additional source terms for turbulence. Several runs are performed for different heat exchanger geometries and flow parameters, and a good agreement is observed between the computed and experimental values of the overall shell-side pressure drop and the temperature change.

Stevanovic et al. [10] performed a numerical analysis of three dimensional fluid flow and heat transfer in a shell-and-tube heat exchanger. Similar to previously mentioned works, baffles and the tube bundle are modeled using porous media concept. The effect of different turbulence models on heat transfer is examined. Three different turbulence models are used; constant turbulent viscosity model, standard $k-\varepsilon$ turbulence model and a modified version of $k-\varepsilon$ turbulence model (Chen-Kim). It was concluded that experimental data of velocity field has a good agreement with the data from the modified turbulence model.

He et al. [11] modeled shell-and-tube heat exchangers using distributed resistance approach with a modified porous medium model and developed a computer code for analyzing the model. In this work, turbulent fluid flow and heat transfer in shell-and-tube heat exchangers are successfully simulated by the developed three dimensional numerical models. Three types of shell-and-tube heat exchanger are modeled; vertical baffled, helical baffled and finned tube banks. The developed code is validated by comparing with test data.

Andrews and Master [12] performed detailed three-dimensional CFD simulations to investigate the performance of helically baffled shell-and-tube heat exchangers. The distributed resistance approach described by Prithiviraj and Andrews was adapted for the helically baffled shell-and-tube heat exchangers. Simulation results are compared with available correlation results and overall pressure drop computations are found reasonable.

De Henau and Ahmed [13] modeled a shell-and-tube heat exchanger by combining 1-D elements for tube side and 3-D elements for shell side. In this study, a method is developed for coupling the 1-D and 3-D solvers and the two fluid domains are combined in a single domain. The coupling of the fluid domains is accomplished by transferring boundary conditions from one domain to the other. Results from the 1-D/3-D simulation are compared with the full 3-D simulation. The comparison results are found to be in good agreement. In addition, model size is decreased by 30% and solution time is decreased by 25% by using 1-D/3-D coupling method. Furthermore, simulation results are compared with Bell-Delaware correlation based approach. 1-D/3-D and full 3-D simulation results were within 10% of the results obtained from the Bell-Delaware correlations.

1.3 Analytical Calculation Methods

In analytical calculations, Kern method [14] and Bell-Delaware method [15] are used. These methods are the most commonly correlation based approaches used in shell-and-tube heat exchanger design. Kern method gives conservative results and it is only suitable for preliminary sizing. Bell-Delaware method is a very detailed method and usually very accurate in estimating shell side heat transfer coefficient and pressure drop for common shell side geometric arrangements. When Bell-Delaware method is used for rating, it can indicate weaknesses in the shell side design.

In pressure drop calculations, the work of Kapale and Chand [16] is used together with Bell-Delaware method, since inlet and outlet nozzle effects on pressure drop are not included in the Bell-Delaware method.

Prithiviraj and Andrews [17] compared the three dimensional computational fluid dynamics simulation with analytical methods; Kern, Bell-Delaware and Donohue [18] methods. The effectiveness of these methods in predicting various geometric and flow parameters were studied. In this work, it is observed that Bell-Delaware method well predicts the flow characteristics better than the other methods. Donohue method over predicts especially pressure drop compared to the other methods.

1.4 Motivation and Thesis Goals

In this study, the detailed design of a relatively small sized shell-and-tube heat exchanger is performed using a CFD technique. CFD techniques are used in rating, and iteratively in sizing of heat exchangers. In CFD simulations, by modeling the geometry as accurately as possible, the flow structure and the temperature distribution inside the shell can be obtained. This detailed data can be used for calculating global parameters like heat transfer coefficient and pressure drop. These results may be compared with correlation based ones. Furthermore, the data can be used to visualize the entire flow and temperature fields which can help to locate weaknesses in the design such as recirculation and relaminarization zones.

In view of the fact that, the tube side flow is very simple and well understood when compared to shell side flow characteristics, the current study is concentrated on the shell side. Assuming all the tubes have the same mass flow rate value, the front and rear heads of the heat exchanger are not modeled. For different heat exchanger models, shell side heat transfer and flow characteristics are analyzed with a series of CFD simulations. The commercial CFD software, FLUENT, is used together with GAMBIT mesh generation software.

1.5 Brief Outline

In the following chapter, the governing equations and the heat exchanger modeling using FLUENT is discussed in detail. In Chapter 3, various sub-model

simulations of shell-and-tube heat exchanger model are discussed. First, sensitivity of the results to the turbulence model and the discretization order is discussed for a fixed geometry of a shell-and-tube heat exchanger. Next, by changing the baffle spacing and the number of baffles the effect on the pressure drop and the heat transfer are analyzed. Then, the effects of baffle cut height on the pressure drop and the heat transfer are analyzed. In these simulations only the shell-side flow is modeled. For a double pipe heat exchanger, the effect of tube-side flow is discussed in the last part of the Chapter 3, by modeling both shell-side and tube-side flows. In Chapter 4, a full shell-and-tube heat exchanger simulation is performed by modeling both shell and tube sides. Then, the simulation results are compared with the sample run data of a commercially available, miniature shell-and-tube heat exchanger. In the last chapter, the results are discussed, some conclusions are drawn and the future work is suggested.

CHAPTER 2

THEORETICAL BACKGROUND AND CFD MODELING

2.1 Governing Equations

The conservative form of the system of the equations governing the time dependent three-dimensional fluid flow and heat transfer including compressibility effects are presented below.

$$\text{mass} \quad \frac{\partial \rho}{\partial t} + \nabla \cdot (\rho \vec{V}) = 0 \quad (2.1)$$

$$\text{x-momentum} \quad \frac{\partial(\rho u)}{\partial t} + \nabla \cdot (\rho u \vec{V}) = -\frac{\partial p}{\partial x} + \nabla \cdot (\mu \nabla u) + S_{Mx} \quad (2.2)$$

$$\text{y-momentum} \quad \frac{\partial(\rho v)}{\partial t} + \nabla \cdot (\rho v \vec{V}) = -\frac{\partial p}{\partial y} + \nabla \cdot (\mu \nabla v) + S_{My} \quad (2.3)$$

$$\text{z-momentum} \quad \frac{\partial(\rho w)}{\partial t} + \nabla \cdot (\rho w \vec{V}) = -\frac{\partial p}{\partial z} + \nabla \cdot (\mu \nabla w) + S_{Mz} \quad (2.4)$$

$$\text{energy} \quad \frac{\partial(\rho e)}{\partial t} + \nabla \cdot (\rho e \vec{V}) = -p \nabla \cdot \vec{V} + \nabla \cdot (k \nabla T) + \Phi + S_e \quad (2.5)$$

$$\text{equation of state} \quad p = \rho R T \quad (2.6)$$

where ρ is the density, \vec{V} is the velocity vector, u , v and w are the velocity components in the x , y and z respectively, S_M is the momentum source term in the related direction, p is the pressure, R is the gas constant, and S_e is the energy source term. Φ is the dissipation function given by Equation 2.7 and it represents the dissipation of mechanical energy into heat.

$$\Phi = \mu \left[2 \left[\left(\frac{\partial u}{\partial x} \right)^2 + \left(\frac{\partial v}{\partial y} \right)^2 + \left(\frac{\partial w}{\partial z} \right)^2 \right] + \left[\left(\frac{\partial u}{\partial y} + \frac{\partial v}{\partial x} \right)^2 + \left(\frac{\partial u}{\partial z} + \frac{\partial w}{\partial x} \right)^2 + \left(\frac{\partial v}{\partial z} + \frac{\partial w}{\partial y} \right)^2 \right] + \lambda (\nabla \cdot \vec{V})^2 \right] \quad (2.7)$$

Assuming that the steady state conditions prevail, time dependent parameters are dropped from the equations. Since the flow inside the heat exchanger is neither a high speed nor a high viscous flow, the dissipation function is omitted. The dissipation function is effective for high Mach number flows. Equation 2.6 is also omitted due to the incompressibility of air. The momentum source terms in the x and z directions can be omitted, and ρg_i can be written for the momentum source term in the y -direction. The resulting equations are:

$$\text{mass} \quad \nabla \cdot (\rho \vec{V}) = 0 \quad (2.8)$$

$$\text{x-momentum} \quad \nabla \cdot (\rho u \vec{V}) = -\frac{\partial p}{\partial x} + \nabla \cdot (\mu \nabla u) \quad (2.9)$$

$$\text{y-momentum} \quad \nabla \cdot (\rho v \vec{V}) = -\frac{\partial p}{\partial y} + \nabla \cdot (\mu \nabla v) + \rho g_i \quad (2.10)$$

$$\text{z-momentum} \quad \nabla \cdot (\rho w \vec{V}) = -\frac{\partial p}{\partial z} + \nabla \cdot (\mu \nabla w) \quad (2.11)$$

$$\text{energy} \quad \nabla \cdot (\rho e \vec{V}) = -p \nabla \cdot \vec{V} + \nabla \cdot (k \nabla T) \quad (2.12)$$

Since the flow in this study is turbulent, turbulence effects should be taken into account using a turbulence modeling. In Appendix A, theoretical background about the turbulence models used in this study is discussed.

2.2 CFD Modeling

A typical CFD software consist of three main parts; a pre-processor, a solver and a post-processor. In pre-processor, input data of the model, which is used by the solver, is processed and computational grid is created. In solver execution, the discretized physical equations are solved according to boundary conditions of the

model, until convergence criteria is met. In post-processing the results are examined using data visualization tools. In this chapter, these three main parts are discussed, for the heat exchanger model used in section 3.2. This model is a shell-and-tube heat exchanger with six baffles, and only the shell side flow is modeled.

2.2.1 Pre-Processing

Inputs of the flow problem are entered into a CFD program in the pre-processing step. The user activities at the pre-processing stage involve the following steps [19]:

- Definition of the geometry
- Mesh generation
- Selection of the physical phenomena
- Definition of continuum types
- Specification of boundary condition types

Pre-processing step in this study is performed using GAMBIT. The details of the pre-processing are discussed below.

2.2.1.1 Definition of the Geometry

In this step, the definition of the geometry of interest is performed using GAMBIT. The computational domain is formed using simple geometrical primitives. A shell, inlet and outlet nozzles, baffles and tubes are formed by using cylinders. Then the shell and the nozzles are united. The baffles are formed by splitting at the desired baffle cut height and moved to the desired locations. Finally the baffles and the tubes are splitted from shell geometry and final shell geometry is formed. The shell-and-tube heat exchanger model used in section 3.2 is shown in Figure 2-1.

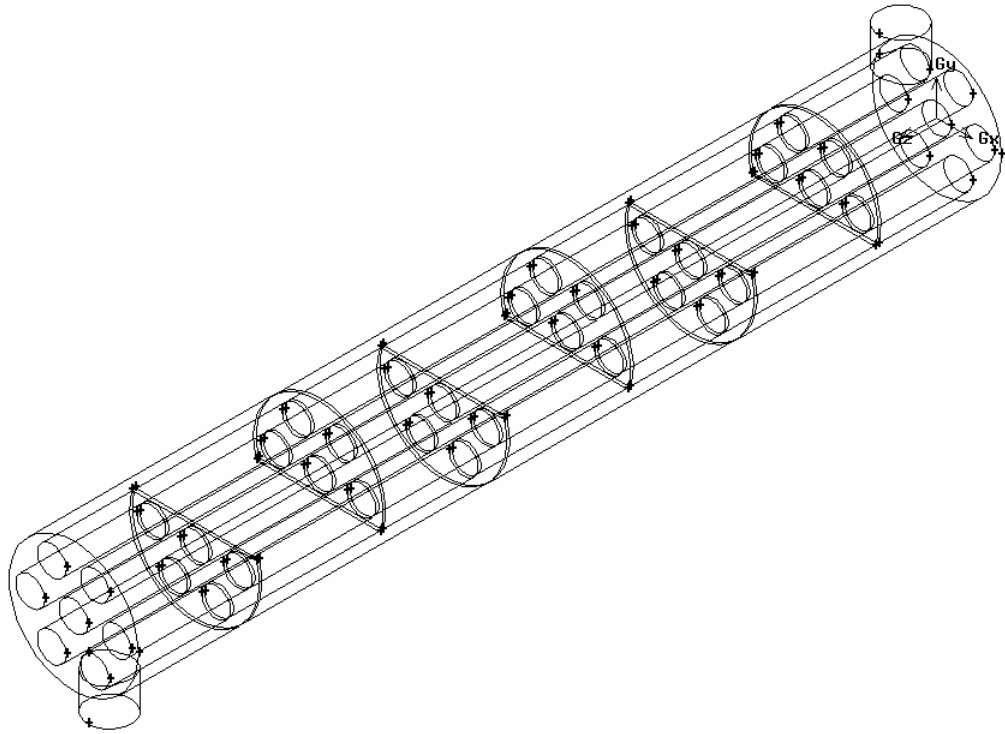


Figure 2-1 The heat exchanger model with six baffles

2.2.1.2 Mesh Generation

Mesh generation is the division of computational domain into smaller sub-domains. Mesh generation of the model is performed using GAMBIT. First, surfaces of the model are meshed using quadrilateral elements. The surface mesh is created starting from critical parts of the model, and then the other surfaces are meshed. The shell surface, which is perpendicular to tubes, and the baffles are meshed, then the tube surfaces are meshed accordingly. Similarly, the nozzle inlets and the nozzle sides are meshed, then the outer surface of the shell is meshed correspondingly. After all the surfaces are meshed successfully then the shell volume is meshed using tetragonal-hybrid elements. In the full heat exchanger model used in Chapter 4, the tube side is also meshed. The meshing procedure is similar to the explained process above. Only difference is the tube side is also

meshed. The details of the meshing process of the full model are discussed in Chapter 4.

The generated mesh should be examined, using "Examine Mesh" option in GAMBIT. This option allows user to specify the portion of the mesh elements to be displayed and the display mode for those elements. Choosing the display type as "Range", the skewness of the mesh is checked.

Skewness is the difference between the shape of the cell and the equivalent cell volume. For instance, for quadrilateral elements, the equivalent cell is a rectangular prism. Skewness value of "0" describes an equilateral element and skewness value of "1" describes a poorly shaped element. And it is recommended that maximum skewness value should not exceed 0.75 [20]. Skewness of the cells is important, since highly skewed elements cause convergence problems and decrease the accuracy. In Figure 2-2 mesh from a vertical cut-plane of the generated mesh is shown, with a maximum skewness of 0.62.

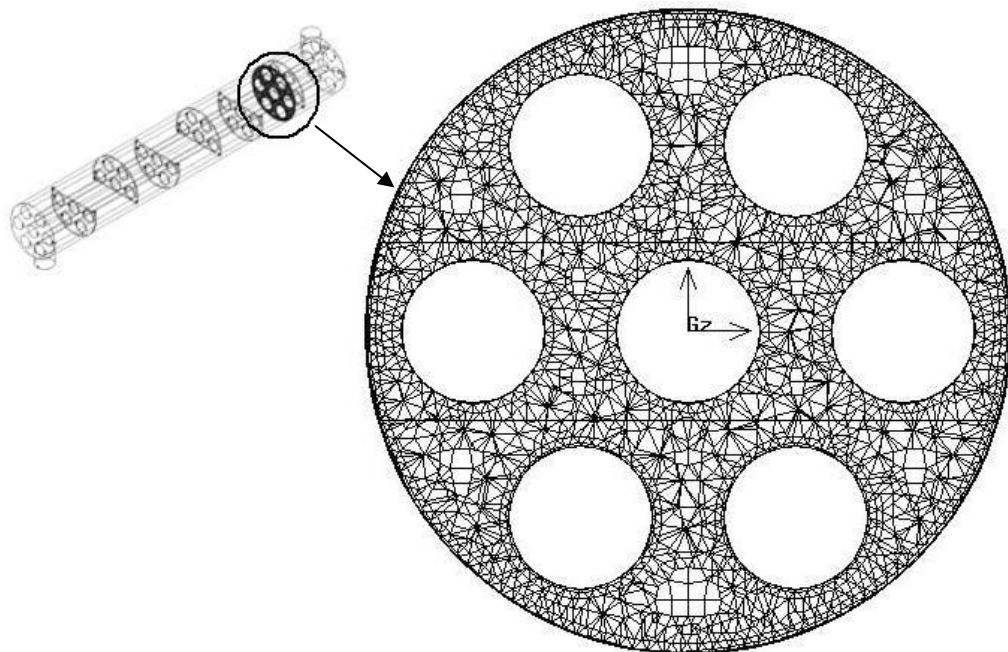


Figure 2-2 Mesh from a vertical cut-plane

2.2.1.3 Selection of the physical phenomena

In this step, the physical phenomena which need to be modeled are selected. If any special chemical phenomenon is present in modeling, it should be specified.

2.2.1.4 Definition of Continuum Types

Continuum types define physical characteristics of the sub-domain [20]. If *fluid* continuum-type is assigned to a volume entity, equations of momentum, continuity, and transport apply at cells that exist within the volume. On the other hand, only the energy and species transport equations (without convection) apply at the cells that exist within a volume when *solid* continuum-type is assigned.

2.2.1.5 Specification of Boundary Conditions

In CFD simulations, appropriate boundary condition specification is important. Boundary condition types are specified at cells which touch the domain boundary. In GAMBIT, different boundary types are displayed with different colors. In Figure 2-3 boundary condition types are shown for the sample heat exchanger with different colors. Mass flow inlets are displayed as blue, pressure outlets are displayed as red and all walls are displayed as white. Outer walls of the model displayed as transparent for better visualization.

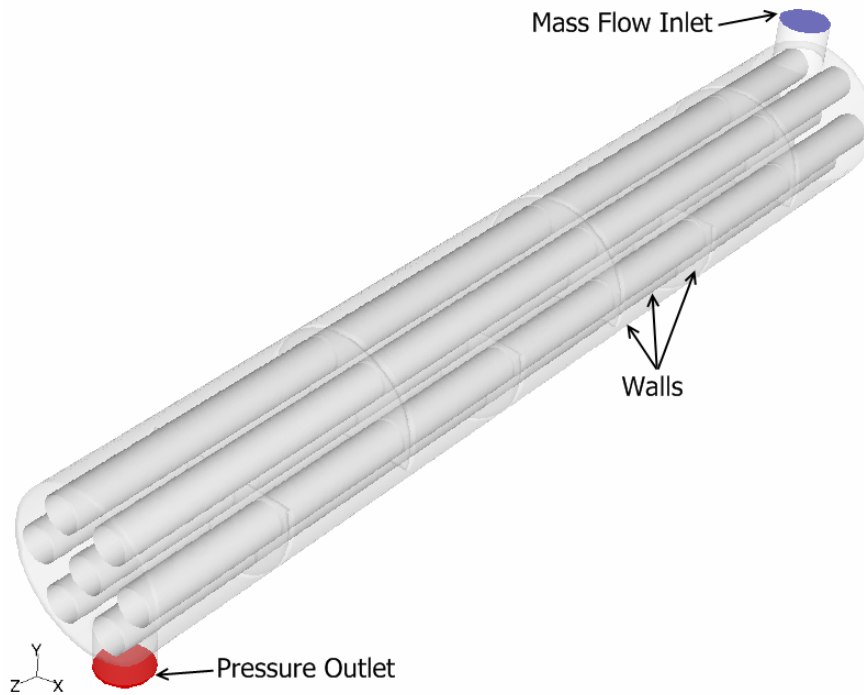


Figure 2-3 Boundary condition types

2.2.2 Solver Execution

In this section FLUENT solver execution steps are discussed in detail.

2.2.2.1 Grid Adjustment

Adjusting grid for the analysis is the first step in the solver execution. First grid must be checked using *grid-check* command. If any errors present in the grid, they would be reported. Minimum volume value must be checked. It must be positive, since the solver cannot begin calculation when minimum volume has a negative value. Then, the grid must be scaled. Next, the domain should be reordered using *Reverse Cuthill-McKee Method* (RCM). The RCM ordering is commonly used when a matrix is to be generated whose rows and columns are numbered according to the numbering of the nodes. By an appropriate renumbering of the nodes, it is often possible to produce a matrix with a much smaller bandwidth [21]. By using this

method computational domain is reordered and computational time would be decreased.

2.2.2.2 Solver Selection

Two numerical methods are available in FLUENT solver; density based and pressure based solvers. In the earlier versions of the FLUENT these are referred as coupled and segregated solvers. Conservation equations for mass, momentum and energy are solved simultaneously in the coupled solver, whereas, in the segregated solver the equations are solved sequentially. But, the memory requirement increases by 1.5 - 2 times that of the segregated algorithm since the discrete system of all momentum and pressure-based continuity equations needs to be stored in the memory when solving for the velocity and pressure fields [22]. Therefore, solution time also increases in the coupled solver.

Under gradient option *Green – Gauss node based* choice is selected, since the node based averaging scheme is more accurate than the cell-based scheme for unstructured mesh which allows any number of elements to meet at a single node. Implicit type formulation is used in pressure based- segregated solver. In implicit type formulation; system of unknown values in each cell is solved simultaneously for a given variable, by using both existing and unknown values from the neighboring cells.

In this work the pressure based – segregated solver is used with node based gradient option.

2.2.2.3 Turbulence Model Selection

Turbulence model selection is an important point in CFD. The choice of the turbulence model depends on the physics of the flow, the solution behavior, available computational resources, CPU time and the required accuracy level. Turbulence model selection is discussed in section 3.2. Various turbulence models

are tried for different solution parameters and the theoretical background is discussed in Appendix A.

2.2.2.4 Choosing Discretization Scheme

In FLUENT, the discretization scheme for the convection terms of each governing equation could be separately selected. By default, the first-order upwind discretization scheme is used for convection terms in all equations, when the pressure based solver is used. The upwind discretization scheme is more stable than the other discretization schemes, since, the flow direction is taken into account in this method. Thus, the main reasons for using the upwind scheme in discretization are its stability and sensitivity to the flow direction.

In the current study, for the momentum, energy and turbulence terms, the first and the second order discretization schemes are tried. And, for the pressure, the standard and the second order discretization schemes are used.

Usually first order discretization has better convergence than the second order; on the other hand, it generally gives less accurate results. Discretization errors are reduced in higher order schemes, since more neighboring points are included in higher order schemes [19].

2.2.2.5 Defining Materials

Materials are defined in the solver using FLUENT Material Database. The main material used in the analyses is water. Water exists in two phases in the database. Water in liquid phase is copied from database. But, properties of the liquid water in the FLUENT database are defined as constant. Therefore, properties of the water are redefined using piecewise-linear functions. Properties are redefined for density, thermal conductivity, viscosity and specific heat capacity of water. Properties are defined in terms of temperature by using Thermo-Physical Properties of Saturated Water tables available in the literature [2]. The range of temperature in the

simulations is between 293 K and 450 K. The details of the water properties in this range are presented in Appendix B.

For other materials constant material properties are applied. In double pipe heat exchanger carbon-steel is defined as the tube material. Steel properties are copied from the material database. Then, desired material properties are adjusted to design values.

2.2.2.6 Defining Boundary Conditions

Inlets

At the inlet boundaries, the distribution of flow variables needs to be specified. Mass flow rate boundary condition is applied to inlets of the models. For the thermal boundary condition, desired temperature value is assigned. Direction of the boundary condition is specified as normal to boundary. Mass flow rate boundary condition is only assigned as constant; thus, the inlet velocity profile is given as uniform in FLUENT. In Chapter 4, to assign non-uniform velocity, inlet nozzle of the model is extended. Thus, inlet nozzle of the model is extended to compensate the effects of the entrance region. Again, mass flow rate boundary condition is applied, but, it is also possible to define a non-uniform velocity profile. Details of non-uniform velocity profile are discussed in Appendix C.

Turbulence specification method is selected as intensity and hydraulic diameter. For internal flows, the turbulence intensity at the inlets is totally dependent on the upstream history of the flow. If the flow is fully developed, the turbulence intensity may be as high as a few percent [22]. Furthermore, it is suggested that for high-speed flows inside complex geometries like heat-exchangers and flow inside rotating machinery, typically, the turbulence intensity value is between 5% and 20%. Also, for flows in not-so-complex devices like large pipes, ventilation flows etc. or low speed flows, typically, the turbulence intensity is between 1% and 5% [23].

At the inlet boundaries, flow is assumed as fully developed. And turbulence intensity value is assigned as 5%. And the hydraulic diameter simply equals to the inlet diameter.

Outlets

Pressure outlet type boundary condition is applied at the outlets. For the pressure outlet boundaries the recommended outlet condition is a gage static pressure value of zero. If this condition is applied to an outlet, then no other conditions need to be assigned to the outlet boundary [24].

Similar to the inlet boundary, the turbulence specification method is selected as intensity and hydraulic diameter. The turbulence intensity value is assigned as 5%. The outlet nozzle diameter is assigned as the hydraulic diameter.

Walls

Wall boundary conditions are used to bound fluid and solid regions. By default, all walls are considered as stationary walls and no slip shear condition is assigned to all wall type boundaries. If no specific thermal boundary condition applied to the walls, all walls considered as perfectly insulated, and the zero heat flux thermal condition is applied to the walls.

If both the shell and the tube sides are modeled, two-sided walls appear in the solution domain. When a wall zone has a fluid or solid region on each side, it is called a two-sided wall. Thermal conditions for two-sided walls should be coupled. If a grid with this type of wall zone opened into FLUENT, a *shadow* zone will automatically be created so that each side of the wall is a distinct wall zone [22]. Under *thermal conditions*, *coupled* option should be selected to couple two sides of the wall. Heat transfer through two sides of the wall is calculated by the solver directly from the neighboring cells. Therefore no additional thermal boundary condition required.

2.2.2.7 Initialization

Full Multigrid Initialization (FMG) is used at the beginning of the FLUENT analysis to accelerate convergence of the problem. After performing standard initialization, FMG initialization utilizes the FLUENT Full-Approximation Storage (FAS) Multigrid technology to obtain the initial solution. FAS multigrid approach merges groups of cells on the finer grid to form coarse grid cells. Coarse grid cells are formed by combining the cells surrounding a node, as shown in Figure 2-4.

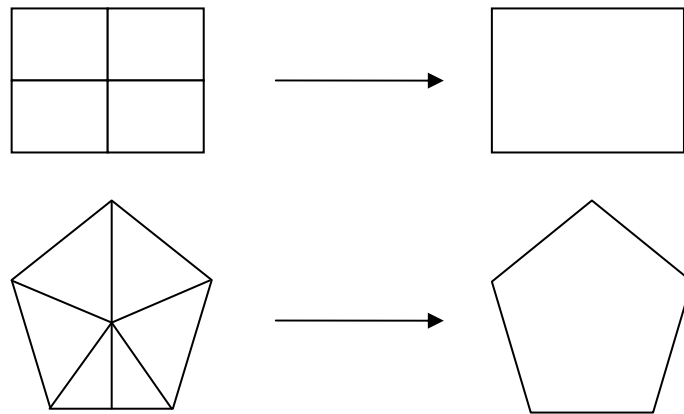


Figure 2-4 Node combining to form coarse grid cells

FMG initialization procedure constructs the desirable number of geometric grid levels. FMG initialization procedure is computationally economical, since most of the computation is performed on coarse levels. Good initial solutions could be obtained for large solution domains.

The following steps are performed, when FMG initialization is applied.

- The current solver selection and all current solver parameters are recorded.
- The selected solver switched to the density-based explicit formulation.

- FMG iteration is performed using the given FMG parameters.
- Solver selection and original solver parameters restored.

2.2.3 Post-Processing

In post-processing, the results of the CFD analysis are examined, after the solver is terminated. By using reports, surface and volume integrals, and the graphical analysis tool results of the CFD simulations are examined in the post-processing step.

Details of the post-processing steps are discussed below.

2.2.3.1 Evaluating Average Temperature

The average temperature value of a desired boundary is evaluated by using *report-surface integrals* command. For the report type, *facet average* is selected. Facet average choice gives the facet-averaged quantity on the selected surface.

2.2.3.2 Evaluating Pressure Drop

Similarly, the pressure drop value of a desired boundary is evaluated by using *report-surface integrals* command. For the report type, *facet average* is selected. Since, gage static pressure value of zero is assigned to an outlet boundary; the pressure drop value is directly evaluated.

2.2.3.3 Evaluating Total Heat Transfer Rate

By using *report-fluxes-total heat transfer rate* command, the total heat transfer rate value through a desired surface is reported. This value can be checked by using *report-surface integrals* command and selecting total surface heat flux through the desired surface. When total surface heat flux value is multiplied by the area of the surface, the obtained value will be equal to the previously reported total heat transfer rate.

2.2.3.4 Evaluating Mass Flow Rate

The mass flow rate value of an exit boundary must be checked; since, only the gage pressure value of zero is assigned to an outlet boundary. The mass flow rate value of a boundary can be checked by using *report-fluxes-mass flow rate* command.

CHAPTER 3

HEAT EXCHANGER MODELING

3.1 Introduction

In this part of the study, various sub-model CFD simulations of shell-and-tube heat exchanger models are performed. First, for a simple shell-and-tube heat exchanger geometry, the sensitivity of results to turbulence model and discretization order is discussed. Next, the effect of baffle spacing on pressure drop and heat transfer is analyzed; by changing the number of baffles. Then, the effect of baffle cut height on pressure drop and heat transfer is analyzed. In these simulations, the analyses are focused on the shell-side flow. In the last part of this chapter, the effect of inclusion of the tube-side flow is discussed, for a double pipe heat exchanger.

3.2 Sensitivity of the Results to Turbulence Model and Discretization

In this section, a small shell-and-tube heat exchanger is considered. The geometric model is presented in Figure 2-1 with six baffles used in this study. This geometry primarily selected for its simplicity. It is used as the base geometry in this part of the study. In this section, a suitable turbulence model and a discretization scheme are selected based on this model, then, a full heat exchanger model simulation is conducted in the following chapter. Some design parameters and predetermined geometric parameters are presented in Table 3-1. Baffle cut is selected to place the cut just below or above the central row of three tubes. The tube side is not considered and a constant temperature is assigned to all tube walls.

Sensitivity of the results to the turbulence model and the discretization order is investigated for three different shell-side mass flow rate values. Two different mesh densities are used in the analyses. Mesh selection, boundary condition assignment, turbulence model selection and other modeling choices are explained below.

Table 3-1 Design parameters and fixed geometric parameters

Shell size, D_s	90 mm
Tube outer diameter, d_o	20 mm
Tube bundle geometry and pitch	Triangular, 30 mm
Number of tubes, N_t	7
Heat exchanger length, L	600 mm
Shell side inlet temperature, T	300 K
Baffle cut, B_c	36 %
Central baffle spacing, B	86 mm
Number of baffles, N_b	6

3.2.1 Mesh Selection

Two different mesh sizes are used in the six baffle case. Approximately 700,000 elements are present in the coarse mesh, where as, the finer mesh has about 1,360,000 elements. Meshing details are presented in Table 3-2. First, surfaces of the model are meshed using quadrilateral elements. Then the shell volume is meshed using tetragonal-hybrid elements.

Map and *Pave* type elements are used in surface meshing. The main difference between map and pave elements is; *map* command creates a regular, structured grid of mesh elements, whereas, *pave* command creates an unstructured grid of mesh elements. Structured grid methods take their name from the fact that the grid is laid out in a regular repeating pattern called a block. On the other hand,

unstructured grid methods utilize an arbitrary collection of elements to fill the domain. Because the arrangement of elements has no discernible pattern, the mesh is called unstructured [25]. Therefore, for the surfaces of the geometry with a regular geometry are meshed with map elements and the other surfaces are meshed with pave elements. In Figure 3-1 examples of structured and unstructured meshes are presented.

Table 3-2 Meshing Details

	interval size	elements	type	interval size	
				Fine mesh	Coarse mesh
surfaces					
inlet & outlet nozzles		quad	pave	1	2
surface of nozzles		quad	pave	2	3
shell wall (perpendicular to tubes)		quad	pave	2	3
baffle (thickness)		quad	map	1	2
baffle surfaces		quad	pave	2	3
tube surfaces		quad	map	2	3
shell outer wall		quad	pave	2	3
volume					
shell volume		tet-hybrid	hex-core	2	3

For the shell volume, hex-core type tet-hybrid elements are used in meshing. Hex core type generates a core of regular hexahedral elements surrounded by transition layers of tetrahedral, pyramidal, and wedge elements. Tet-Hybrid meshing scheme specifies that the mesh is composed primarily of tetrahedral elements but may include hexahedral, pyramidal, and wedge elements where appropriate. Example of a hex-core type tet-hybrid mesh is given in Figure 3-2.

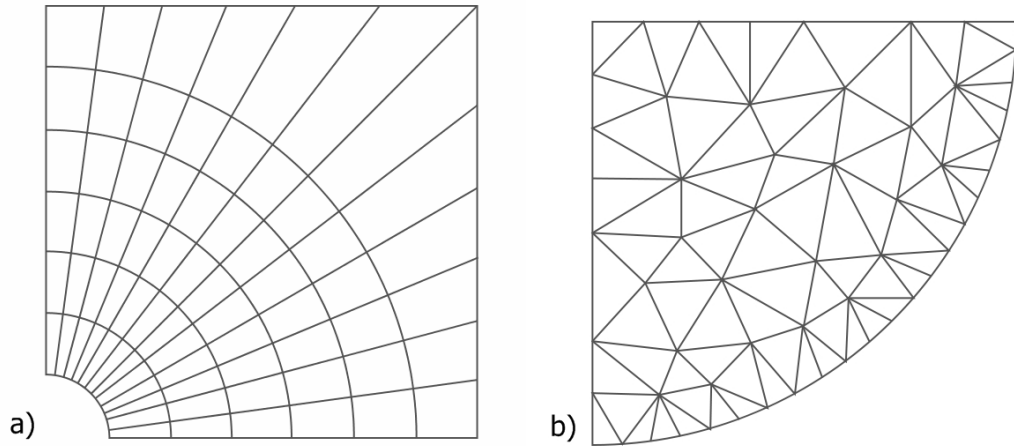


Figure 3-1 Grid examples: a) structured grid, b) unstructured grid (adapted from [20])

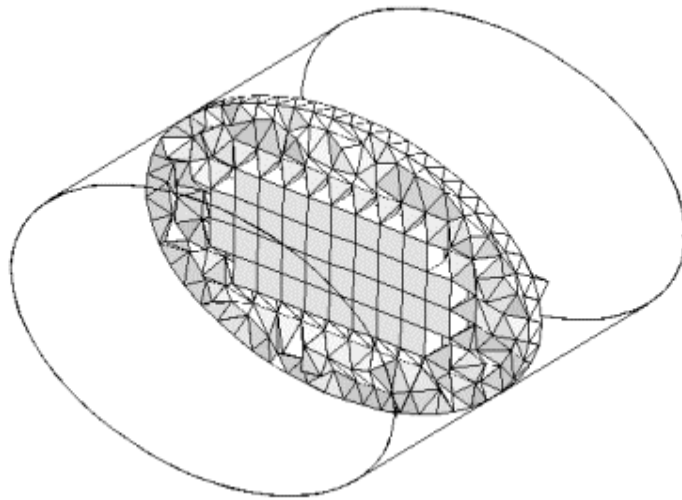


Figure 3-2 Example of a hex-core type tet-hybrid mesh (adapted from [20]).

3.2.2 Boundary Conditions

Boundary conditions are specified into the model as described in section 2.2.2.6. The temperature value of 300 K and the desired mass flow rate value are assigned to the inlet nozzle of the heat exchanger. Then, zero gauge pressure is assigned to

the outlet nozzle. Assuming the shell outer wall is insulated, zero heat flux boundary condition is assigned to the shell outer wall. The tube side flow is very simple and easy to resolve; therefore, this part of the work is concentrated on the shell side flow. Therefore, a constant temperature of 450 K is assigned to the tube walls.

3.2.3 Turbulence Model

Spalart-Allmaras and $k-\varepsilon$ turbulence models are performed as turbulence model choices. The Spalart-Allmaras model is a one-equation turbulence model that solves an equation for the kinematic eddy (turbulent) viscosity. In Spalart-Allmaras turbulence model, only one turbulence equation is solved, therefore it is the least expensive model in FLUENT considering computational effort [22].

Two types of $k-\varepsilon$ turbulence model are performed; standard and realizable. Since one more transport equation is to be solved in the $k-\varepsilon$ model, it requires more computational effort than the Spalart-Allmaras model. $k-\varepsilon$ turbulence model is the one of the simplest complete models of turbulence because two separate transport equations are included in the model. And this allows the turbulent velocity and length scales to be independently determined in the model.

The standard $k-\varepsilon$ model is a semi-empirical model based on model transport equations for the turbulence kinetic energy k and its dissipation rate ε . The realizable $k-\varepsilon$ model differs from the standard $k-\varepsilon$ model in two points; a new formulation for the turbulent viscosity included in the realizable model, and for the dissipation rate ε a different transport equation is derived. The realizable $k-\varepsilon$ model requires slightly more computational effort than the standard $k-\varepsilon$ model. The transport equations, viscosity calculation method, and the constants used in the model are the main differences between the standard and the realizable $k-\varepsilon$ models [22].

3.2.4 Other Modeling Choices

The first order and second order discretization schemes are performed in analysis. In the first order discretization, the standard scheme is selected for pressure, and the first order upwind scheme is selected for momentum, turbulent kinetic energy and dissipation rate. In the second order discretization, the standard second order scheme is selected for pressure, and the second order upwind scheme is selected for momentum, turbulent kinetic energy and dissipation rate.

For most problems, default convergence criterion in FLUENT is sufficient. In this study default convergence criterion is used. This criterion requires that the scaled residual for pressure residual is taken as 10^{-6} , and for all other residuals it is taken as 10^{-3} .

Another popular approach for judging convergence is to require that the unscaled residuals drop by three orders of magnitude. FLUENT provides residual normalization for this purpose, where residuals are defined for both the pressure-based solver and the density-based solver. In this approach the convergence criterion is that the normalized unscaled residuals should drop to 10^{-3} . The difference between the scaled and the unscaled residuals are discussed in Fluent Users Guide [22].

3.2.5 Results and Discussion

The results of the CFD analysis for different turbulence models and discretization orders are tabulated in Table 3-3. In Table 3-3, the shell side outlet temperature, shell side pressure drop and total heat transfer rate values are obtained directly from the CFD runs. The heat transfer coefficient values are calculated using the temperature difference and heat transfer area from the log-mean-temperature-difference method [26]. A detailed sample calculation for obtaining heat transfer coefficient is presented in Appendix D. In Table 3-4, results of the analytical calculations are tabulated. In analytical calculations, Kern method and Bell-Delaware method are used, and the detailed sample calculations are discussed in

Appendix E. In Table 3-3 and 3-4, a capital letter is assigned to each case, and for the second order discretization "-2" added.

In Table 3-4 it is observed that, in all cases, Kern Method under predicts the heat transfer coefficient. It is due to the conservative approach taken by the Kern method and its fixed baffle cut value of 25%. As expected, Bell-Delaware method gives better results for overall heat transfer coefficient calculation. Furthermore, the difference between CFD analyses and the analytical calculations increases by increasing the mass flow rate.

It is difficult to follow the results presented in Table 3-4. Therefore, to easily follow this table, in Figures 3-3, 3-4, 3-5 and 3-6 the results of the CFD analysis for turbulence model and mesh density are plotted for each mass flow rate value. In Figure 3-3 shell side mass flow rate values, in Figure 3-4 heat transfer coefficient values, in Figure 3-5 shell side pressure drop values and in Figure 3-6 total heat transfer values are compared for each case.

The percent differences between the analytical calculations and CFD analysis results are presented in Table 3-5. The analytical calculations are taken as base values for the percent difference calculations. For the heat transfer coefficient comparison, CFD results are compared with Bell-Delaware method.

Table 3-3 Results of the CFD analysis for different turbulence models and discretization order for $N_b = 6$

				Results of the CFD Analysis			
Case	Turbulence Model	Mesh	Mass Flow Rate (kg/s)	Shell Side Outlet Temp. (K)	Heat Transfer Coeff. (W/m ² K)	Shell Side Pressure Drop (Pa)	Total Heat Transfer Rate (W)
A	$k-\varepsilon$ standard	coarse mesh	0.5	321.76	2127	2153	76950
			1	326.05	3561	6648	126824
			2	327.22	6452	24692	228780
B	$k-\varepsilon$ standard 2nd order	coarse mesh	0.5	320.58	2116	2209	76872
			1	325.15	3547	6732	126742
			2	326.90	6438	24792	228564
C	$k-\varepsilon$ realizable	coarse mesh	0.5	334.20	2078	1509	71808
			1	327.72	3348	6112	118515
			2	325.74	6163	24464	219733
D	Spalart Allmaras	fine mesh	0.5	323.44	2323	2036	83512
			1	326.29	3654	6586	130031
			2	323.89	6151	25465	220773
D-2	Spalart Allmaras 2nd order	fine mesh	0.5	318.27	2013	2367	73713
			1	320.84	3330	7419	120845
			2	321.10	5952	27291	215792
E	$k-\varepsilon$ standard	fine mesh	0.5	332.14	2501	1768	87100
			1	330.00	3941	6570	138318
			2	328.65	6994	25005	246709
E-2	$k-\varepsilon$ standard 2nd order	fine mesh	0.5	325.01	2511	2162	89752
			1	327.37	3904	6714	138383
			2	328.46	6980	25068	246391
F	$k-\varepsilon$ realizable	fine mesh	0.5	340.40	2514	1522	84853
			1	330.18	3757	6168	131785
			2	326.64	6768	24963	240506
F-2	$k-\varepsilon$ realizable 2nd order	fine mesh	0.5	343.90	2819	1547	93851
			1	337.68	4695	6198	160103
			2	332.10	8585	25702	298975

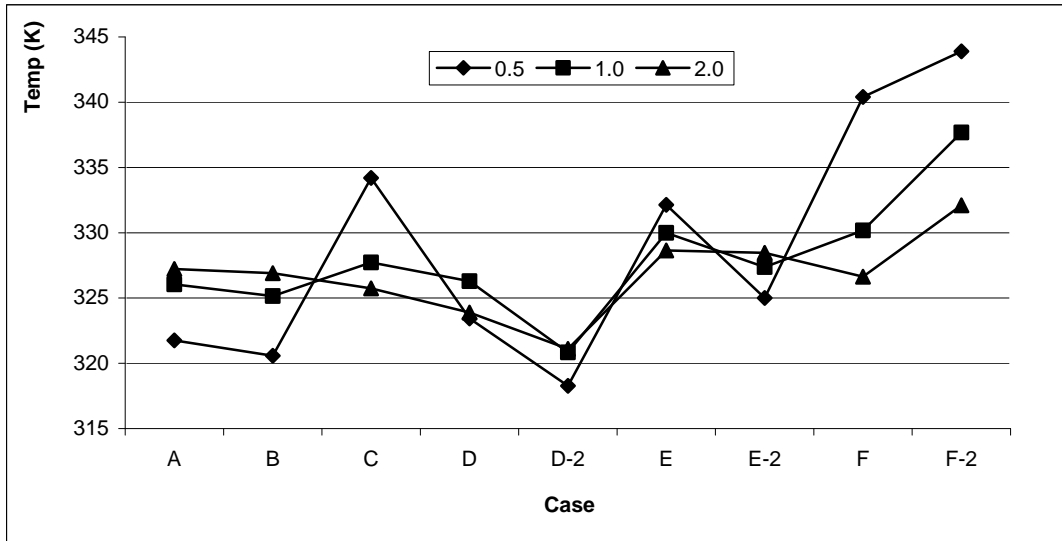


Figure 3-3 Comparison of outlet temperature values

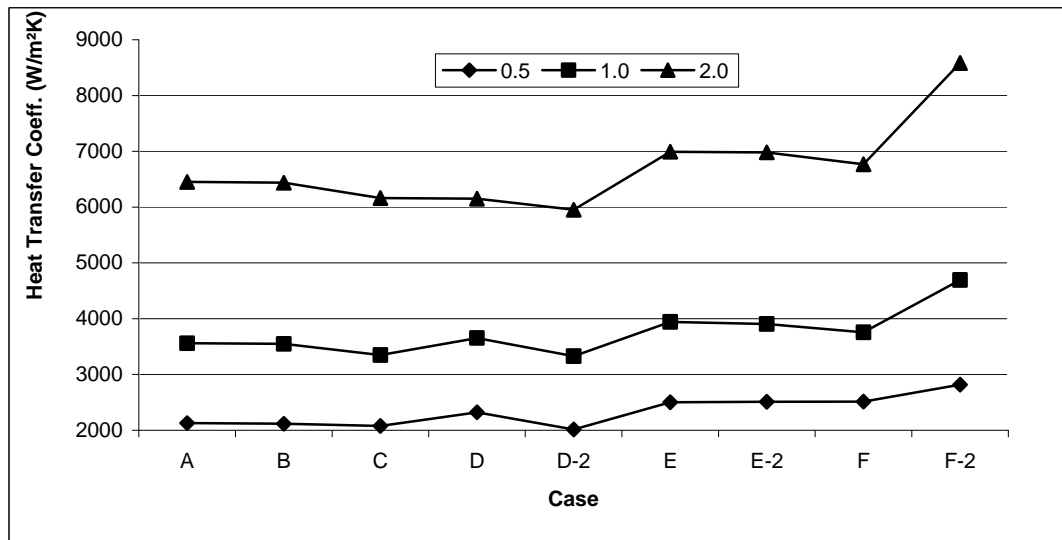


Figure 3-4 Comparison of heat transfer coefficient values

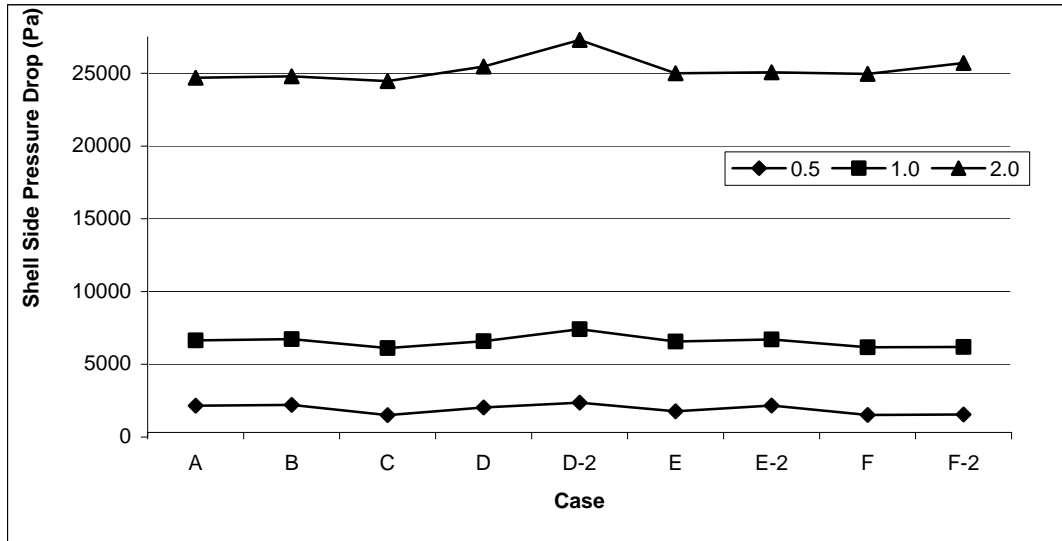


Figure 3-5 Comparison of shell side pressure drop values

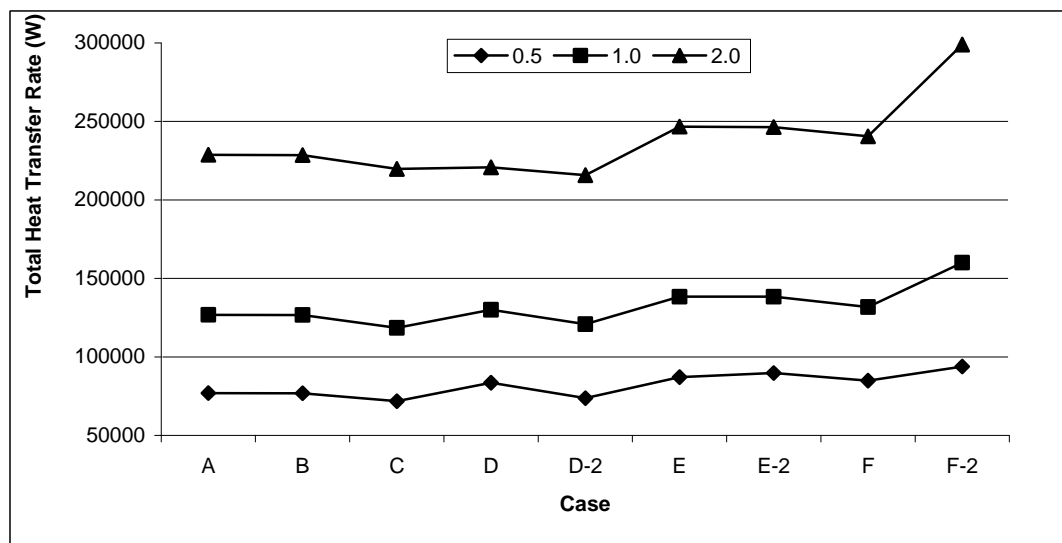


Figure 3-6 Comparison of total heat transfer rate values

Table 3-4 Results of the analytical calculations for $N_b = 6$

Case	Turbulence Model	Mesh	Mass Flow Rate (kg/s)	Analytical Calculations			
				Kern Method	Bell-Delaware Method		
				Heat Transfer Coeff. (W/m ² K)	Heat Transfer Coeff. (W/m ² K)	Shell Side Pressure Drop (Pa)	Total Heat Transfer Rate (W)
A	$k-\epsilon$ standard	coarse mesh	0.5	2076	2113	1230	45460
			1	3063	3276	4587	108855
			2	4494	5037	18650	227494
B	$k-\epsilon$ standard 2nd order	coarse mesh	0.5	2072	2122	1234	42993
			1	3058	3267	4585	105092
			2	4491	5029	18640	224818
C	$k-\epsilon$ realizable	coarse mesh	0.5	2123	2177	1242	71471
			1	3072	3290	4592	115838
			2	4482	5019	18630	215118
D	Spalart Allmaras	fine mesh	0.5	2082	2121	1232	48971
			1	3064	3277	4588	109858
			2	4467	4992	18610	199648
D-2	Spalart Allmaras 2nd order	fine mesh	0.5	2063	2097	1227	38166
			1	3035	3234	4575	87074
			2	4445	4964	18580	176321
E	$k-\epsilon$ standard	fine mesh	0.5	2115	2167	1240	67162
			1	3085	3306	4597	125372
			2	4506	5113	18660	239453
E-2	$k-\epsilon$ standard 2nd order	fine mesh	0.5	2088	2129	1233	52253
			1	3070	3287	4591	114374
			2	4504	5024	18630	237864
F	$k-\epsilon$ realizable	fine mesh	0.5	2147	2213	1248	84442
			1	3086	3311	4597	126125
			2	4489	5025	18640	222644
F-2	$k-\epsilon$ realizable 2nd order	fine mesh	0.5	2161	2231	1251	91766
			1	3128	3370	4616	157501
			2	4534	5094	18700	268312

Table 3-5 Percent differences between analytical calculations and CFD analysis

Case	Turbulence Model	Mesh	Mass Flow Rate (kg/s)	Heat Transfer Coeff.	Shell Side Pressure Drop	Total Heat Transfer Rate
				% difference w.r.t Bell-Delaware	% difference	% difference
A	$k-\epsilon$ standard	coarse mesh	0.5	0.7	42.9	40.9
			1	8.0	31.0	14.2
			2	21.9	24.5	0.6
B	$k-\epsilon$ standard 2nd order	coarse mesh	0.5	0.3	44.1	44.1
			1	7.9	31.9	17.1
			2	21.9	24.8	1.6
C	$k-\epsilon$ realizable	coarse mesh	0.5	4.8	17.7	0.5
			1	1.7	24.9	2.3
			2	18.6	23.8	2.1
D	Spalart Allmaras	fine mesh	0.5	8.7	39.5	41.4
			1	10.3	30.3	15.5
			2	18.8	26.9	9.6
D-2	Spalart Allmaras 2nd order	fine mesh	0.5	4.2	48.2	48.2
			1	2.9	38.3	27.9
			2	16.6	31.9	18.3
E	$k-\epsilon$ standard	fine mesh	0.5	13.4	29.9	22.9
			1	16.1	30.0	9.4
			2	26.9	25.4	2.9
E-2	$k-\epsilon$ standard 2nd order	fine mesh	0.5	15.2	43.0	41.8
			1	15.8	31.6	17.3
			2	28.0	25.7	3.5
F	$k-\epsilon$ realizable	fine mesh	0.5	12.0	18.0	0.5
			1	11.9	25.5	4.3
			2	25.8	25.3	7.4
F-2	$k-\epsilon$ realizable 2nd order	fine mesh	0.5	20.9	19.1	2.2
			1	28.2	25.5	1.6
			2	40.7	27.2	10.3

It is observed that, for all cases in Table 3-4, pressure drop values are lower in the analytical calculations than the CFD analysis results in Table 3-3. The main reason for this may be explained by the baffle spacing to shell diameter ratio B/D_s . Pressure drop is strongly affected by the baffle spacing. Analytical methods under predict the pressure drop, if the window flow area is considerably less than the cross flow area [27]. Mukherjee [3] suggested that, the optimum B/D_s ratio is between 0.3 and 0.6, whereas, in the current model, B/D_s is calculated as 0.96.

In Figure 3-3, it is observed that, for cases B, D and D-2 shell side outlet temperature unexpectedly increases by increasing the mass flow rate. It is expected that; shell side outlet temperature should decrease with increasing mass flow rate. Also, from Table 3-5, it is observed that, the total heat transfer rate results are not acceptable for these cases.

In Figure 3-3, in cases A, E and E-2, $k-\varepsilon$ standard turbulence model is used. The behavior of the shell side outlet temperature differs in these cases. Again, it is expected that; shell side outlet temperature should decrease with increasing mass flow rate. But, for case A and E-2 it is increasing with increasing mass flow rate, whereas, for case E it is decreasing with increasing mass flow rate. Thus, for the current simulation, $k-\varepsilon$ standard turbulence model is not stable. In addition, the difference between total heat transfer rates increases by decreasing the mass flow rate. Also, the order of shell outlet temperatures with respect to the increasing mass flow rate is inconsistent.

In cases C, F and F-2 of Table 3-3, $k-\varepsilon$ realizable turbulence model is used. The behavior of the shell side temperature difference and total transfer rate is as expected. That is, the shell side outlet temperature decreases by increasing the mass flow rate. Also, the difference between the total heat transfer rates is reasonable.

In Table 3-5, it is observed that, among the considered cases, the $k-\varepsilon$ realizable turbulence model with the first order discretization and a fine mesh (case F) gives reasonable results. Therefore it is selected as the best modeling approach.

In this part of the study, the shell-and-tube heat exchanger is modeled with six baffles which corresponds to B/D_s ratio of 0.96. This value is in the recommended region suggested by Bell-Delaware method as indicated in Figure 3-7, for $B_c=36\%$. But, as mentioned above, B/D_s should be reduced to improve the pressure drop results. Therefore, in the following section, increased number of baffle values (N_b) are considered for a fixed heat exchanger length.

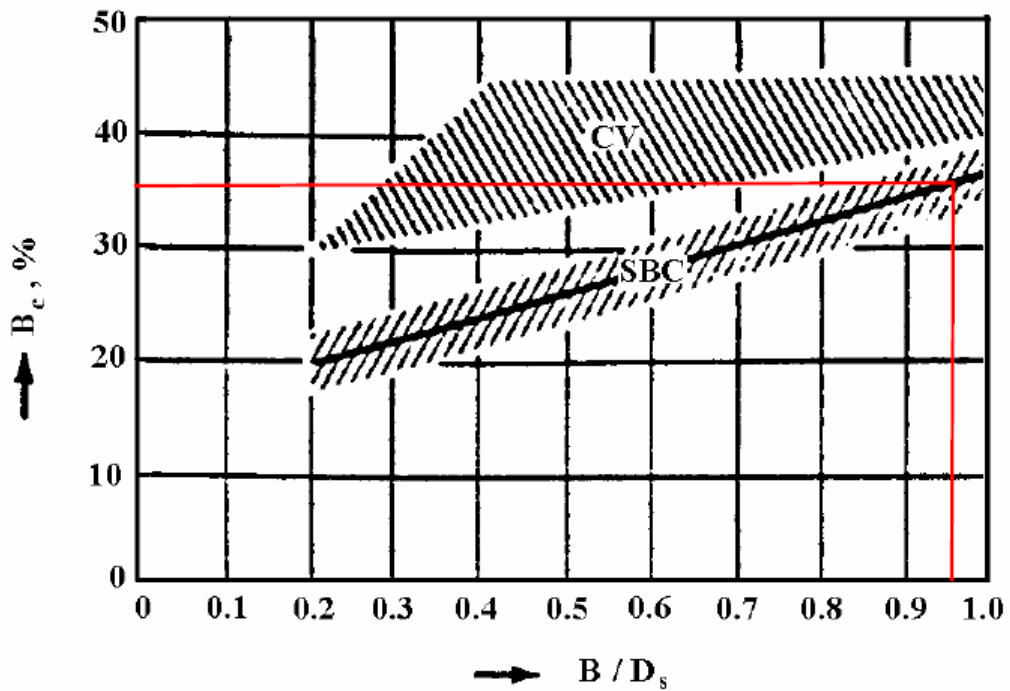


Figure 3-7 Bell-Delaware recommended segmental baffle cut values as a function of B/D_s ratio. SBC: segmental baffle cuts in no-phase-change flow; CV: baffle cuts applicable to condensing vapors (adapted from [15]).

3.3 Effect of Baffle Spacing on Pressure Drop and Heat Transfer

In this section, effect of baffle spacing on heat transfer and pressure drop is investigated for four different N_b values.

3.3.1 Pre-processing

In this section, the heat exchanger geometry in the previous section is used. The baffles are copied and moved to desired locations. The corresponding central baffle spacing and B/D_s ratio values are presented in Table 3-6.

After adjusting the baffle spacing and N_b , the model is re-meshed using the previous mesh parameters that are used for the finer mesh. The number of elements is increased to 1,568,850 in twelve baffle case.

Table 3-6 Design parameters and fixed geometric parameters

Number of baffles, N_b	6	8	10	12
Central baffle spacing, B	86	62	48	40
B/D_s ratio	0.96	0.69	0.53	0.44
Number of elements	1,361,514	1,561,201	1,555,980	1,568,850

The $k-\varepsilon$ realizable turbulence model is used in this part with the first order discretization scheme. The boundary conditions used in the previous section is applied. For each model, three different shell-side mass flow rate values are applied.

3.3.2 Results and Discussion

The results of the CFD analysis for 6, 8, 10 and 12 baffles are tabulated in Table 3-7. Similar to the previous section, shell side outlet temperature, shell side pressure drop and total heat transfer rate values are obtained directly from the CFD runs. The heat transfer coefficient values are calculated as explained in Appendix D. In Table 3-8, the analytical calculation results are tabulated. The analytical calculations are performed as in Appendix E.

The percent differences between the analytical calculations and CFD analysis results are presented in Table 3-9. The analytical calculations are taken as base values for the percent difference calculations. In overall heat transfer calculation, the percent difference between the Kern method and the CFD results does not reduced. In all cases Kern method underpredicts the heat transfer coefficient. By decreasing baffle spacing (increasing N_b); the difference between CFD results and the Bell-Delaware method is reduced as expected.

Table 3-7 Results of the CFD analysis for $N_b = 6, 8, 10$ and 12

		Results of the CFD Analysis			
N_b	Mass Flow Rate (kg/s)	Shell Side Outlet Temp. (K)	Heat Transfer Coeff. (W/m²K)	Shell Side Pressure Drop (Pa)	Total Heat Transfer Rate (W)
6	0.5	340.4	2514	1522	84853
	1	330.18	3757	6168	131785
	2	326.64	6768	24963	240506
8	0.5	341.35	2699	2206	89706
	1	334.64	4268	8634	145517
	2	332.03	7811	34371	268975
10	0.5	344.63	2869	3042	94160
	1	337.72	4736	11944	159624
	2	335.38	8784	47191	298677
12	0.5	346.34	3015	3980	98289
	1	340.31	5115	15435	170693
	2	338.36	9621	60930	323457

The percent difference for overall heat transfer prediction of CFD analyses is reduced, although, the recommended baffle cut ratio for Figure 3-7 is not satisfied for $N_b > 6$. For 0.5 kg/s and 1 kg/s mass flow rates, the difference decreased

below 10%, by adjusting B/D_s ratio. But, for 2 kg/s the percent difference is still high. The percent difference for pressure drop predictions of CFD analyses is also reduced. In 12 baffle case, the difference is reduced below 10%. There is also a reduction in the percent difference of the total heat transfer rate in CFD predictions and analytical calculations. The percent difference is reduced below 2%, for 10 and 12 baffle cases.

Table 3-8 Results of the analytical calculations for $N_b = 6, 8, 10$ and 12

		Analytical Calculations			
		Kern Method	Bell-Delaware Method		
N_b	Mass Flow Rate (kg/s)	Heat Transfer Coeff. (W/m²K)	Heat Transfer Coeff. (W/m²K)	Shell Side Pressure Drop (Pa)	Total Heat Transfer Rate (W)
6	0.5	2147	2213	1248	84442
	1	3086	3311	4597	126125
	2	4489	5025	18640	222644
8	0.5	2572	2584	1975	86431
	1	3724	3961	7069	144782
	2	5427	5941	28720	267727
10	0.5	2976	2933	2618	93298
	1	4311	4432	10708	157669
	2	6285	6745	43969	295756
12	0.5	2984	3254	3758	96878
	1	4328	4921	15453	168509
	2	6318	7507	63819	320694

Table 3-9 Percent differences between analytical calculations and CFD analysis for $N_b = 6, 8, 10$ and 12

		Heat Transfer Coeff.		Press Drop	Total Heat Transfer Rate
Number of Baffles	Mass Flow Rate (kg/s)	% difference w.r.t. Kern Method	% difference w.r.t. Bell-Delaware	% difference	% difference
6	0.5	17.1	13.6	22.0	0.5
	1	21.7	13.5	34.2	4.5
	2	50.8	34.7	33.9	8.0
8	0.5	4.9	4.5	11.7	3.8
	1	14.6	7.7	22.1	0.5
	2	43.9	31.5	19.7	0.5
10	0.5	3.6	2.2	16.2	0.9
	1	9.9	6.9	11.5	1.2
	2	39.8	30.2	7.3	1.0
12	0.5	1.0	7.3	5.9	1.5
	1	18.2	3.9	0.1	1.3
	2	52.3	28.2	4.5	0.9

In Figures 3-8 to 3-11, velocity path lines for 6, 8, 10 and 12 baffles are given for shell side mass flow rate of 1 kg/s. In Figures 3-8 and 3-9, it is observed that the flow hits the baffle plates, and then the direction of the flow is changed. Therefore, the shell space behind the baffle is not effectively used for cross-flow, as marked with a red circle in Figure 3-8. Recirculation zones appear in these regions, as indicated with a red circle in Figure 3-9. In Figures 3-10 and 3-11, the flow seems to be well developed. Cross flow regime is extended throughout the shell volume and recirculation zones disappear. That explains the more accurate results

obtained for 10 and 12 baffles in Table 3-7. Considering that Bell-Delaware method was based on very large collection of data from operational heat exchangers (accepted designs), only an acceptable shell side design gives matching CFD results.

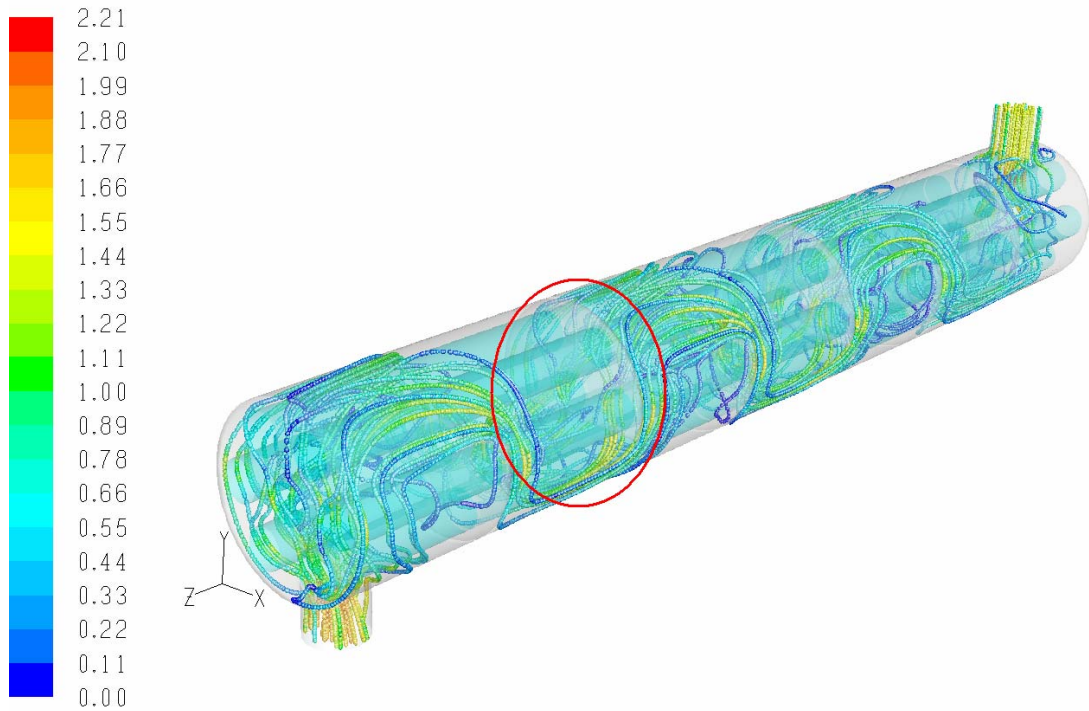


Figure 3-8 Velocity (m/s) path lines for 6 baffles (1 kg/s mass flow rate)

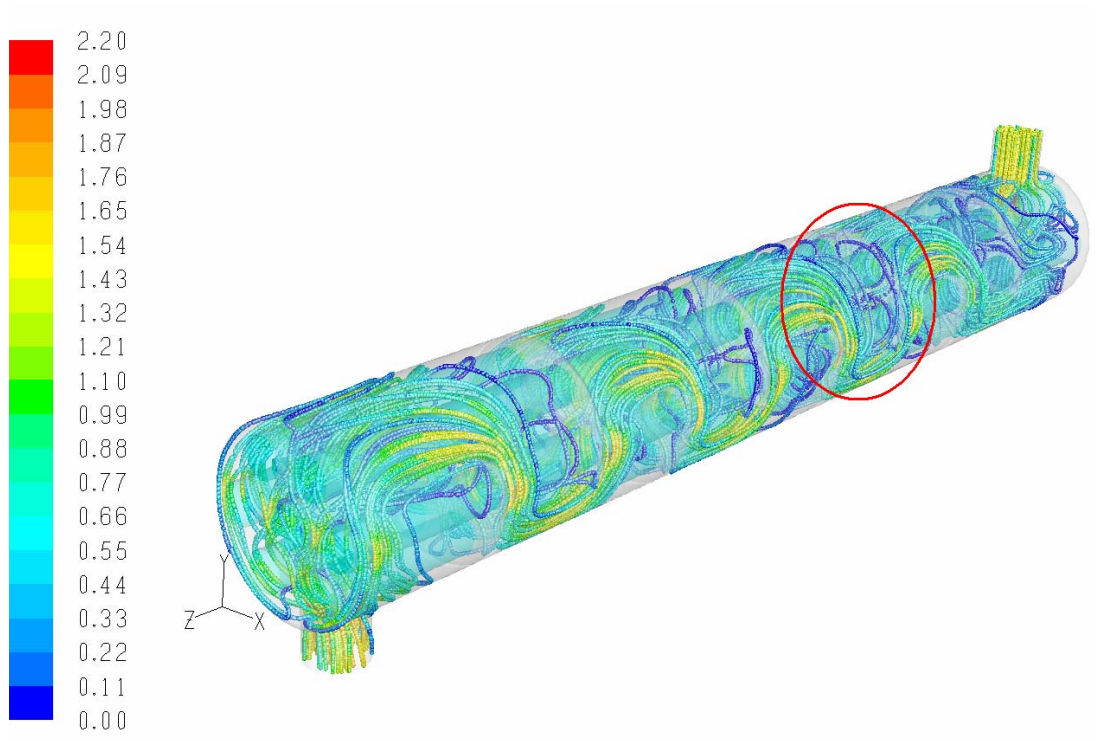


Figure 3-9 Velocity (m/s) path lines for 8 baffles (1 kg/s mass flow rate)

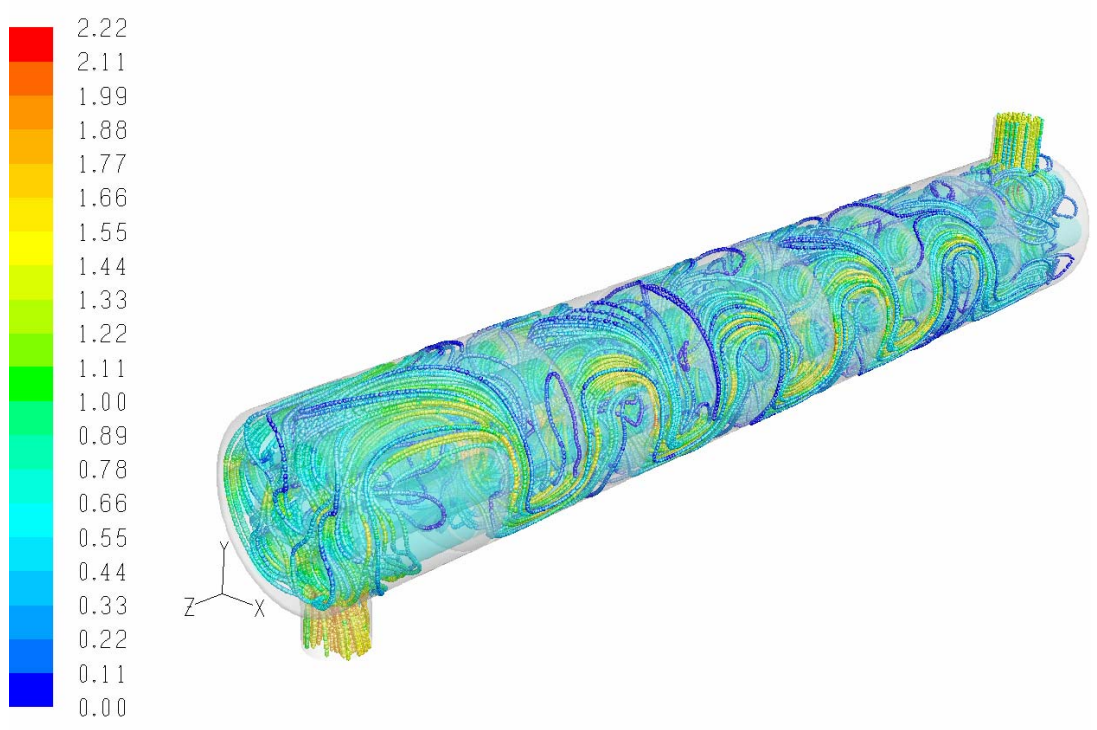


Figure 3-10 Velocity (m/s) path lines for 10 baffles (1 kg/s mass flow rate)

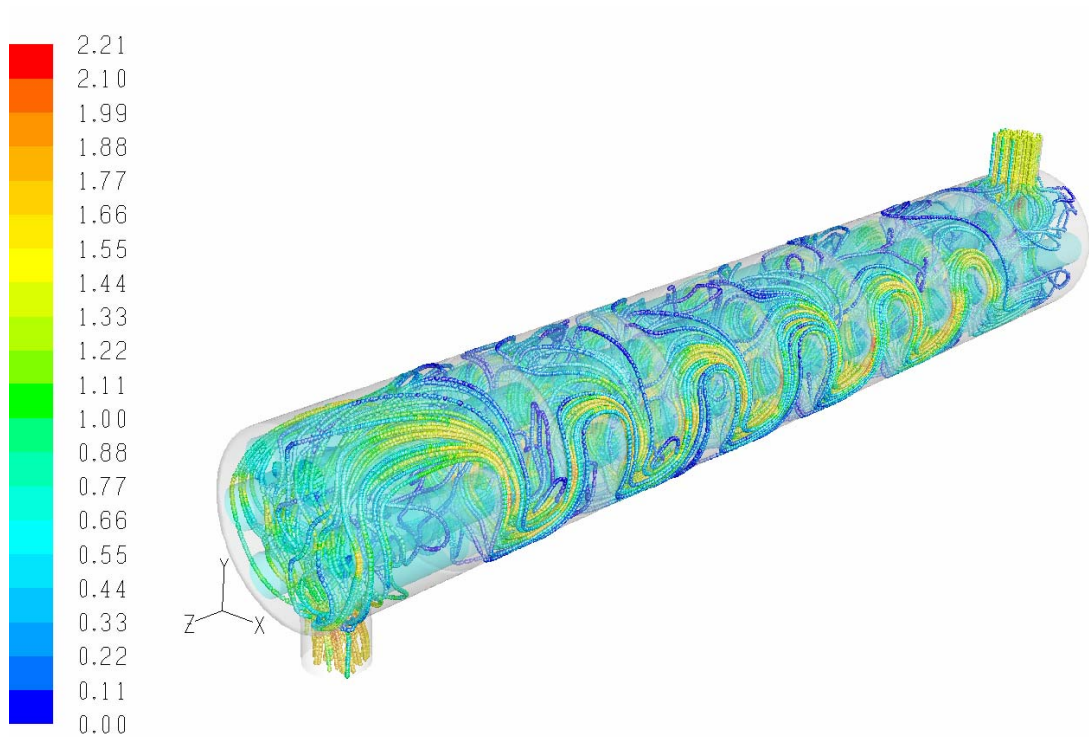


Figure 3-11 Velocity (m/s) path lines for 12 baffles (1 kg/s mass flow rate)

Detailed visualization of flow phenomenon in Figure 3-8 is illustrated in Figure 3-12. In this figure, path lines colored by velocity data are presented for the region that is marked with a red circle in Figure 3-8. The path lines are started at just below the fifth baffle; therefore, flow phenomenon in this compartment of the heat exchanger can be clearly observed. From Figure 3-12 it is observed that the shell space within a compartment is not effectively used for cross-flow. As explained before, flow hits the baffle, then the direction of the flow is changed.

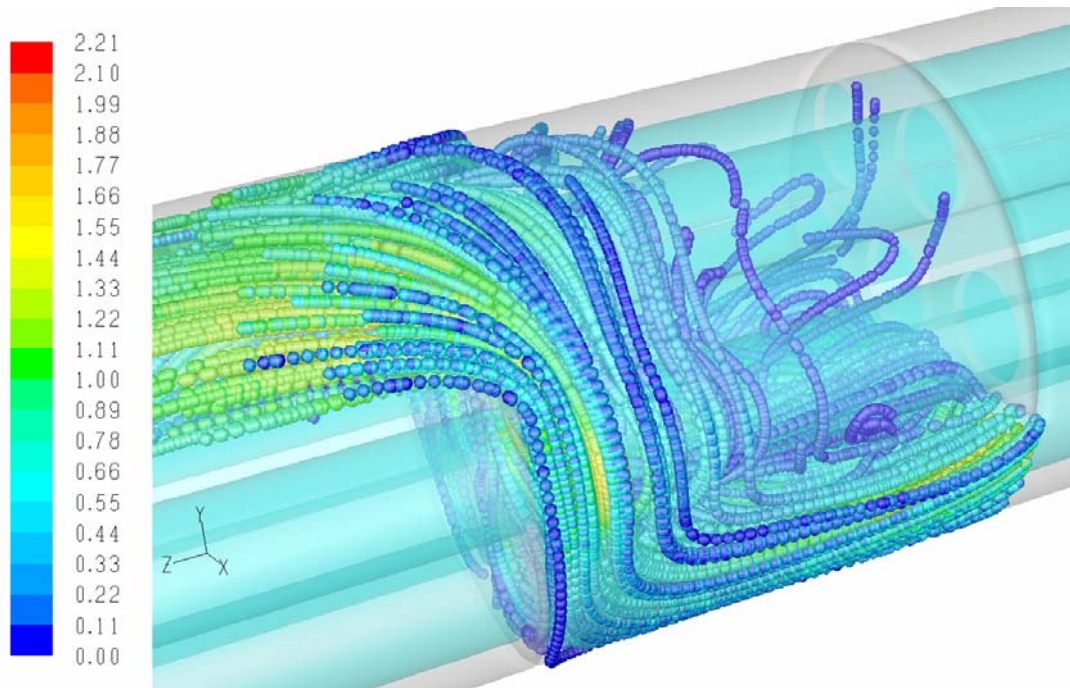


Figure 3-12 Detailed representation of velocity (m/s) path lines for 6 baffles case

Velocity profile in the z-direction in the compartment between fifth and sixth baffles is presented in Figure 3-13. The velocity profile presented in this figure is for the line passing between the first and second row of tubes, at the middle of the compartment. It is observed that, flow is not symmetrical about the center of the shell. Also, flow is comparatively slow in this region of the compartment. Because of the backflow region, there exist recirculation regions in the compartment. The backflow region has negative velocity values in the z-direction.

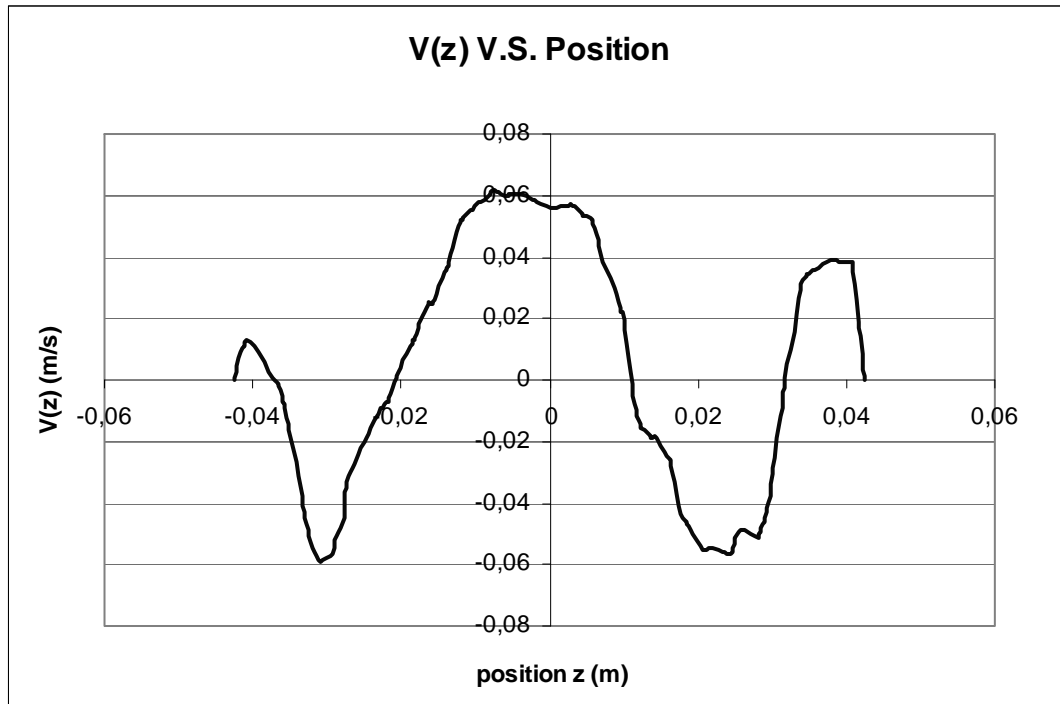


Figure 3-13 Velocity profile of the line passing through mid-plane of the compartment between first and second row of the tubes (for $N_b=6$)

The detailed flow phenomenon in Figure 3-9 is illustrated in Figure 3-14. In this figure, path lines colored by velocity data are presented for the region that is demonstrated by a red circle in Figure 3-9. The flow phenomenon in this compartment of the heat exchanger can be clearly observed by the path lines that are started at the middle of the compartment. It is observed that a recirculation region is present in this region and the shell volume is not used effectively for cross flow.

In Figure 3-15, velocity profile in the z-direction in the compartment between fifth and sixth baffles are presented. The velocity profile presented in this figure is for the line passing through centers of the first tube row. It is observed that, flow is approximately symmetrical about the center of the shell. In addition, flow is relatively slow in this region of the compartment. Backflow region in the Figure 3-14 illustrates the recirculation zone in the compartment.

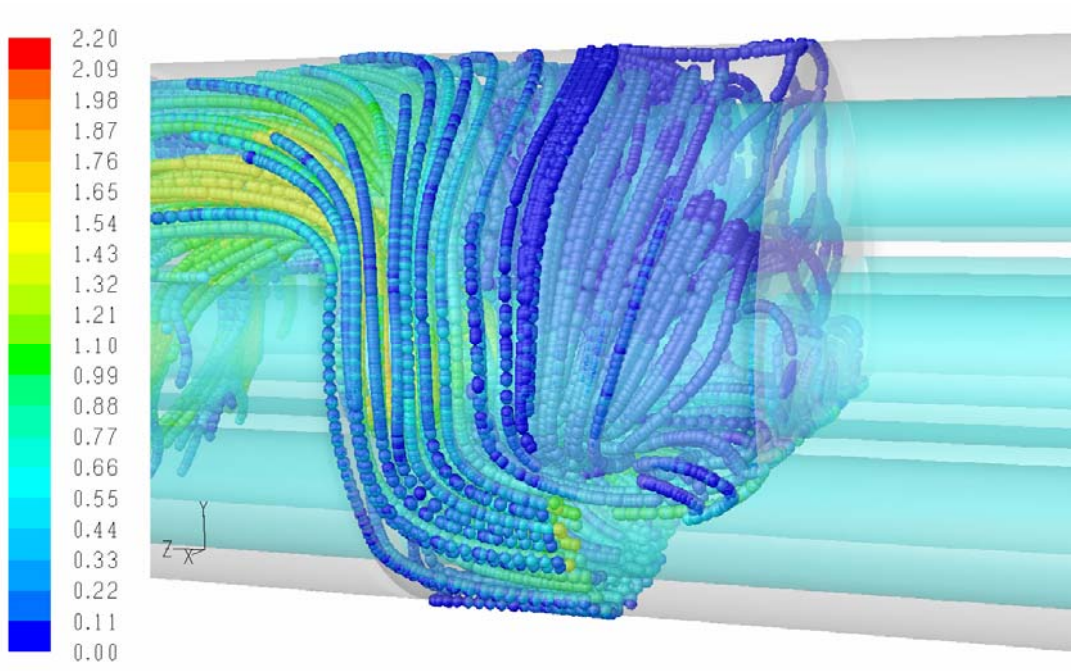


Figure 3-14 Detailed representation of velocity (m/s) path lines for 8 baffles case

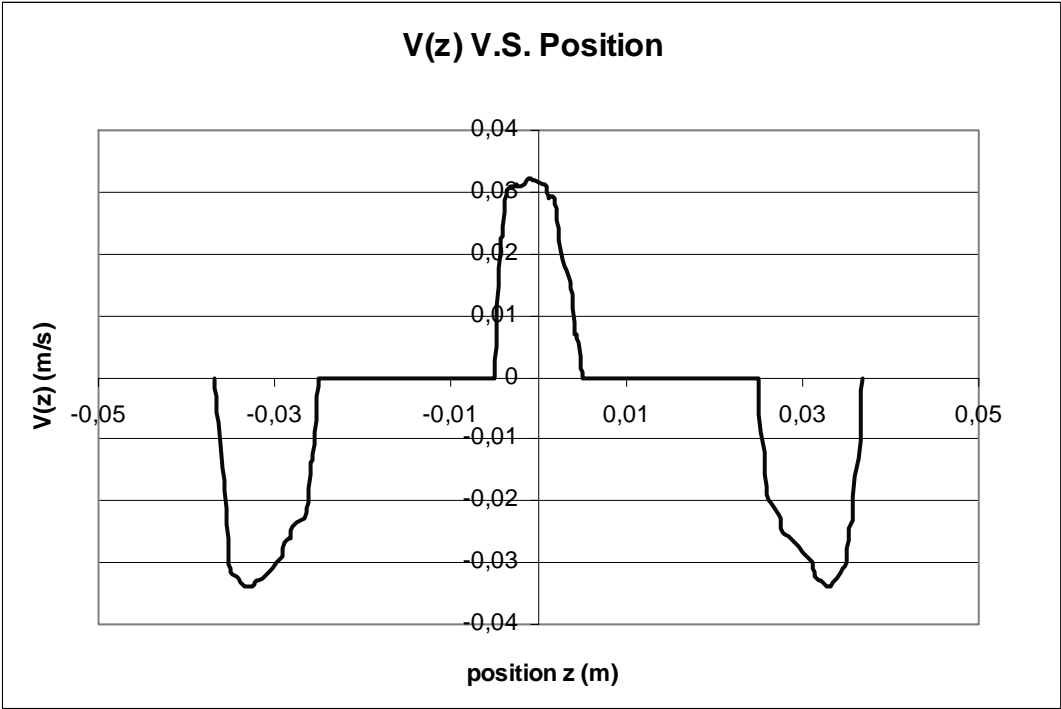


Figure 3-15 Velocity profile of the line passing through centers of the tubes of the first row (for $N_b=8$)

In Figures 3-16 and 3-17, velocity profiles in the z-direction in the baffle compartment between third and fourth baffles are presented for the twelve baffles case. The velocity profile presented in Figure 3-16 is for the line passing through centers of the first tube row. And the velocity profile presented in Figure 3-17 is for the line passing between the first and second row of tubes. It is observed that the magnitude of the velocity at the middle of the compartment is increased in twelve baffles case. Moreover, flow structure is improved, since backflow region is almost disappeared. Thus, recirculation is not expected in twelve baffles case.

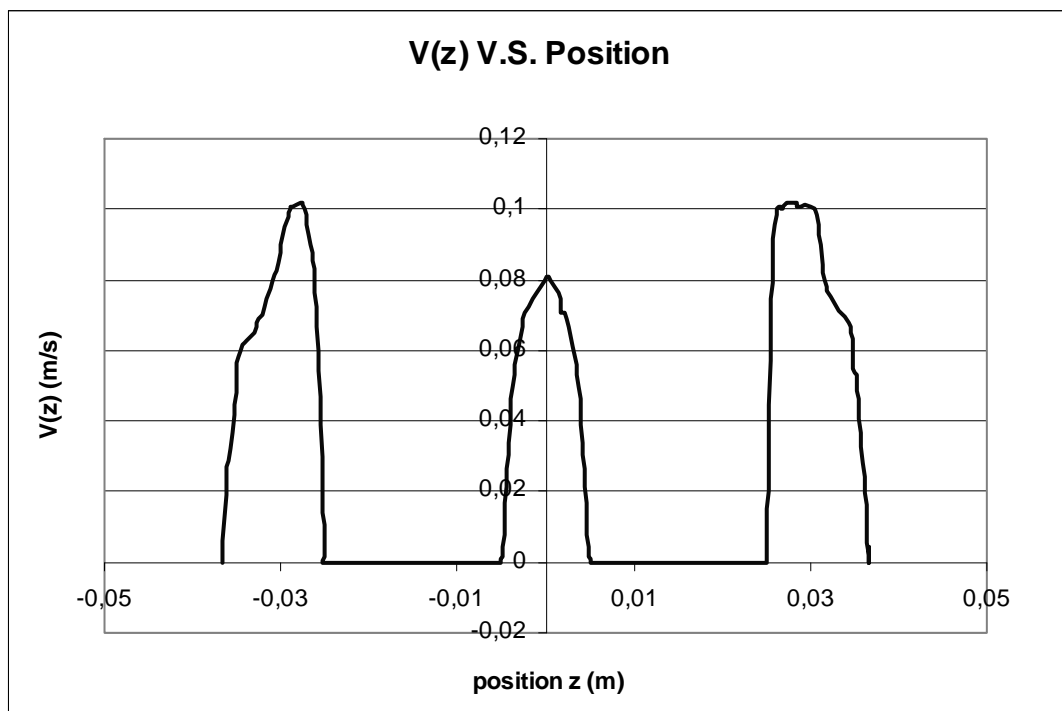


Figure 3-16 Velocity profile of the line passing through centers of the tubes of the first row (for $N_b = 12$)

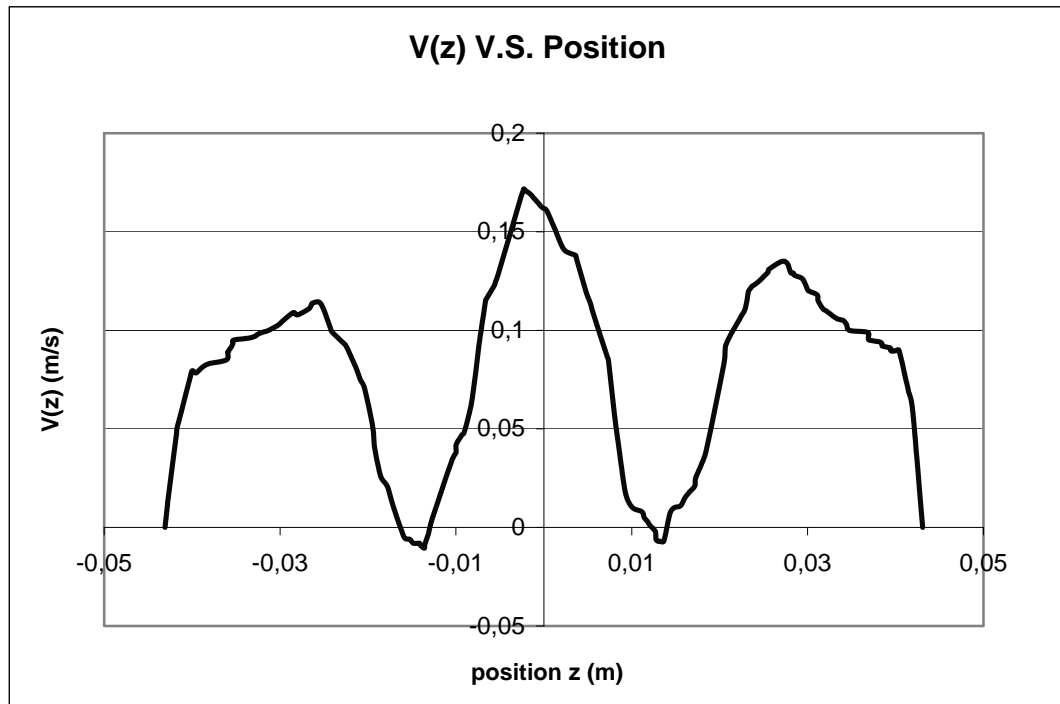


Figure 3-17 Velocity profile of the line passing through mid-plane of the compartment between first and second row of the tubes (for $N_b=12$)

3.4 Effects of Baffle Cut on Pressure Drop and Heat Transfer

In this section, effects of baffle cut on heat transfer and pressure drop is investigated. Similar to the previous section, for four different N_b values, simulations are performed for the baffle cut value of 25%.

The results of the CFD analysis for $B_c=25\%$ are tabulated in Table 3-10. Similar to the previous sections, shell side outlet temperature, shell side pressure drop and total heat transfer rate values are obtained directly from the CFD runs. In Table 3-11, the analytical calculation results are tabulated. The calculation procedure is same as the previous section.

The percent differences between the analytical calculations and CFD analysis results are presented in Table 3-12. The analytical calculations are taken as base

values for the percent difference calculations. To easily compare with the results of the previous section, results of the previous section is also included in Table 3-12.

From Table 3-12, for $N_b=6$ and $N_b=8$, it is observed that for heat transfer coefficient and pressure drop prediction, the difference between the CFD analysis and the analytical calculations are slightly reduced for $B_c =25\%$. But, for the total heat transfer rate prediction for $N_b=6$, CFD simulations give closer results for $B_c=25\%$, whereas, for $N_b=8$, CFD simulations give closer results for $B_c=36\%$.

Table 3-10 Results of the CFD analysis for $B_c =25\%$

Results of the CFD Analysis					
$N_b /$ $\%BC$	Mass Flow Rate (kg/s)	Shell Side Outlet Temp. (K)	Heat Transfer Coeff. (W/m²K)	Shell Side Pressure Drop (Pa)	Total Heat Transfer Rate (W)
6 / 25% BC	0.5	342.13	2628	2351	88124
	1	336.11	4362	9542	149654
	2	331.52	7484	37538	261235
8 / 25% BC	0.5	343.85	2813	3253	91672
	1	339.13	4929	12466	163971
	2	337.36	8854	51866	312401
10 / 25% BC	0.5	347.89	3170	4325	101459
	1	343.13	5611	18983	183474
	2	340.78	10389	75783	343186
12 / 25% BC	0.5	350.46	3378	6409	106834
	1	347.56	6300	25697	201920
	2	344.1	11228	111692	365547

From Table 3-12, for $N_b=10$, it is observed that for heat transfer coefficient and total heat transfer rate prediction, the difference between the CFD analysis and the analytical calculations are increased for $B_c=25\%$. But, for the pressure drop prediction, CFD simulations give closer results for $B_c=25\%$.

For $N_b=12$ and $B_c =25\%$, for heat transfer coefficient prediction, the difference between the CFD analysis and the analytical calculations are decreased for shell side mass flow rate value of 1 and 2 kg/s, whereas, for $m=0.5$ kg/s there is no such reduction in the heat transfer rate prediction. For pressure drop and total heat transfer rate prediction for shell side mass flow rate value of 0.5 kg/s gives closer results for $B_c =25\%$, however, for $m=1$ kg/s and $m=2$ kg/s the difference between the CFD simulations and analytical calculations are increased.

Table 3-11 Results of the analytical calculations for $B_c =25\%$

		Analytical Calculations			
		Kern Method	Bell-Delaware Method		
$N_b /$ $\%BC$	Mass Flow Rate (kg/s)	Heat Transfer Coeff. (W/m²K)	Heat Transfer Coeff. (W/m²K)	Shell Side Pressure Drop (Pa)	Total Heat Transfer Rate (W)
6 / 25% BC	0.5	2312	2401	1985	88062
	1	3631	3885	7197	150932
	2	5212	5832	28698	263460
8 / 25% BC	0.5	2680	2698	3036	92023
	1	4412	4587	10644	168569
	2	6248	7125	43584	318324
10 / 25% BC	0.5	3005	3343	4184	100108
	1	4842	5075	17185	180296
	2	7266	8042	70703	340926
12 / 25% BC	0.5	3339	3721	6204	105486
	1	5414	6276	23273	198834
	2	8106	9021	106230	368709

Table 3-12 Percent differences between analytical calculations and CFD analysis for $B_c = 25\%$ and $B_c = 36\%$

$N_b / \%BC$	Mass Flow Rate (kg/s)	Heat Transfer Coeff.		Press Drop	Total Heat Transfer Rate
		% difference w.r.t. Kern Method	% difference w.r.t. Bell-Delaware	% difference	% difference
6 / 25% BC	0.5	13.7	9.5	18.4	0.1
	1	20.1	12.3	32.6	0.8
	2	43.6	28.3	30.8	0.8
8 / 25% BC	0.5	5.0	4.3	7.1	0.4
	1	11.7	7.4	17.1	2.7
	2	41.7	24.3	19.0	1.9
10 / 25% BC	0.5	5.5	5.2	3.4	1.3
	1	15.9	10.6	10.5	1.8
	2	43.0	29.2	7.2	0.7
12 / 25% BC	0.5	1.2	9.2	3.3	1.3
	1	16.4	0.4	10.4	1.6
	2	38.5	24.5	5.1	0.9
6 / 36% BC	0.5	17.1	13.6	22.0	0.5
	1	21.7	13.5	34.2	4.5
	2	50.8	34.7	33.9	8.0
8 / 36% BC	0.5	4.9	4.5	11.7	3.8
	1	14.6	7.7	22.1	0.5
	2	43.9	31.5	19.7	0.5
10 / 36% BC	0.5	3.6	2.2	16.2	0.9
	1	9.9	6.9	11.5	1.2
	2	39.8	30.2	7.3	1.0
12 / 36% BC	0.5	1.0	7.3	5.9	1.5
	1	18.2	3.9	0.1	1.3
	2	52.3	28.2	4.5	0.9

3.5 Double Pipe Heat Exchanger Design

In this section, FLUENT analysis of a double pipe heat exchanger with a single tube is performed. A typical double pipe heat exchanger consists of two concentric pipes, one pipe placed inside the other. One fluid flows through the annulus, and the other fluid flows through the inner tube. The difference from the previous section is; here, the tube side flow is also modeled. In this analysis, the effect of the tube side inlet temperature and the annulus side mass flow rate on the heat transfer is analyzed. In Table 3-13, predetermined geometric parameters are presented. In Figure 3-18, double pipe heat exchanger model is presented.

The aim of this section is; to model a tubular heat exchanger by considering both the tube side and the shell side, and to visualize the flow phenomenon in a double pipe heat exchanger.

Table 3-13 Predetermined geometric parameters

Type of exchanger	single pass
Number of Tubes, N_t	single tube
Annulus Diameter, D_i	78 mm
Inner Tube Diameter, d_i	52 mm
Outer Tube Diameter, d_o	60 mm
Tube Wall Thickness	4 mm
Tube Thermal Conductivity, k	54 W/mK
Length of the Heat Exchanger, L	600 mm

Geometric and design parameters of the double pipe heat exchanger model is taken from the example problem of the textbook of the Kakaç and Liu [2]. The statement of the problem is given below:

Water at a flow rate of 5000 kg/h will be heated from 20 to 35°C by hot water. A 15°C hot water temperature drop is allowed. A number of 3.5 m hairpins of 3 in. by 2 in. Double-pipe heat exchangers with annuli and pipes each connected in series will be used. Hot water flows through the inner tube. Assume that the pipe is made of carbon steel. The heat exchanger is insulated against heat losses. Calculate the number of hairpins and the pressure drops.

In the simulations fouling is neglected for the shell and the tube side fluids. In the statement of the problem, it is mentioned that double-pipe heat exchangers each connected in series will be used and the length of the heat exchanger is given as 3.5m. Because of the grid size limitation, heat exchanger length is reduced to 0.6m to completely resolve the geometry. Thus, it is not possible to reach the required cold fluid temperature. This example problem is only a starting point for the heat exchanger model. It is not strictly followed.

The effect of the tube side inlet temperature and the annulus side mass flow rate on the heat transfer is analyzed by two set of simulations. For two different annulus side mass flow rate values, three different simulations are performed for different tube side inlet temperatures. Design parameters are tabulated in Table 3-14.

In Table 3-14, a capital letter is assigned to each annulus mass flow rate value and a number is assigned for each different simulation of corresponding mass flow rate value.

Table 3-14 Design parameters

	A-1	A-2	A-3
Tube Side Inlet Temperature (K)	349.5	359	368
Annulus Side Inlet Temperature (K)	293	293	293
Tube Side Mass Flow rate (kg/s)	1.36	1.36	1.36
Annulus Side Mass Flow rate (kg/s)	1.39	1.39	1.39

	B-1	B-2	B-3
Tube Side Inlet Temperature (K)	349.5	359	368
Annulus Side Inlet Temperature (K)	293	293	293
Tube Side Mass Flow rate (kg/s)	1.36	1.36	1.36
Annulus Side Mass Flow rate (kg/s)	0.7	0.7	0.7

3.5.1 Mesh Selection

Meshing details are presented in Table 3-15. Mesh parameters similar to the ones in the previous section are applied to the current model. For the steel and tube volumes, cooper type hex-wedge elements are used in meshing. Cooper scheme sweeps the mesh node patterns of specified "source" faces through the volume. Hex/Wedge meshing scheme specifies that the mesh is composed primarily of hexahedral elements but includes wedge elements where appropriate [20]. First, the inner wall and the side walls of the tube are meshed with quadrilateral elements. Then, the tube inner volume is meshed with a size function starting from "2", which is the value of the interval size of the tube inner wall. The growth rate is assigned as "1.05" and the end interval size is assigned as "4". Next, with hexagonal-wedge type elements and cooper scheme the tube solid volume is meshed. One important point on meshing contacting volumes is; meshes from different sides of the boundary should conform. In other words, they must share the same nodes. After completing the tube mesh, the annulus walls are meshed according to the given parameters. Finally, the annulus volume is meshed with tetrahedral-hybrid type elements.

The resulting mesh parameters are: 838,572 volume elements, with 103,786 mesh faces, 788 mesh edges and 459,737 nodes.

Table 3-15 Mesh details

	elements	type	interval size
surfaces			
tube side walls	quad	map	2
tube inner wall	quad	map	2
inlet & outlet nozzles	quad	pave	1
surface of nozzles	quad	pave	2
annulus wall (perpendicular to tubes)	quad	map	2
annulus outer wall	quad	pave	3
volume			
steel volume	hex-wedge	cooper	2
tube volume	hex-wedge	cooper	size function
annulus volume	tet-hybrid	hex-core	3

3.5.2 Boundary Conditions

According to Table 3-14, the annulus side and tube side inlet temperatures and the desired mass flow rates are specified as inlet boundary conditions. Next, zero gauge pressure is assigned to the tube and the annulus exits. As shown in Figure 3-18, the mass flow inlets are displayed as blue and the pressure outlets are displayed as red. Thus, counter flow conditions prevail in the model. All surfaces are defined as wall, and no slip condition is assigned to all surfaces. Assuming no heat loss through the annulus outer wall, zero heat flux boundary condition is assigned there.

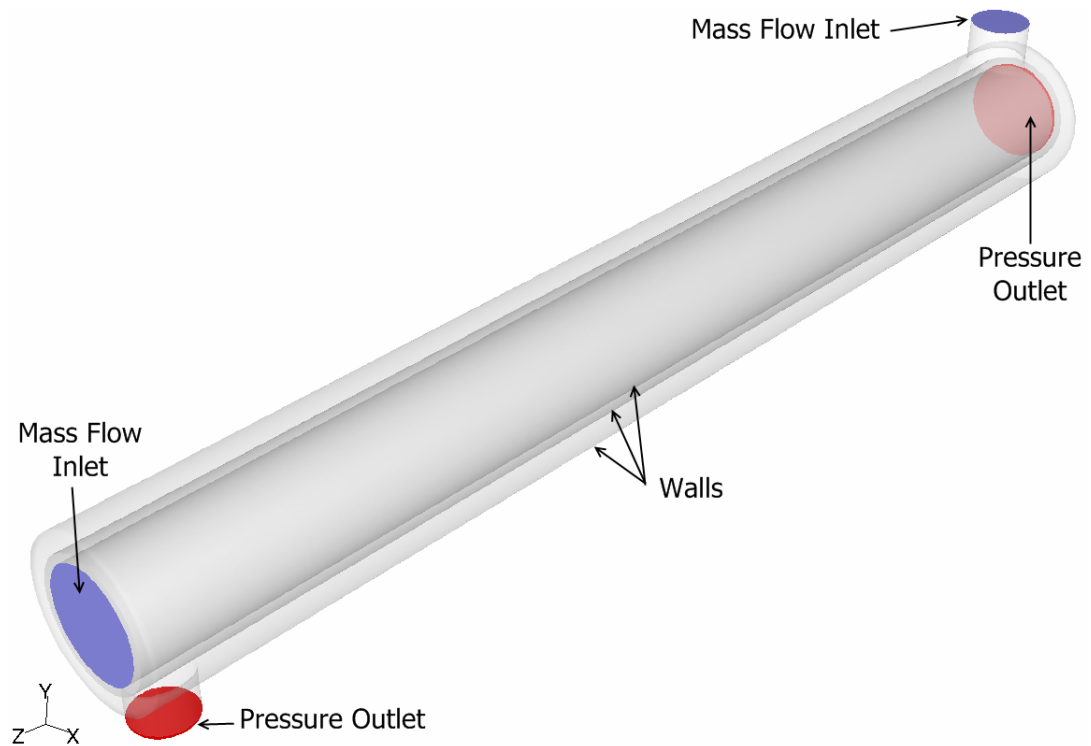


Figure 3-18 Double pipe heat exchanger

3.5.3 Other Modeling Choices

The $k-\varepsilon$ realizable turbulence model with the first order discretization is used in this part of the work. The convergence criterion for the pressure residual is defined as 10^{-6} , and for all other residuals it is taken as 10^{-3} .

3.5.4 Results and Discussion

The results of the CFD analysis for double pipe heat exchanger are tabulated in Table 3-16 and 3-17. Also, percent differences with respect to analytical calculations are presented in these tables. In Table 3-16 and 3-17 the results are presented for annulus mass flow rate of 1.39 kg/s and 0.7 kg/s, respectively. The total heat transfer rate, the outlet temperatures and pressure drop values for both fluids are obtained directly from the CFD runs. The analytical calculations are

performed using the appropriate correlations as presented in Kakaç and Liu [2]. The detailed sample calculation procedure is presented in Appendix F.

Table 3-16 Results of the CFD analysis for double pipe heat exchanger (for annulus mass flow rate of 1.39 kg/s)

		A-1	A-2	A-3	
Annulus Side	Boundary Conditions	Mass Flow Rate (kg/s)	1.39	1.39	1.39
		Inlet Temperature (K)	293	293	293
	CFD Results	Outlet Temperature (K)	295.91	296.05	296.23
		Pressure Drop (Pa)	7609	7440	7434
		Total Heat Transfer rate (W)	8275	9493	10981
Tube Side	Boundary Conditions	Mass Flow Rate (kg/s)	1.36	1.36	1.36
		Inlet Temperature (K)	349.5	359	368
	CFD Results	Outlet Temperature (K)	346.37	355.31	364.17
		Pressure Drop (Pa)	67.77	67.72	67.77
Analytical Results	Pressure Drop (Pa) (annulus side)	4370	4370	4370	
	Pressure Drop (Pa) (tube side)	89.75	88.16	86.76	
	Overall Heat Transfer Coefficient (W/m ² K)	815	824	835	
	Total Heat Transfer rate (W)	9848	11677	13502	
% difference w.r.t. analytic calculations	Pressure Drop (annulus)	74.1	70.3	70.1	
	Pressure Drop (tube)	24.5	23.2	21.9	
	Total Heat Transfer Rate	16.0	18.7	18.7	

Table 3-17 Results of the CFD analysis for double pipe heat exchanger (for annulus mass flow rate of 0.7 kg/s)

			B-1	B-2	B-3
Annulus Side	Boundary Conditions	Mass Flow Rate (kg/s)	0.7	0.7	0.7
		Inlet Temperature (K)	293	293	293
	CFD Results	Outlet Temperature (K)	296.6	296.8	297.1
		Pressure Drop (Pa)	1917	1916	1911
		Total Heat Transfer rate (W)	7080	7988	9120
Tube Side	Boundary Conditions	Mass Flow Rate (kg/s)	1.36	1.36	1.36
		Inlet Temperature (K)	349.5	359	368
	CFD Results	Outlet Temperature (K)	346.69	356.35	365.41
		Pressure Drop (Pa)	67.77	67.72	67.72
Analytical Results	Pressure Drop (Pa) (annulus side)		1135	1135	1135
	Pressure Drop (Pa) (tube side)		89.67	88.03	86.74
	Overall Heat Transfer Coefficient (W/m ² K)		602	607	612
	Total Heat Transfer rate (W)		7287	8625	9847
% difference w.r.t. analytic calculations	Pressure Drop (annulus)		68.9	68.8	68.4
	Pressure Drop (tube)		24.4	23.1	21.9
	Total Heat Transfer Rate		2.8	7.4	7.7

From Table 3-16 and 3-17, it is observed that by decreasing the mass flow rate value of the annulus side; the temperature difference of the annulus side increases, whereas, the temperature difference of the tube side is decreases. Also,

the pressure drop value of the annulus side is decreases with decreasing mass flow rate, on the other hand, the tube side pressure drop is not affected, since the tube side pressure drop value is proportional to tube side mass flow rate. Moreover, total heat transfer rate and the overall heat transfer coefficient of the heat exchanger is decreased by decreasing annulus side mass flow rate.

In Table 3-16 and 3-17, for the tube side, the pressure drop predictions of the CFD simulations are 20-25 % higher than the analytical calculation results. Mesh density is the main reason of this difference. For a single tube, with the same geometry, CFD analysis is performed. This analysis is only focused on the tube side pressure drop. Single tube is successfully meshed by adapting boundary layer mesh. The resulting model has 572,502 volume elements. Tube side length is extended to obtain fully developed flow conditions. The resulting tube side pressure drop is 82.76 Pa. And, the difference with the analytical calculations is 8.5%. There may be a 10% uncertainty in the analytical methods. Thus, the calculated pressure drop value is acceptable.

In Table 3-16 and 3-17, for the annulus side, the pressure drop predictions of the CFD simulations are 70-75 % higher than the analytical calculation results. The main reason for this is; in analytical calculations, the annulus side velocity distribution is taken as uniform. But, in reality, the velocity of the annulus side fluid is not uniform for this type of geometry. As seen in Figure 3-19, fluid mainly flows through the lower part of the model in the annulus. The upper part of the model is not used effectively. Therefore, the annulus side velocity is not constant through the heat exchanger.

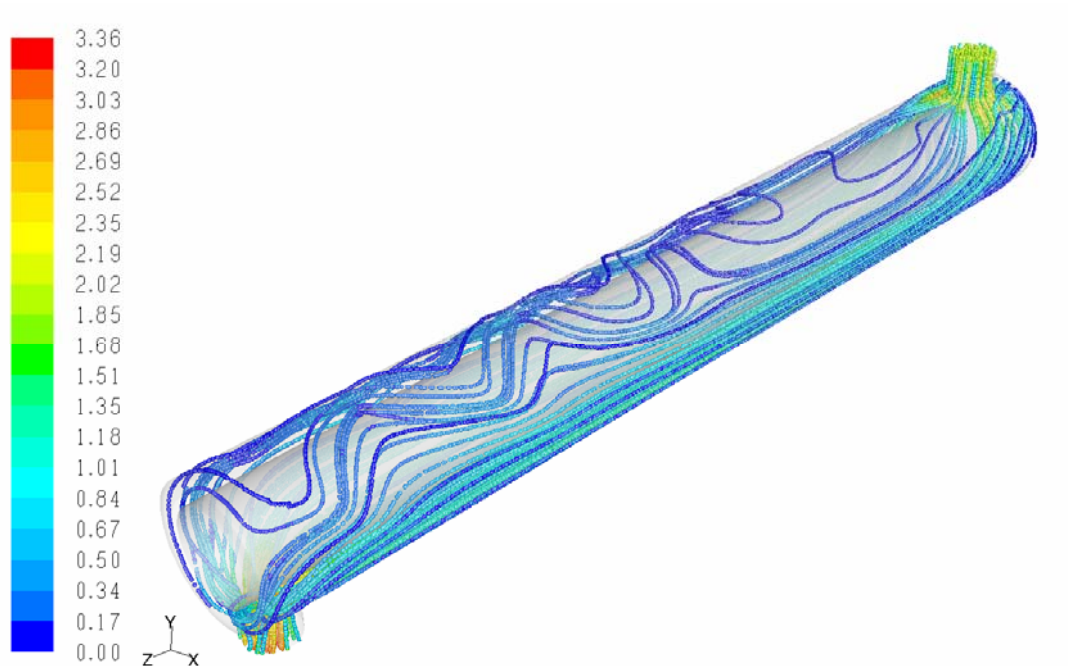


Figure 3-19 Velocity (m/s) path-lines for analysis A-1

Pressure drop is directly proportional to the square of velocity; therefore, there exist a big difference between the pressure drop values in the analytical calculations and the CFD runs for the shell-side. Figure 3-20 display the velocity vectors from the middle of the annulus in z-direction. As seen in Figure 3-20, the velocity vectors are denser at the lower part of the annulus. Moreover, in the model it is expected that the velocity path-lines would be mainly in the z-direction. However, it is observed that at the upper part of the model path-lines follow a wavy path.

In Figure 3-21, velocity versus radial position is presented. The velocity data presented for three different locations. Figure 3-22 shows the locations of the velocity data lines. Figure 3-21 is divided into two parts, to clearly present the velocity profile in the model. The left side is the lower part and the right side is the upper part of the annulus. The tube side velocity distribution is excluded, since

tube side flow is straightforward. The blue plot is the velocity data from the middle of the annulus ($z=0.3$). Other plots are from positions at $z=0.15$ and $z=0.45$.

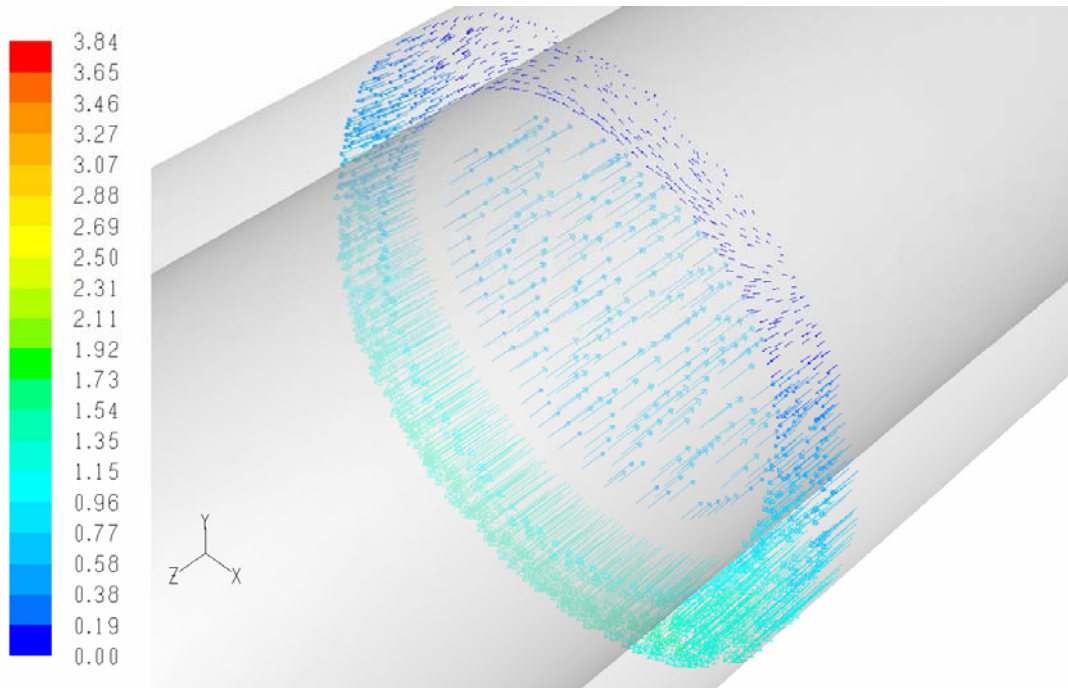


Figure 3-20 Velocity vectors (m/s) from middle of the annulus

In Figure 3-21, it is observed that the velocity distribution in the model is not uniform. In the upper part of the model, presented in right side, velocity of the flow increases in the z-direction, whereas; at the lower part of the model velocity of the flow decreases in the same direction.

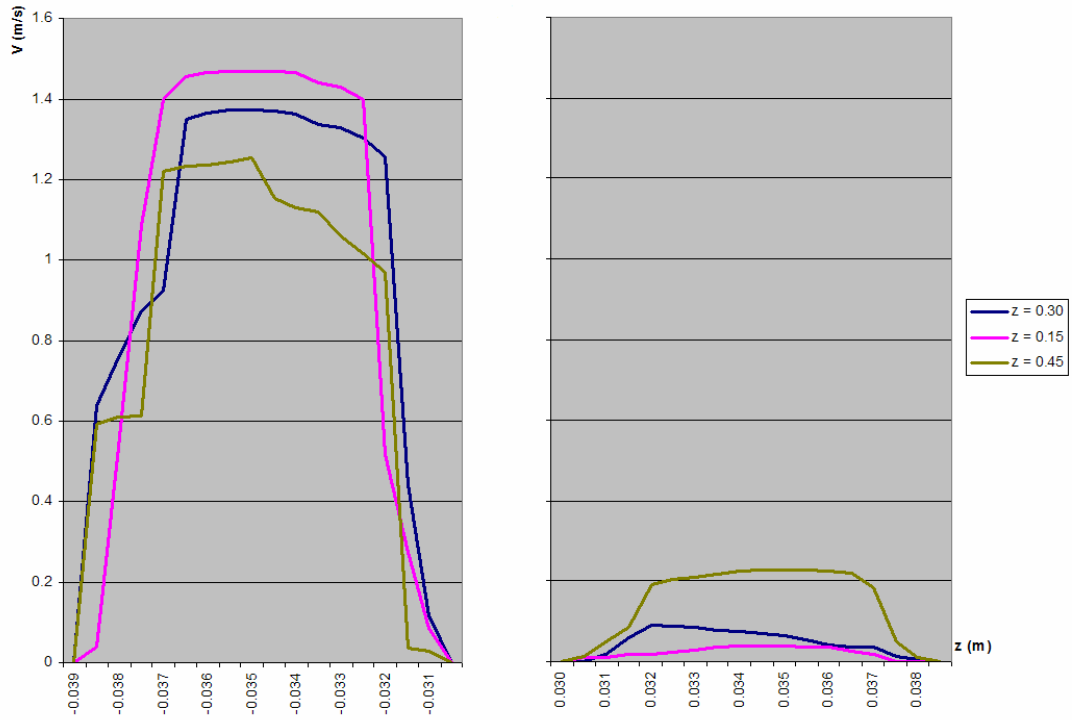


Figure 3-21 Velocity data versus annulus diameter

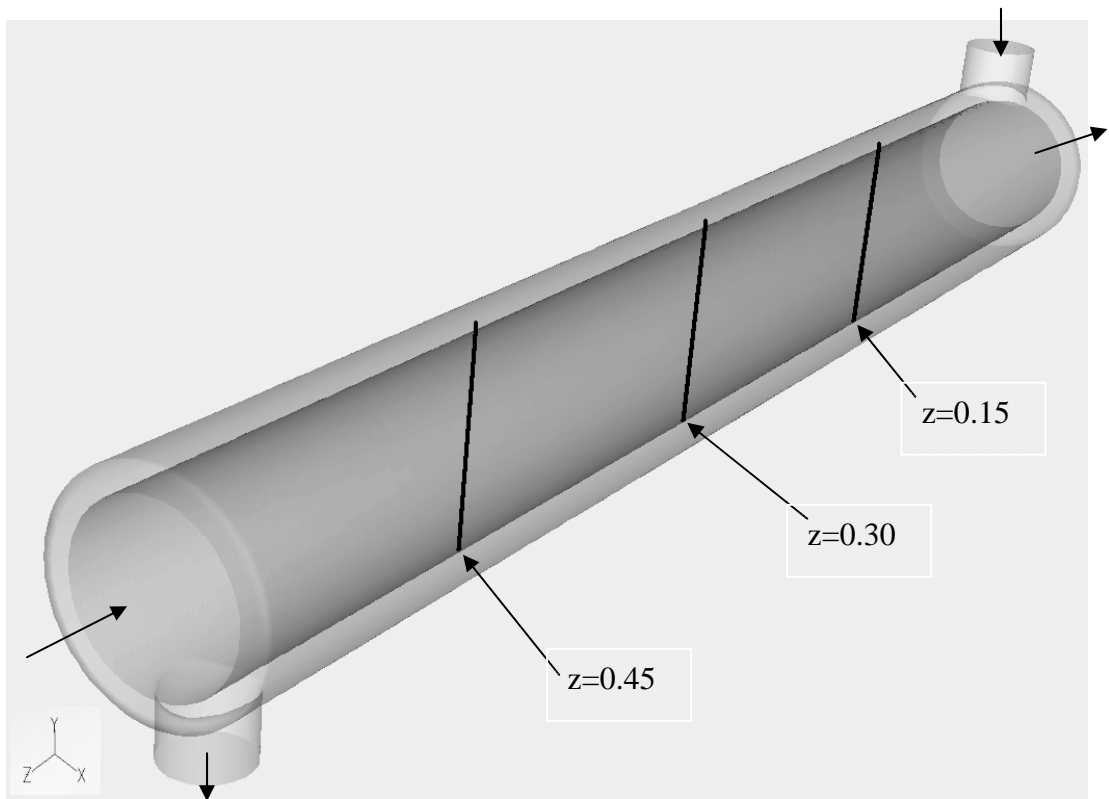


Figure 3-22 Locations of the velocity data lines

In conclusion, annulus should be narrowed to make the annulus velocity radially more uniform; however, it is still very difficult to obtain a constant velocity profile in the annulus. Moreover, several assumptions are present in the analytical calculation methods. One of the main assumptions in the annulus side calculations is; constant annulus side flow velocity. This analysis also shows a weakness of the analytical methods.

The main reason of the 75% difference between CFD simulations and the analytical calculations is the inlet and outlet nozzles, since, in analytical calculations the effect of inlet and outlet nozzles are not taken into account. Therefore, double pipe heat exchanger is remodeled without inlet and outlet nozzles, as displayed in Figure 3-23. The model is the same as the double pipe heat exchanger model that is used in this section, except the inlet and outlet nozzles. The mesh parameters that are discussed in section 3.5.1 are used for the current model. For this model the simulations are performed again using boundary conditions presented in Table 3-17. The model is extended to obtain fully developed flow conditions, but the results are presented for the design heat exchanger length of 600 mm.

The results are presented in Table 3-18 for the double heat exchanger without inlet and outlet nozzles. From Table 3-18, it is observed that the difference between the total heat transfer values between the CFD simulations and analytical calculations are reduced, except for the tube inlet temperature value of 349.5K. Again, for the tube side pressure drop, the difference between the CFD simulations and the analytical calculations are above 20%. But, as discussed above this problem is solved by increasing number of elements in the tube side.



Figure 3-23 Double pipe heat exchanger without inlet nozzles

The aim of performing the analyses presented in the Table 3-18, is to compare annulus side pressure drop. From Table 3-18 it is observed that, annulus side pressure drop values are below ten percent for double pipe heat exchanger without inlet and the outlet nozzles. One should note that, there may be a 10% uncertainty in the analytical methods. Thus, the calculated pressure drop value is acceptable.

Table 3-18 Results of the CFD analysis for double pipe heat exchanger (without inlet and outlet nozzles)

			C-1	C-2	C-3
Annulus Side	Boundary Conditions	Mass Flow Rate (kg/s)	0.7	0.7	0.7
		Inlet Temperature (K)	293	293	293
	CFD Results	Outlet Temperature (K)	295.7	295.9	296.2
		Pressure Drop (Pa)	139	139	139
		Total Heat Transfer rate (W)	7696	8458	9666
Tube Side	Boundary Conditions	Mass Flow Rate (kg/s)	1.36	1.36	1.36
		Inlet Temperature (K)	349.5	359	368
	CFD Results	Outlet Temperature (K)	347.37	356.65	365.31
		Pressure Drop (Pa)	68.48	68.49	68.49
Analytical Results	Pressure Drop (Pa) (annulus side)		153	153	153
	Pressure Drop (Pa) (tube side)		89.65	89.63	89.62
	Overall Heat Transfer Coefficient (W/m ² K)		598	602	607
	Total Heat Transfer rate (W)		7354	8575	9748
% difference w.r.t. analytic calculations	Pressure Drop (annulus)		9.3	9.3	9.3
	Pressure Drop (tube)		23.6	23.6	23.6
	Total Heat Transfer Rate		4.7	1.4	0.8

3.6 Conclusion

Final conclusion of this part suggests the following;

- Kern Method under predicts the heat transfer coefficient.
- Kern method gives conservative results.
- Bell-Delaware method gives better results for overall heat transfer coefficient calculation.
- The difference between CFD analyses and the analytical calculations increases by increasing the mass flow rate.
- Analytical methods under predict the pressure drop, if the window flow area is considerably less than the cross flow area.
- Among the considered cases, the $k-\varepsilon$ realizable turbulence model is suitable for the shell-and-tube heat exchanger design problem.
- By decreasing baffle spacing (increasing N_b); the difference between CFD results and the Bell-Delaware method is reduced as expected.
- The shell space behind the baffle is not effectively used for cross-flow for $B/D_s > 0.6$.
- Cross flow regime is extended throughout the shell volume and recirculation zones disappear for $B/D_s < 0.6$.
- The annulus side velocity is not uniform through the double pipe heat exchanger.
- The annulus of the double pipe heat exchanger should be narrowed to make the annulus velocity radially more uniform.

CHAPTER 4

FULL HEAT EXCHANGER SIMULATION

4.1 Introduction

In this part of the study, a full shell-and-tube heat exchanger simulation is performed by modeling both the shell side and the tube side. A commercially available, miniature shell-and-tube heat exchanger is modeled. Simulations are performed for two different types of flow arrangements; counter-current and co-current. Then, simulation results are compared with a sample run data of the miniature heat exchanger. In Figure 4-1, the side view of the heat exchanger is presented.

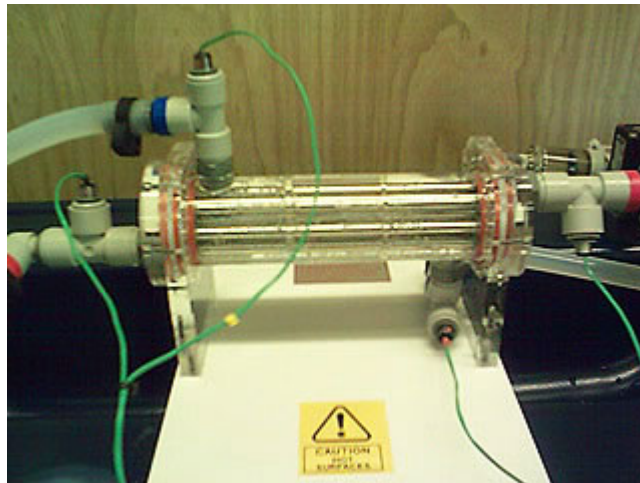


Figure 4-1 Miniature shell-and-tube heat exchanger (adapted from [28])

4.2 Model Details

The modeled miniature exchanger used in this study demonstrates the liquid to liquid heat transfer in a shell and tube heat exchanger. The heat exchanger consists of one shell and seven tubes with two transverse baffles in the shell. The schematic diagram of the heat exchanger is presented in Figure 4-2. In normal operation, the hot fluid from the hot water reservoir enters the header at one end of the shell and passes through the bundle of stainless steel tubes while the cold fluid from the cold water supply passes through the cylindrical shell. This arrangement minimizes the heat loss from the exchanger, since the ambient temperature is usually similar to average shell side temperature. Without additional insulation, the construction of the exchanger can be viewed. The outer annulus, headers, and baffles are constructed from clear acrylic to allow visualization of the heat exchanger construction and minimize thermal losses. The headers and outer shell incorporate the necessary tapings for sensors to measure the temperatures and for connections to the hot and cold water supplies. The heat exchanger is connected to a service unit [28]. The technical and geometrical details of the heat exchanger model are presented in Table 4-1.

Table 4-1 Technical and geometrical details of the heat exchanger

Shell size, D_s	39 mm
Shell wall thickness	3.0 mm
Tube outer diameter, d_o	6.35 mm
Tube inner diameter, d_i	5.15 mm
Tube wall thickness	0.6 mm
Number of tubes, N_t	7
Tube bundle geometry and pitch	Triangular, 11.35 mm
Heat exchanger length, L	144 mm
Heat transfer area	20,000 m ²
Baffle cut, B_c	37 %
Central baffle spacing, B	48 mm
Number of baffles, N_b	2
Inlet and outlet nozzles diameter	15 mm

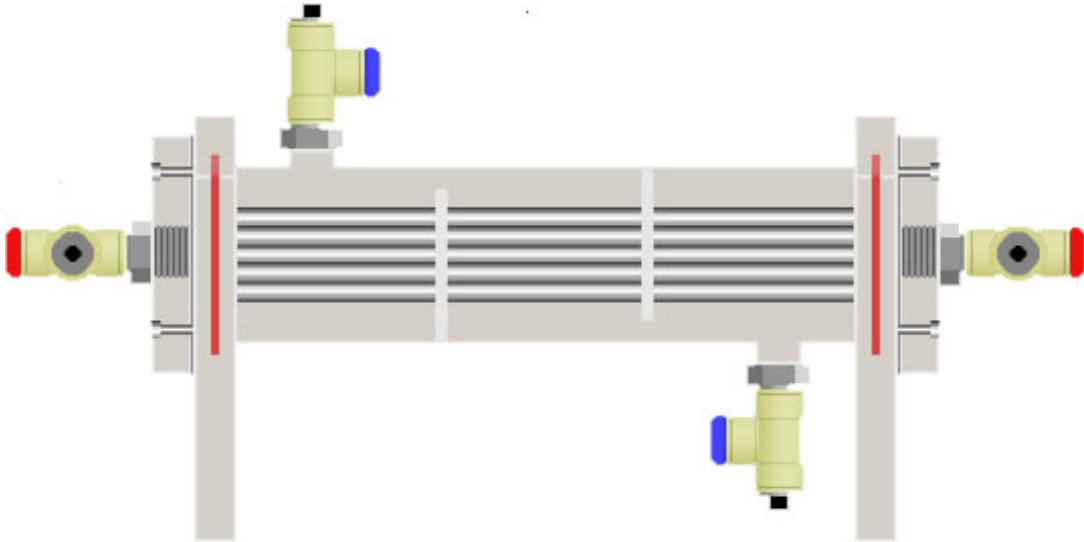


Figure 4-2 Schematic diagram of the heat exchanger (adapted from [28])

A sample experimental data of the heat exchanger model is obtained from CFU International Trade & Services Co. LTD and presented in Table 4-2. For two different flow arrangements, the sample data is presented. In simulations, inlet conditions are used as boundary conditions and fluid properties are taken from the sample data set.

4.2.1 Mesh Selection

Meshing details are presented in Table 4-3. Mesh parameters similar to the ones in the previous chapter are applied to current model. Since, the present model is smaller than the previous models, the interval sizes are decreased. First the tube volume and the steel volume are meshed using hex-wedge cooper elements. Then the surfaces of the shell are meshed according to the given parameters. Finally, the shell volume is meshed using tetragonal-hybrid type elements.

Resulting mesh parameters are: 920,837 volume elements, with 145,142 mesh faces, 2,128 mesh edges and 184,729 nodes.

Table 4-2 Sample experimental data of the miniature heat exchanger (The ambient temperature is not reported)

		units	counter-current	co-current
Hot water inlet temperature	T_1	°C	54.4	54.3
Hot water outlet temperature	T_2	°C	48.7	48.8
Reduction in hot temperature	ΔT	°C	5.7	5.5
Specific heat of hot water	$c_{p,h}$	kJ/kgK	4180.9	4180.9
Density of hot water	ρ_h	kg/m ³	987.3	987.3
Hot water mass flow rate	m_h	kg/s	0.0329	0.0329
Heat emitted from hot water	Q_e	kW	0.78	0.76
Cold water inlet temperature	T_3	°C	10.7	11
Cold water outlet temperature	T_4	°C	21.9	21.8
Increase in cold temperature	ΔT	°C	11.2	10.8
Specific heat of cold water	$c_{p,c}$	kJ/kgK	4184.3	4184.2
Density of cold water	ρ_c	kg/m ³	998.8	998.9
Cold water mass flow rate	m_c	kg/s	0.0167	0.0167
Heat absorbed by cold water	Q_a	kW	0.78	0.75
Heat lost		W	0.00	0.00
Overall efficiency		%	99.8	99.5

Table 4-3 Meshing details

	elements	type	interval size
surfaces			
shell wall (perpendicular to tubes)	quad	pave	1
baffle (thickness)	quad	map	0.5
baffle surfaces	quad	pave	1
inlet and outlet nozzles	quad	map	0.5
surface of nozzles	quad	pave	1
volume			
steel volume	hex-wedge	cooper	0.5
tube volume	hex-wedge	cooper	1
shell volume	tet-hybrid	hex-core	1

4.2.2 Boundary Conditions

The boundary conditions are applied according to Table 4-2. The inlet temperature and mass flow rate values are taken from the table. Mass flow rate boundary condition is applied to the shell side and the tube side. For the tube side, it is assumed that all the tubes have the same mass flow rate. For the shell inlet, to assign a non-uniform velocity, inlet nozzle of the model is extended. The details of the non-uniform velocity profile are discussed in Appendix C. Zero gauge pressure is applied to the pressure outlets. No slip boundary condition is applied to all other surfaces. Again, assuming no heat loss through the shell outer wall, zero heat flux boundary condition is assigned. As shown in Figure 4-3, the mass flow inlets are displayed as blue and the pressure outlets are displayed as red. The figure is for the counter-current analysis. For the co-current analysis, simply inlets and outlets of the tube side are changed.

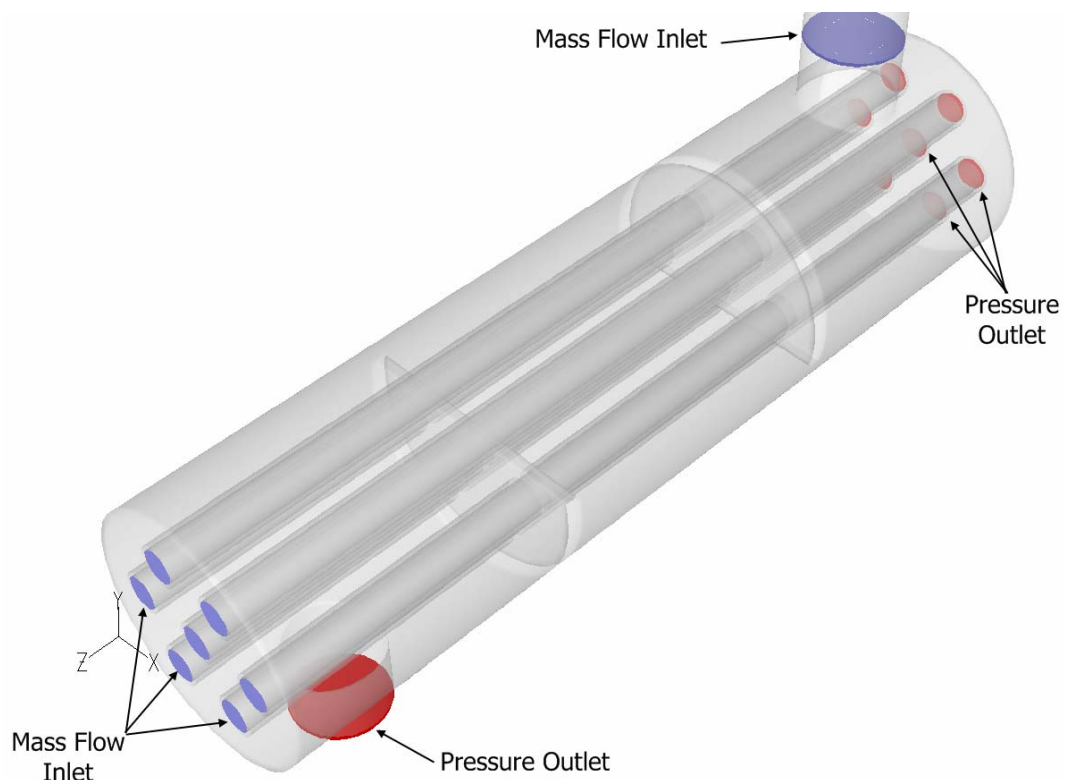


Figure 4-3 Boundary conditions

4.2.3 Other Modeling Choices

In the current model, both in the shell and tube sides, the flows are laminar, since for the shell and the tube sides Reynolds numbers are below 2300. Therefore, the laminar viscous model is selected. The first order discretization is selected for the pressure, momentum and energy equations. The convergence criterion for pressure residual is defined as 10^{-6} , and for all other residuals it is taken as 10^{-3} .

4.2.4 Results and Discussion

As explained before, the inlet temperature values are assigned as boundary conditions and for the outlet, only gauge pressure value of zero is assigned. The outlet temperatures for the both streams are calculated by the CFD simulations. Total heat transfer rate values are obtained from the tube walls of the CFD simulations.

The results of the CFD analysis for the counter-current and co-current flow arrangements are presented in Table 4-4. The simulation results are compared with the experimental data set. The simulation results have a good agreement with the experimental data set. Heat transfer rate values have 3-4 % percent difference between the experimental data and the CFD simulations. The difference between the shell side outlet temperatures is below 0.5 K. For the co-current flow arrangement the hot water outlet temperature value has an acceptable value. Only, for the counter-current simulation tube side outlet temperature value is higher than expected.

Table 4-4 Comparison of Results of the Experimental data and CFD results

			Experimental data	CFD results	% diff.
Counter-current arrangement					
HOT SIDE	Hot water inlet temperature	K	327,4	327,4	-
	Hot water outlet temperature	K	321,7	322,91	0.4
	Specific heat of hot water	kJ/kgK	4180,9		-
	Hot water mass flow rate	kg/s	0,0329		-
COLD SIDE	Cold water inlet temperature	K	283,7	283,7	-
	Cold water outlet temperature	K	294,9	294,44	0.2
	Specific heat of cold water	kJ/kgK	4184,3		-
	Cold water mass flow rate	kg/s	0,0167		-
	Heat transfer rate	W	0,78	0,76	2.6
Co-current arrangement					
HOT SIDE	Hot water inlet temperature	K	327,3	327,3	-
	Hot water outlet temperature	K	321,8	321,9	0.03
	Specific heat of hot water	kJ/kgK	4180,9		-
	Hot water mass flow rate	kg/s	0,0329		-
COLD SIDE	Cold water inlet temperature	K	284	284	-
	Cold water outlet temperature	K	294,8	295,2	0.1
	Specific heat of cold water	kJ/kgK	4184,3		-
	Cold water mass flow rate	kg/s	0,0167		-
	Heat transfer rate	W	0,75	0,78	4

For the co-current case, the tube side flow is represented well by the CFD simulations, whereas, for the counter-current case, the shell side is represented well. For the counter-current case, in CFD simulations the heat transfer rate is lower than the co-current case. Also, in the experimental data, the heat transfer rates for the two cases are almost equal. In addition, in CFD simulations, for the

co-current case the outlet temperature is higher than the counter-current case, for the shell side. In the simulations, the counter flow effects are not clearly observed. The effect of the counter flow will be dominant, if the heat exchanger length is extended.

In the Figure 4-4, the temperature distributions for the two cases are presented. The experimental data set is presented with continuous lines, and the CFD results are presented with dashed lines. For the co-current flow heat exchangers, temperature difference is expected initially large but decays rapidly in the z-direction. In contrast to co-current flow heat exchangers, counter-current flow heat exchangers provide for heat transfer between the hotter portions of the two fluids at one end, as well as between the colder portions at the other. Therefore, temperature difference with respect to heat exchanger length nowhere as large as it is for the inlet region of the co-current case [26].

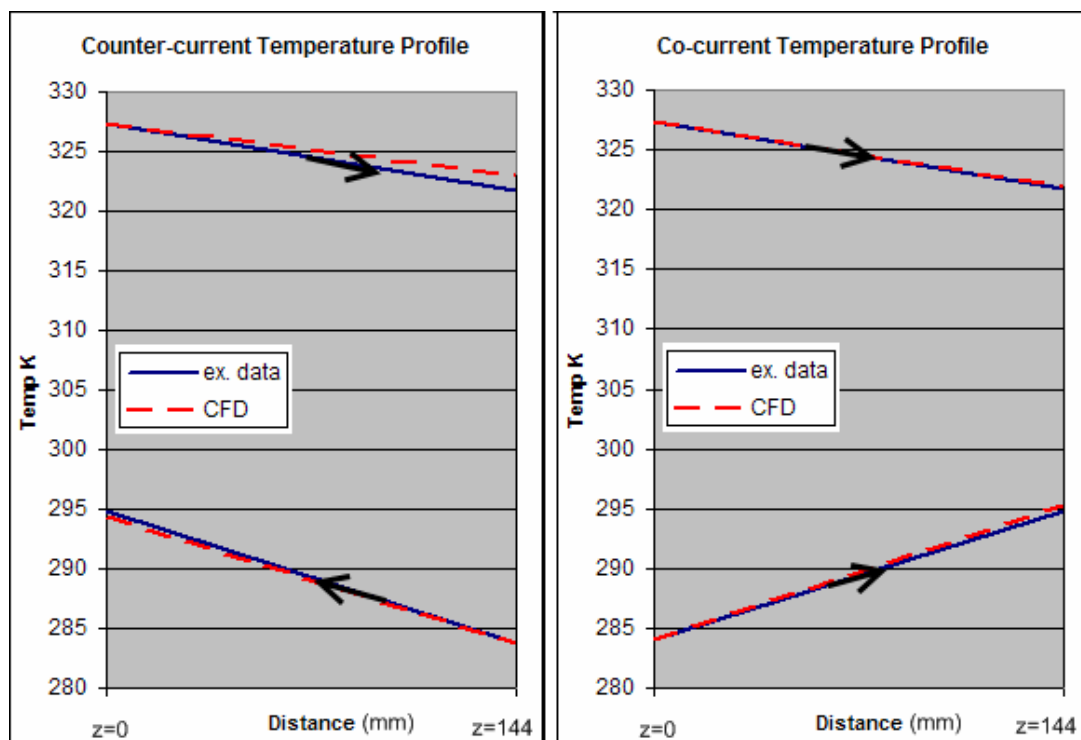


Figure 4-4 Temperature distributions for the two flow arrangements

In Figures 4-5 and 4-6, velocity path lines are presented for the counter-current and co-current case, respectively. The velocities in these figures are low, since the flow is laminar in the analyses. Similar to the six and eight baffle cases presented in Chapter 3, it is observed that flow hits the baffle, and then the direction of the flow is changed. Thus, the spaces behind the baffles are not effectively used and recirculation regions are developed in these regions. Baffle spacing should be reduced to use shell effectively.

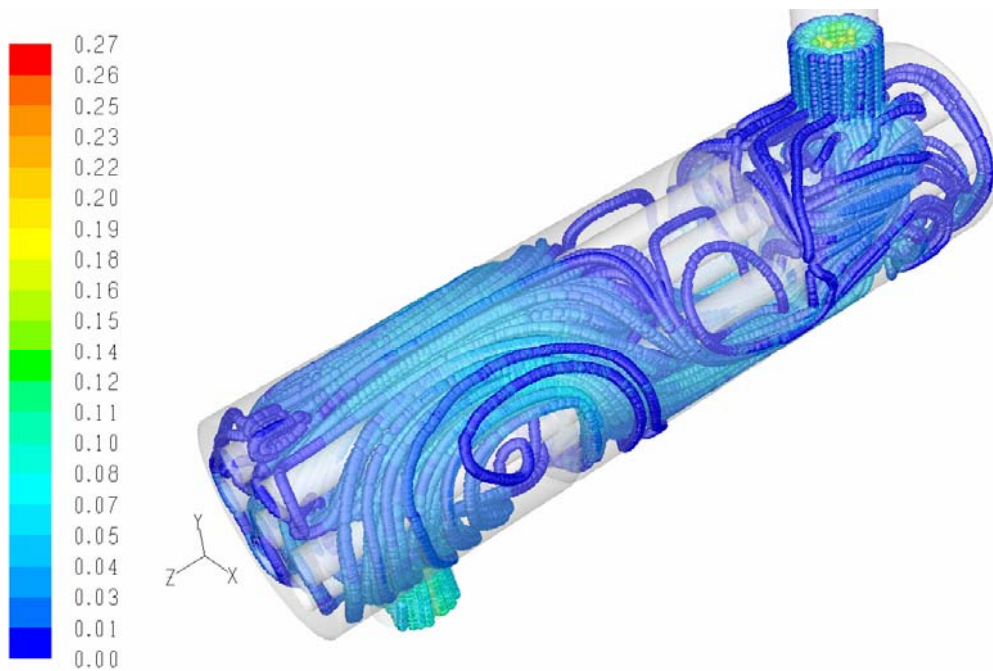


Figure 4-5 Velocity (m/s) path lines for the co-current case

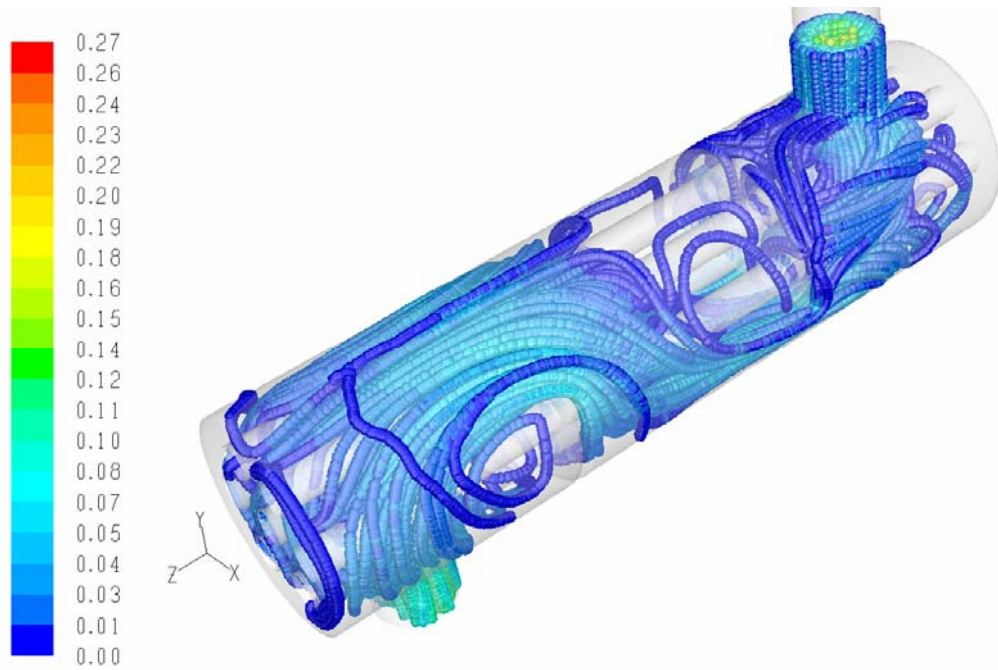


Figure 4-6 Velocity (m/s) path lines for the counter-current case

In the current study, to assign non-uniform velocity profile to shell-inlet, inlet nozzle is extended. In Figure 4-7, velocity profile at the inlet nozzle of the heat exchanger is given. It is observed that at low velocities and the near wall region the velocity graphs seem well fit. But, the maximum velocities are different in two graphs. The maximum value of the theoretical graph is higher than the numerical one.

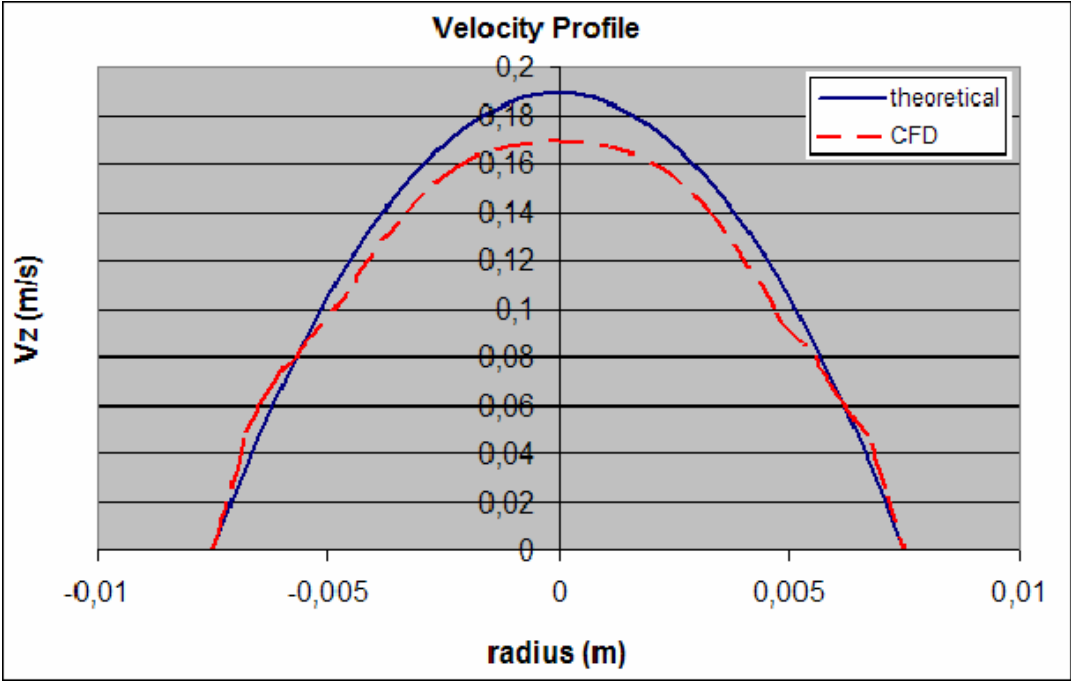


Figure 4-7 Velocity profiles at the shell inlet

CHAPTER 5

CONCLUSION

5.1 Comments on the Results

In this study, relatively small shell-and-tube heat exchangers are modeled and numerically analyzed using a commercial CFD software. The study is concentrated on the shell side flow, since the tube side flow is straightforward. Thus, the front and rear heads of the heat exchangers are not modeled.

The shell side of a small shell-and-tube heat exchanger is modeled with sufficient detail to resolve flow and temperature fields. From CFD simulation results, for fixed tube wall and shell inlet temperatures, the shell side heat transfer coefficient, pressure drop and heat transfer rate values are obtained. The sensitivity of the shell side flow and temperature distributions to the mesh density, the order of discretization and the turbulence modeling is observed. Various turbulence models are tried for the first and second order discretizations using two different mesh densities. By comparing with Bell-Delaware results, k - ε realizable turbulence model with the first order discretization and fine mesh is selected as the best simulation approach.

By changing the baffle spacing between 6 and 12, for 0.5, 1 and 2 kg/s shell side flow rates, the simulation results are again compared with the results from Kern and Bell-Delaware methods. It is observed that Kern method always under predicts heat transfer coefficient. For properly spaced baffles, it is observed that the CFD simulation results are in very good agreement with the Bell-Delaware results.

The effect of tube side flow is examined for a double pipe heat exchanger. In the analytical methods, it is assumed that, the annulus side velocity is uniform in double pipe heat exchangers and the average velocity is obtained from the corresponding mass flow rate. The CFD simulations showed that, the velocity distribution in the annulus is not uniform. There exists a considerable difference in velocity distribution between the upper and the lower parts of the heat exchanger. Therefore, the pressure drop in the analytical calculations and the CFD simulations did not coincide for the double pipe heat exchanger.

Flow structures that are visualized using the CFD simulations showed that for the smaller number of baffles, cross flow windows are not well utilized and some recirculation regions form behind the baffles. By increasing the number of baffles, this weakness is fixed and the heat transfer characteristics of the heat exchanger are improved.

The laminar viscous model is used for the full heat exchanger model. For the overall heat transfer coefficient and pressure drop values sample run data of the model was not available. Thus, only the outlet temperatures for both sides are compared for this model and they are found to be in good agreement. Using the laminar viscous model simplifies the simulation procedure.

As a general conclusion, it can be said that correlation based approaches may indicate the existence of a weakness in design, but CFD simulations can also pin point the source and the location of it. Using CFD, together with experiments, may speed up the shell-and-tube heat exchanger design process and may improve the quality of the final design.

5.2 Recommendations for Future Work

Because of the limitations of the number of the computational elements and the memory of the computers used in this study, the selected heat exchanger model is relatively small. The same computations may be repeated with a finer grid adaptation for understanding the effect of mesh resolution effectively. Enhanced

wall treatment option of FLUENT may be used with finer grids. By using finer grids, user may be able to resolve near wall region with its viscous sub-layer.

In section 3-2, only the shell side flow is modeled, and for the tube side a constant wall temperature is assigned. In future, the tube side should also be modeled.

In section 3-4, the annulus side velocity is not uniform. By adjusting, annulus and tube diameters velocity profile may be improved.

In the current study, it is assumed that all the tubes have the same mass flow rate, in other words, all the tubes have the same flow characteristics. But, because of the effects of the front and rear head flow distributions, flow characteristics in tubes differ. In future, the front and rear heads should also be modeled, and the effects of the heads should be investigated.

REFERENCES

- [1] Wikipedia Contributors, Wikipedia,
http://en.wikipedia.org/wiki/Shell_and_tube_heat_exchanger, last accessed at
June 2007.
- [2] S. Kakaç, H. Liu, "Heat Exchangers: Selection, Rating and Thermal Design" 2nd
ed., The CRC Press, Washington, D.C., 2002.
- [3] R. Mukherjee, "Effectively Design Shell-and-Tube Heat Exchangers," Chemical
Engineering Progress, vol. 94, pp.21-37, 1998.
- [4] D. Binicioğulları, "Comparative Study of Shell-and-Tube Heat Exchangers
Versus Gasketed-Plate Heat Exchangers", M.S. Thesis, METU, Turkey, 2001.
- [5] M. Prithviraj, M.J. Andrews, "Three Dimensional Numerical Simulation of Shell-
and-Tube Heat Exchangers. Part 1: Foundation and Fluid Mechanics," Numerical
Heat Transfer. Part A, Applications, vol. 33, pp. 799-816, 1998.
- [6] M.L. Sawley, "Numerical Simulation of the Flow around a Formula 1 Racing
Car", EPFL Supercomputing Review, EPFL-SCR No:9, Nov. 97.
- [7] M. Prithviraj, "Numerical Modeling of Flow and Heat Transfer in Shell-and-Tube
Heat Exchangers", Doctorate Dissertation, Texas A&M University, USA 1997.
- [8] W. T. Sha, C.I. Yang, T.T. Kao, S.M. Cho, "Multidimensional Numerical
Modeling of Heat Exchangers," Journal of Heat Transfer, vol. 104, pp.417-425,
1982.

- [9] M. Prithviraj, M.J. Andrews, "Three Dimensional Numerical Simulation of Shell-and-Tube Heat Exchangers. Part 2: Heat Transfer," Numerical Heat Transfer. Part A, Applications, vol. 33, pp. 817-828, 1998.
- [10] Z. Stevanović, G. Ilić, N. Radojković, M. Vukić, V. Stefanović, G. Vučković, "Design of Shell and Tube Heat Exchangers by Using CFD Technique – Part One: Thermo Hydraulic Calculation," Facta Universitatis Series: Mechanical Engineering, vol. 1, pp. 1091-1105, 2001.
- [11] Y.L. He, W.Q. Tao, B. Deng, X. Li, Y. Wu, "Numerical Simulation and Experimental Study of Flow and Heat Transfer Characteristics of Shell Side Fluid in Shell-and-Tube Heat Exchangers," Fifth International Conference on Enhanced, Compact and Ultra-Compact Heat Exchangers: Science, Engineering and Technology, Hoboken, NJ, pp. 29-42, Sep. 2005.
- [12] M.J. Andrews, B.I. Master, "Three-Dimensional Modeling of a Helixchanger Heat Exchanger Using CFD", Heat Transfer Engineering, vol.26, pp.22-30, 2005
- [13] V. De Henau, I. Ahmed, "Heat Exchanger Analysis Combining 1-D and 3-D Flow Modeling," ASME International Mechanical Engineering Congress and Exposition, Orlando, Florida, ASME Paper No. IMECE2005-79725, Nov. 5-11, 2005.
- [14] D.Q. Kern, "Process Heat Transfer", Mc-Graw-Hill, New York, 1950.
- [15] K.J. Bell, Delaware Method for Shell Side Design. In "Heat Exchangers: Thermal-Hydraulic Fundamentals and Design", S. Kakaç, A. E. Bergles, and F. Mayinger (Eds.), Hemisphere, New York, pp. 581-618, 1981.
- [16] U.C. Kapale, S. Chand, "Modeling for Shell-Side Pressure Drop for Liquid Flow in Shell-and-Tube Heat Exchanger," International Journal of Heat and Mass Transfer, vol. 49, pp. 601-610, 2006.

- [17] M. Prithviraj, M.J. Andrews, "Comparison of a Three-Dimensional Numerical Model with Existing Methods for Prediction of Flow in Shell-and-Tube Heat Exchangers", *Heat Transfer Engineering*, vol.20, pp.15-19, 2000.
- [18] D.A. Donohue, "Heat Transfer and Pressure Drop in Heat Exchangers", *Ind. Eng. Chem.*, vol. 41, pp. 2499-2511, 1949.
- [19] H.K. Versteeg, W. Malalasekera, "An Introduction to Computational Fluid Dynamics: The Finite Volume Method," 1st ed., Pearson, Essex, England, 1995.
- [20] Gambit 2.3 Users Guide
- [21] John Burkardt, RCM Ordering,
http://people.scs.fsu.edu/burkardt/f_src/rcm/rcm.html, last accessed at June 2007.
- [22] Fluent 6.3 Users Guide.
- [23] CFD-online Contributors, CFD-online, http://www.cfd-online.com/Wiki/Turbulence_intensity, last accessed at July 2007.
- [24] S. Kayılı, "CFD Simulation of Fire and Ventilation in the Stations of Underground Transportation Systems", M.S. Thesis, METU, Turkey, 2005.
- [25] Viable Computing, CFD Review,
<http://www.cfdreview.com/article.pl?sid=01/04/28/2131215>, last accessed at August 2007.
- [26] F.P. Incropera, D.P. Dewitt, "Fundamentals of Heat and Mass Transfer," J. Wiley, NY, 1996.

[27] R.S. Kistler, J.M. Chenoweth, "Heat Exchanger Shellside Pressure Drop: Comparison of Predictions with Experimental Data," Journal of Heat Transfer, vol. 110, pp.68-76, 1988.

[28] R. Graham, MIT Department of Chemical Engineering,
<http://heatex.mit.edu/Equipment.aspx#Heat%20Exchanger%20Experiments>, last accessed at August 2007.

[29] D.C. Wilcox, "Turbulence Modelling for CFD", Second Edition, DCW Industries Inc., 2000.

[30] National Institute of Standards and Technology,
<http://webbook.nist.gov/chemistry/fluid/>, last accessed at September 2007.

[31] M. H. Aksel, "Fluid Mechanics", Volume I, version 2.0, METU, Ankara, 1999.

APPENDIX A

THEORETICAL BACKGROUND ABOUT TURBULENCE MODELS

In this section, theoretical background about turbulence models that are used in the study is discussed in detail. The information on the turbulence models are gathered from the following references; Fluent Users Guide [22] and Turbulence Modeling for CFD [29].

A.1 Spalart-Allmaras Turbulence Model

The Spalart-Allmaras model is a one-equation model that solves a modeled transport equation for the turbulent viscosity. The Spalart-Allmaras model includes eight closure coefficients and three closure functions. For steady state, its defining equations are as follows [29];

$$\begin{aligned} \frac{\partial}{\partial x_i}(\rho \tilde{v} u_i) = \rho \tilde{v} C_{b1} \tilde{S} - C_{w1} f_w \rho \left(\frac{\tilde{v}}{d} \right)^2 + \\ \frac{1}{\sigma_{\tilde{v}}} \left[\frac{\partial}{\partial x_j} \left\{ (\tilde{v} \rho + \mu) \frac{\partial \tilde{v}}{\partial x_j} \right\} + C_{b2} \rho \left(\frac{\partial \tilde{v}}{\partial x_j} \right)^2 \right] + S_{\tilde{v}} \end{aligned} \quad (\text{A.1})$$

$$\mu_t = \rho f_{\nu 1} \tilde{v} \quad (\text{A.2})$$

Equation A.1 is the transport equation and Equation A.2 is the turbulent viscosity equation. In Equation A.1, $\sigma_{\tilde{v}}$ and C_{b2} are constants, ν is the molecular kinematic viscosity and $S_{\tilde{v}}$ is a user-defined source term. Auxiliary relations in the Spalart-Allmaras model are as follows:

$$\tilde{S} = S + \frac{\tilde{\nu}}{\kappa^2 d^2} f_{v2} \quad (\text{A.3})$$

$$S = \sqrt{2\Omega_{ij}\Omega_{ij}} \quad (\text{A.4})$$

$$\Omega_{ij} = \frac{1}{2} \left(\frac{\partial u_i}{\partial x_j} - \frac{\partial u_j}{\partial x_i} \right) \quad (\text{A.5})$$

$$f_{v1} = \frac{\chi^3}{\chi^3 + C_{v1}^3} \quad (\text{A.6})$$

$$f_{v2} = 1 - \frac{\chi}{1 + \chi f_{v1}} \quad (\text{A.7})$$

$$\chi = \frac{\tilde{\nu}}{\nu} \quad (\text{A.8})$$

$$f_w = g \left[\frac{1 + C_{w3}^6}{g^6 + C_{w3}^6} \right]^{1/6} \quad (\text{A.9})$$

$$g = r + C_{w2}(r^6 - r) \quad (\text{A.10})$$

$$r = \frac{\tilde{\nu}}{\tilde{S}\kappa^2 d^2} \quad (\text{A.11})$$

where f_{v1} is the viscous damping function, d is the distance from the wall for near wall treatment, S is a scalar measure of the deformation tensor and Ω_{ij} is the mean rate-of-rotation tensor. In Equation A.1, A.4 and A.5, i or $j = 1, 2, 3$ represents the three components of the variables in x, y and z direction.

And the closure coefficients are as follows:

$$C_{w1} = \frac{C_{b1}}{\kappa^2} + \frac{(1 + C_{b2})}{\sigma_{\tilde{\nu}}} \quad (\text{A.12})$$

$$C_{b1} = 0.1355 \quad C_{b2} = 0.622 \quad C_{v1} = 7.1 \quad \sigma_{\tilde{\nu}} = 2/3$$

$$C_{w2} = 0.3 \quad C_{w3} = 2.0 \quad \kappa = 0.4187$$

A.2 Standard k - ε Turbulence Model

The standard k - ε model is a semi-empirical model based on model transport equations for the turbulence kinetic energy k and its dissipation rate ε . k is the turbulence kinetic energy, and ε is the its dissipation rate. The model transport equation for k is derived from the exact equation, while the model transport equation for ε was obtained using physical reasoning [22]. For steady state, k and ε are obtained from the following transport equations:

$$\frac{\partial}{\partial x_i}(\rho k u_i) = \frac{\partial}{\partial x_j} \left[\left(\mu + \frac{\mu_t}{\sigma_k} \right) \frac{\partial k}{\partial x_j} \right] + G_k + G_b - \rho \varepsilon + S_k \quad (\text{A.13})$$

$$\frac{\partial}{\partial x_i}(\rho \varepsilon u_i) = \frac{\partial}{\partial x_j} \left[\left(\mu + \frac{\mu_t}{\sigma_\varepsilon} \right) \frac{\partial \varepsilon}{\partial x_j} \right] + C_{1\varepsilon} \frac{\varepsilon}{k} (G_k + C_{3\varepsilon} G_b) - C_{2\varepsilon} \rho \frac{\varepsilon^2}{k} + S_\varepsilon \quad (\text{A.14})$$

where G_k represents the production of turbulence kinetic energy and defined by Equation A.15, G_b is the generation of turbulence due to buoyancy is given by Equation A.16. $C_{1\varepsilon}$, $C_{2\varepsilon}$ and $C_{3\varepsilon}$ are constants. σ_k and σ_ε are the turbulent Prandtl numbers for k and ε respectively. S_k and S_ε are user defined source terms. In Equation A.13 and A.14, i or $j = 1, 2, 3$ represents the three components of the variables in x , y and z direction.

$$G_k = -\rho \overline{u_i' u_j'} \frac{\partial u_j}{\partial x_i} \quad (\text{A.15})$$

$$G_b = \beta g_i \frac{\mu_t}{Pr_t} \frac{\partial T}{\partial x_i} \quad (\text{A.16})$$

In Equation A.16, Pr_t is the turbulent Prandtl number for energy and is equal to 0.85, g_i is the component of the gravitational vector in the direction i , and β is the coefficient of thermal expansion.

Turbulent viscosity is defined by following equation:

$$\mu_t = \rho C_\mu \frac{k^2}{\varepsilon} \quad (\text{A.17})$$

where C_μ is a constant.

The model constants have the following values [29]:

$$C_{1\varepsilon} = 1.44 \quad C_{2\varepsilon} = 1.92 \quad C_\mu = 0.09 \quad \sigma_k = 1.0 \quad \sigma_\varepsilon = 1.3$$

A.3 Realizable k - ε Turbulence Model

The main differences between the realizable k - ε model and the standard k - ε model are; a new formulation for the turbulent viscosity included in the realizable model, and for the dissipation rate ε different transport equation is derived. In realizable k - ε model, for steady state, k and ε are obtained from the following transport equations:

$$\frac{\partial}{\partial x_j}(\rho k u_j) = \frac{\partial}{\partial x_j} \left[\left(\mu + \frac{\mu_t}{\sigma_k} \right) \frac{\partial k}{\partial x_j} \right] + G_k + G_b - \rho \varepsilon + S_k \quad (\text{A.18})$$

$$\frac{\partial}{\partial x_j}(\rho \varepsilon u_j) = \frac{\partial}{\partial x_j} \left[\left(\mu + \frac{\mu_t}{\sigma_\varepsilon} \right) \frac{\partial \varepsilon}{\partial x_j} \right] + \rho C_1 S \varepsilon + C_{1\varepsilon} \frac{\varepsilon}{k} C_{3\varepsilon} G_b - C_2 \rho \frac{\varepsilon^2}{k + \sqrt{\varepsilon \nu}} + S_\varepsilon \quad (\text{A.19})$$

where

$$C_1 = \max \left[0.43, \frac{\eta}{\eta + 5} \right] \quad (\text{A.20})$$

$$\eta = S \frac{k}{\varepsilon} \quad (\text{A.21})$$

$$S = \sqrt{2 S_{ij} S_{ij}} \quad (\text{A.22})$$

Note that, except for the model constants, Equation A.18 is the same as that in the standard k - ε model. In Equation A.19 a new model equation for dissipation rate ε is developed. In these equations, G_k and G_b are calculated similar to standard k - ε model; G_k is defined by Equation A.15 and G_b is given by Equation A.16. $C_{1\varepsilon}$ and C_2 are constants. σ_k and σ_ε are the turbulent Prandtl numbers for k and ε respectively. S_k and S_ε are user defined source terms. In Equation A.18 and A.19, i or $j = 1, 2, 3$ represents the three components of the variables in x, y and z direction.

Similarly, turbulent viscosity is defined by following equation:

$$\mu_t = \rho C_\mu \frac{k^2}{\varepsilon} \quad (\text{A.23})$$

where C_μ is a variable, and this is the another difference between the standard and the realizable k - ε turbulence models. Formulation of the C_μ is presented in Fluent User's Guide [22].

The model constants have the following values:

$$C_{1\varepsilon} = 1.44 \quad C_2 = 1.9 \quad \sigma_k = 1.0 \quad \sigma_\varepsilon = 1.2$$

APPENDIX B

WATER PROPERTIES IN THE SIMULATION RANGE

In simulations, the properties of water are redefined using piecewise-linear functions for density, thermal conductivity, viscosity and specific heat capacity of water. Piecewise-linear functions are defined for ten different intervals covering temperature range of the analysis. The range of temperature in the simulations is between 293 K and 450 K. In Figures B-1, B-2, B-3, and B-4 the behavior of the water properties in the simulation range is given. From these figures, it is observed that; the change of density, thermal conductivity, viscosity and specific heat capacity versus temperature can be approximated by using ten different temperature values. The figures used in this appendix are adapted from the webpage of the National Institute of Standards and Technology [30].

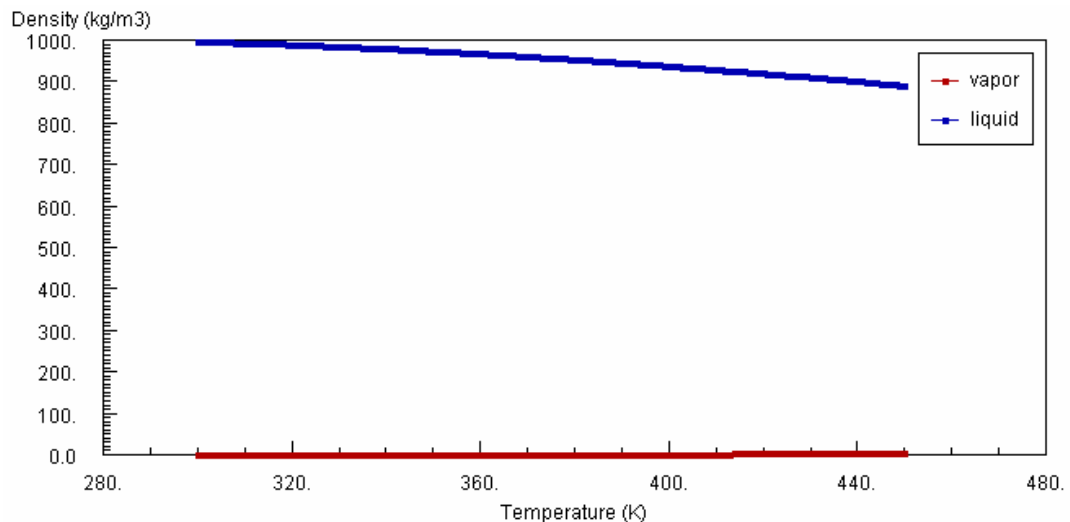


Figure B-1 Density of water versus temperature (adapted from [30])

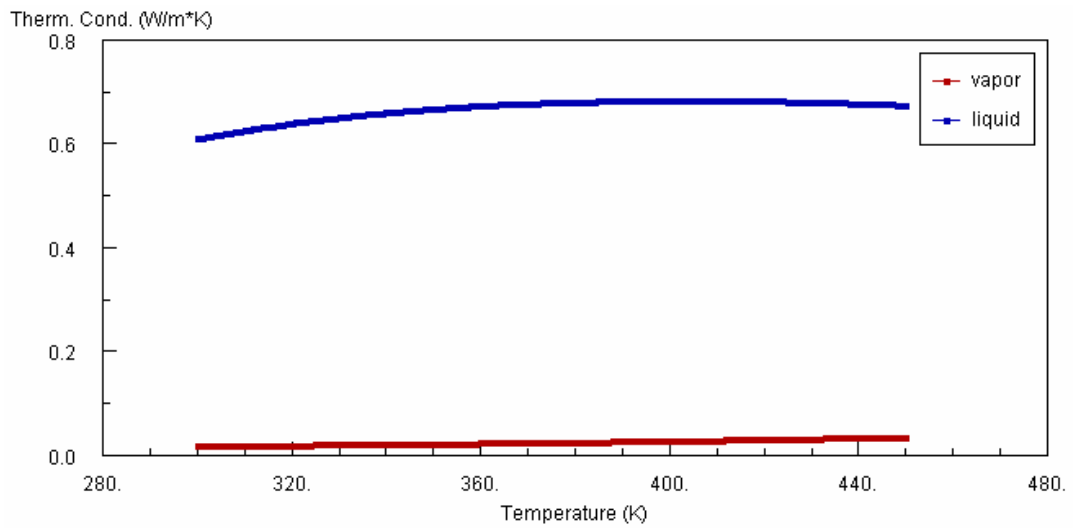


Figure B-2 Thermal conductivity of water versus temperature (adapted from [30])

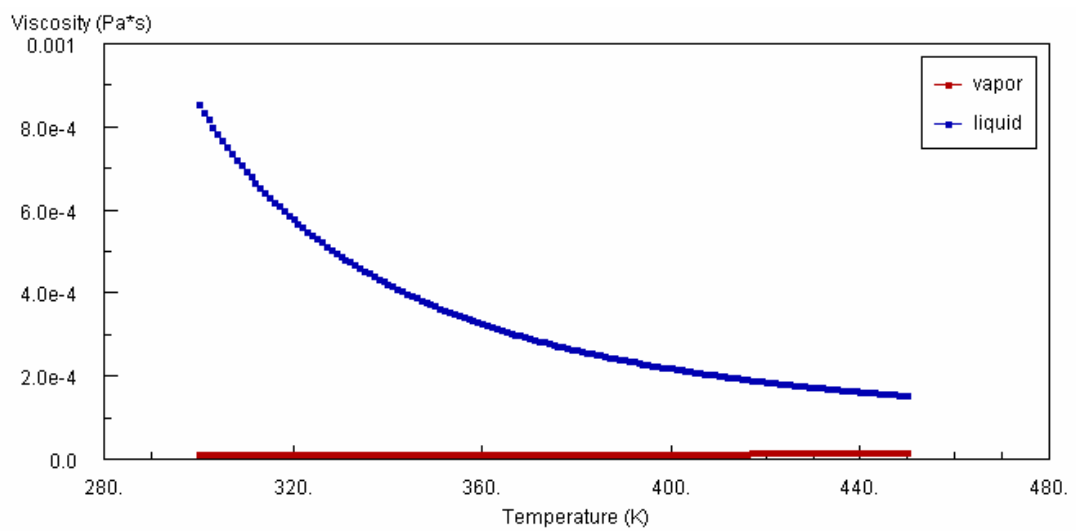


Figure B-3 Viscosity of water versus temperature (adapted from [30])

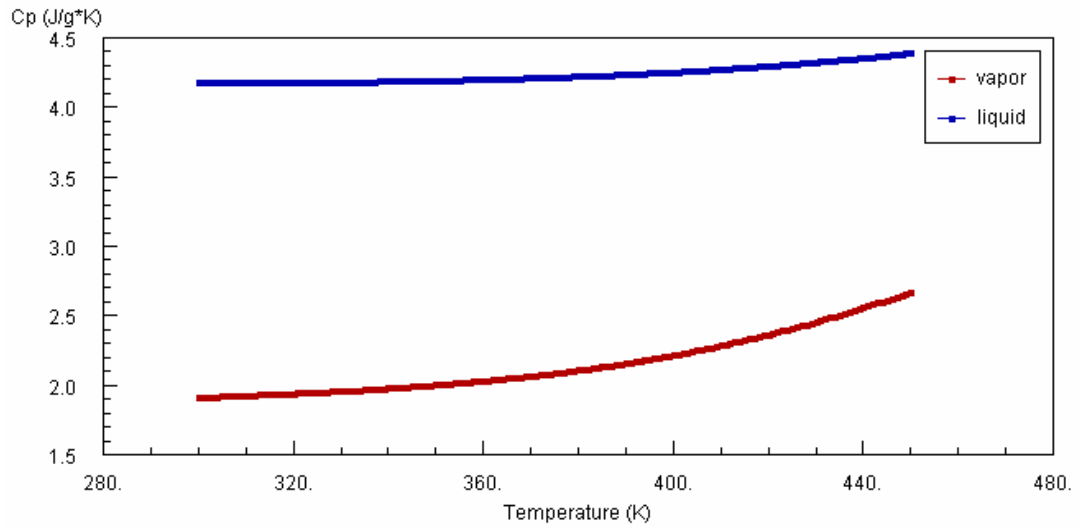


Figure B-4 Specific heat capacity of water versus temperature (adapted from [30])

In Figure B-5, for the viscosity the graph of defined piecewise-linear function is given.

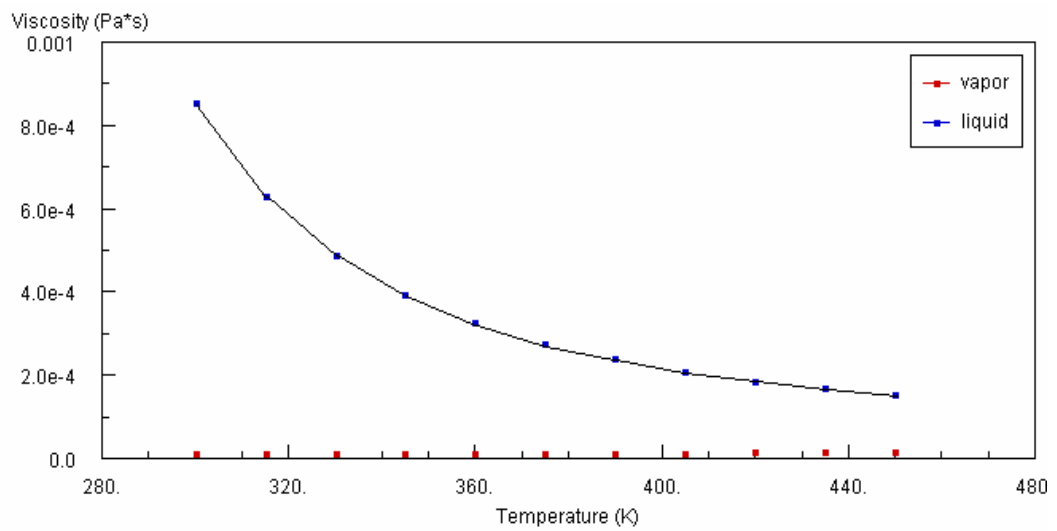


Figure B-5 Viscosity of water versus temperature (for ten intervals)
(adapted from [30])

APPENDIX C

DETAILS OF NON-UNIFORM VELOCITY PROFILE

In cylindrical coordinates velocity distribution in axial direction is given as [31]:

$$V_z = V_c \left(1 - \frac{r^2}{R^2} \right) \quad (\text{C.1})$$

where V_c is the velocity at the centerline of the pipe, R is the radius of the pipe and V_z is the velocity in the z-direction.

and volumetric flow rate through a pipe is defined by;

$$Q = \int_A V_z dA \quad (\text{C.2})$$

After integrating from 0 to R , and substituting Equation C.1 into Equation C.2;

$$Q = \int_0^R 2\pi r V_z dr = 2\pi V_c \int_0^R \left(1 - \frac{r^2}{R^2} \right) r dr \quad (\text{C.3})$$

From Equation C.3, resulting equation between volumetric flow rate, and the centerline velocity of the pipe is given by following equation:

$$Q = \frac{\pi R^2 V_c}{2} \quad (\text{C.4})$$

Using Equation C.4, V_c is calculated as: 0.189 m/s.

Therefore, fully developed, laminar velocity profile for the inlet nozzle is given by following equation:

$$V_z = 0.189 \left(1 - \frac{r^2}{0.075^2} \right) \quad (\text{C.5})$$

The theoretical graph in the Figure 4-7 is drawn by using Equation C.5.

APPENDIX D

SAMPLE HEAT TRANSFER COEFFICIENT CALCULATION

The heat transfer coefficient values are calculated as general heat exchanger theory available in the literature [26]. In this section, the heat transfer coefficient calculation for case A with mass flow rate 0.5 kg/s presented in Table 3-3.

Constant wall temperature is assumed for tube side; thus: $T_{h,i} = T_{h,o} = 450$ K

For shell side $T_{c,i} = 300$ K and from CFD analysis $T_{c,o} = 321.76$ K

$$\Delta T_1 = T_{h,i} - T_{c,o} = 128.24 \text{ K} \quad (\text{D.1})$$

$$\Delta T_2 = T_{h,o} - T_{c,i} = 150 \text{ K} \quad (\text{D.2})$$

Bulk mean temperature, which is the average temperature of ΔT_1 & ΔT_2 is used since tube side temperatures are taken from directly tube wall temperature.

$$\Delta T_m = (\Delta T_1 + \Delta T_2) / 2 = 139.12 \text{ K} \quad (\text{D.3})$$

From general heat exchanger theory available in the literature, using $q = 76950$ W and $A = 0.26$ m²

$$q = UA\Delta T_m \longrightarrow U = \frac{q}{A\Delta T_m} = 2127 \text{ W/m}^2\text{K} \quad (\text{D.4})$$

APPENDIX E

SAMPLE ANALYTICAL CALCULATIONS

In this section detailed sample calculations of Kern method and Bell-Delaware method are explained.

For clean heat exchanger (no fouling), the overall heat transfer coefficient is given by;

$$\frac{1}{U} = \frac{1}{h_o} + \frac{d_o}{d_i} \frac{1}{h_i} + d_o \frac{\ln(d_o/d_i)}{k} \quad (\text{E.1})$$

In overall heat transfer coefficient calculation, tube side heat transfer coefficient is assumed relatively high than shell side, since tube walls are at the same temperature. Also, tube materials thermal conductivity is assumed to be high. Therefore, the overall heat transfer coefficient equation can be simplified as follows; considering only tubes outside surface for heat transfer area.

$$\frac{1}{U} = \frac{1}{h_o} \quad (\text{E.2})$$

E.1 Kern Method Analysis

Sample Kern method analysis is performed for case A in Table 3-4 (for mass flow rate 0.5 kg/s). The properties are evaluated at the average fluid temperature in the shell.

Equivalent diameter is given by following equation;

$$D_e = \frac{4 \times \text{free-flow area}}{\text{wetted perimeter}} \quad (\text{E.3})$$

and for triangular pitch D_e is given by;

$$D_e = \frac{4\left(\frac{P_T^2 \sqrt{3}}{4} - \frac{\pi d_o^2}{8}\right)}{\pi d_o / 2} = 0.0296 \text{ m} \quad (\text{E.4})$$

The tube clearance is given by;

$$C = P_T - d_o = 0.01 \text{ m} \quad (\text{E.5})$$

The bundle cross-flow area A_s at the center of the shell is;

$$A_s = \frac{D_s C B}{P_T} = 0.00258 \text{ m} \quad (\text{E.6})$$

The shell side mass velocity is found with following equation;

$$G_s = \frac{\dot{m}}{A_s} = 193.8 \text{ kg/m}^2\text{s} \quad (\text{E.7})$$

Shell side Reynolds number is given by following equation;

$$\text{Re} = \frac{G_s D_e}{\mu} = 8401 \quad (\text{E.8})$$

For shell side heat transfer coefficient, McAdams correlation is used;

$$\frac{h_o D_e}{k} = 0.36 \left(\frac{D_e G_s}{\mu} \right)^{0.55} \left(\frac{c_p \mu}{k} \right)^{1/3} \left(\frac{\mu}{\mu_w} \right)^{0.14} = 98.54 \quad (\text{E.9})$$

Equation E.9 is valid for;

$$\text{for } 2 \times 10^3 < \text{Re} = \frac{D_e G_s}{\mu} < 1 \times 10^6 \quad (\text{E.10})$$

Therefore; from Equation E.9 shell side heat transfer coefficient is calculated as:

$$h_o = 2076 \text{ W/m}^2\text{K}$$

From Equation E.2 heat transfer coefficient for case A with mass flow rate 0.5 kg/s is calculated as;

$$h_o = U = 2076 \text{ W/m}^2\text{K} \quad (\text{E.11})$$

E.2 Bell-Delaware Method Analysis

Similarly, sample Bell-Delaware analysis is performed for case A in Table 3-4 (for mass flow rate 0.5 kg/s).

E.2.1 Additional Bell-Delaware Method Definitions:

The tube layout is defined by the characteristic angle and for current study it is $\theta_{tp} = 30^\circ$ [4].

Segmental baffle, B_c cut is defined as ratio of baffle cut to D_s and for current model $B_c = 0.36\%$.

Shell to baffle clearance L_{sb} and clearance between tube outside diameter and baffle hole L_{tb} values are taken as zero, since, in the model these clearances are neglected because of the size of the model. Thus, tube to baffle hole leakage area for one baffle S_{tb} and shell to baffle leakage area S_{sb} are zero.

L_{bb} , shell diameter to tube bundle bypass clearance is (diametral) 10mm in the model.

The diameter of the circle through the centers of the tube located within the outermost tubes; D_{ctl} is;

$$D_{ctl} = D_s - (L_{bb} - d_o) = 0.06 \text{ m} \quad (\text{E.12})$$

The tube bundle circumscribed circle, D_{otl} , is defined as;

$$D_{otl} = D_s - L_{bb} = 0.08 \text{ m} \quad (\text{E.13})$$

The cross flow area at the centerline of the shell for one cross flow between two baffles, A_s is defined as;

$$A_s = (D_s - N_{tc} \cdot d_o)B = 2.58 \cdot 10^{-3} \text{ m}^2 \quad (\text{E.14})$$

where N_{tc} is number of tubes in cross-flow, and has a value of 3.

E.2.2 Bell-Delaware Method Calculations:

Cross flow area S_m at the shell centerline with one baffle is defined with following equation; where $P_{Teff} = P_{Tr}$, since the tube layout is triangular.

$$S_m = \left[L_{bb} + \frac{D_{ctl}}{P_{Teff}} (P_T - d_o) \right] = 2.58 \cdot 10^{-3} \text{ m}^2 \quad (\text{E.15})$$

Average temperature of the shell-side is;

$$T_{sav} = \frac{1}{2} (T_{si} + T_{so}) = 310.88 \text{ K} \quad (\text{E.16})$$

Shell-side Reynolds number is defined as;

$$\text{Re} = \frac{d_o G_s}{\mu} = 5675 \quad (\text{E.17})$$

where the maximum shell-side cross flow mass velocity, G_s is defined by;

$$G_s = \frac{m}{S_m} = 193.8 \text{ kg/m}^2\text{s} \quad (\text{E.18})$$

The effective mean temperature difference is defined by following equation;

$$\Delta T_m = \Delta T_{lm} F = 138.83 \text{ K} \quad (\text{E.19})$$

where F is the correction factor, and equal to 1 for the current model [2].

Total heat transfer surface of the heat exchanger is;

$$A_o = \pi d_o L N_t = 0.264 \text{ m}^2 \quad (\text{E.20})$$

The centri-angle of the baffle cut intersection with the inside shell wall, θ_{ds} can be expressed as;

$$\theta_{ds} = 2 \arccos(1 - 2B_c) = 147.75^\circ \quad (\text{E.21})$$

The angle intersecting the circle through the centers of the outermost tubes, θ_{ctl} is defined as;

$$\theta_{ctl} = 2 \arccos \left[\frac{D_s}{D_{ctl}} (1 - 2B_c) \right] = 130.75^\circ \quad (\text{E.22})$$

The gross window flow area, that is, without tubes in the window is defined as;

$$S_{wg} = \frac{\pi}{4} D_s^2 \left[\theta_{ds} - \frac{\sin(\theta_{ds})}{2\pi} \right] = 2.07 \cdot 10^{-3} \text{ m}^2 \quad (\text{E.23})$$

The fraction of number of tubes in one baffle window; $F_w = 2/7 = 0.286$.

F_c is the fraction of number of tubes in pure cross flow between the baffle cut tips, and can be expressed as;

$$F_c = 1 - 2F_w = 0.429 \quad (\text{E.24})$$

N_{tw} is the number of tubes in the window, and it is equal to 2.

S_{wt} the segmental baffle window area occupied by the tubes is defined by;

$$S_{wt} = N_{tw} \left[\frac{\pi}{4} d_o^2 \right] = 6.28 \cdot 10^{-4} \text{ m}^2 \quad (\text{E.25})$$

Thus, net cross flow area through one baffle window is;

$$S_w = S_{wg} - S_{wt} = 1.44 \cdot 10^{-3} \text{ m}^2 \quad (\text{E.26})$$

N_{icc} the number of effective rows crossed in one cross flow section is 1 tube rows.

And L_{wp} the effective distance of penetration is;

$$L_{wp} = 0.4 \left[D_s B_c - \frac{D_s - D_{ctl}}{2} \right] = 7 \cdot 10^{-3} \text{ m} \quad (\text{E.27})$$

So, N_{icw} the effective number of tube rows crossed is expressed as;

$$N_{icw} = 2L_{wp} / P_p = 0.539 \quad (\text{E.28})$$

where $P_p = 0.866 P_T$ for triangular pitch.

The bypass area within one baffle, S_b is;

$$S_b = B(D_s - D_{otl}) = 8.6 \cdot 10^{-4} \text{ m}^2 \quad (\text{E.29})$$

F_{sbp} , the fraction of the bypass area to the overall cross flow area is expressed as;

$$F_{sbp} = S_b / S_m = 0.333 \quad (\text{E.30})$$

E.2.3 Correction Factors:

Segmental baffle window correction factor, J_c is;

$$J_c = 0.55 + 0.72F_c = 0.859 \quad (\text{E.31})$$

Correction factors for baffle leakage effects for heat transfer, J_l , and pressure drop R_l is one, since, there is no leakage through baffles.

Correction factors for bundle bypass effects for heat transfer, J_b , and pressure drop, R_b are calculated as follows:

$$J_b = \exp\left[-C_{bh}F_{sbp}\left(1 - (2r_{ss})^{1/3}\right)\right] = 0.659 \quad (\text{E.32})$$

$$R_b = \exp\left[-C_{bp}F_{sbp}\left(1 - (2r_{ss})^{1/3}\right)\right] = 0.291 \quad (\text{E.33})$$

where $C_{bh} = 1.35$ and $C_{bp} = 3.7$ for turbulent flow, and r_{ss} is equal to zero, when there is no sealing strip.

Heat transfer correction factor for adverse temperature gradient in laminar flow, J_r is equal to one for turbulent flow.

Heat transfer correction for unequal baffle spacing at inlet and outlet, is calculated as follows;

$$J_s = \frac{(N_b - 1) + L_i^{1-n} + L_o^{1-n}}{(N_b - 1) + L_i + L_o} = 1.002 \quad (\text{E.34})$$

where L_i is the ratio of inlet baffle spacing to central baffle spacing and L_o is the ratio of outlet baffle spacing to central baffle spacing.

R_s , pressure drop correction factor for unequal baffle spacing at inlet and outlet is expressed as;

$$R_s = (L_o)^{n-2} + (L_i)^{n-2} = 2.043 \quad (\text{E.35})$$

where $n = 0.2$ for turbulent flow.

E.2.4 Calculation of Shell-Side Heat Transfer Coefficient and Pressure Drop:

The ideal tube bank-based heat transfer coefficient can be calculated from;

$$h_{id} = j_i c_{ps} \left(\frac{m_s}{A_s} \right) \left(\frac{k_s}{c_{ps} \mu_s} \right)^{2/3} \left(\frac{\mu_s}{\mu_{sw}} \right)^{0.14} = 3726 \text{ W/m}^2\text{K} \quad (\text{E.36})$$

The shell side heat transfer coefficient;

$$h_o = h_{id} (J_c J_1 J_b J_s J_r) = 2113 \text{ W/m}^2\text{K} \quad (\text{E.37})$$

For a shell-and-tube type heat exchanger, the pressure drop is calculated as the sum of the following four components; pressure drop in interior cross flow section

Δp_{cr} , pressure drop in the window Δp_{wr} , pressure drop in the entrance and exit sections Δp_e and nozzle pressure drop Δp_n .

Pressure drop in interior cross flow section, Δp_c is calculated by using the pressure drop in an equivalent ideal tube bank in one baffle compartment of central baffle spacing, Δp_{bi} .

$$\Delta p_{bi} = 4f_i \frac{G_s^2}{2\rho_s} \left(\frac{\mu_{sw}}{\mu_s} \right)^{0.14} = 107 \text{ Pa} \quad (\text{E.38})$$

$$\Delta p_c = \Delta p_{bi} (N_b - 1) R_l R_b = 156 \text{ Pa} \quad (\text{E.39})$$

In Equations E.36 and E.38, j_i is the Colburn j -factor and f_i is the friction coefficient for an ideal tube bank. Although ideal values of j_i and f_i are available in graphic forms and a set of curve fit correlations. j_i and f_i are calculated by using curve fit correlations presented in Kakaç and Liu [2].

For turbulent flow, pressure drop in the window, Δp_w can be expressed as;

$$\Delta p_w = N_b \left[(2 + 0.6N_{tcw}) \frac{m_w^2}{2\rho_s} \right] R_l = 472 \text{ Pa} \quad (\text{E.40})$$

where m_w is the shell-side flow mass velocity through segmental baffle window, which is equal to m_s .

Pressure drop in the entrance and exit sections, Δp_e can be expressed as;

$$\Delta p_e = \Delta p_{bi} \left[1 + \frac{N_{tcw}}{N_{tcc}} \right] R_b R_s = 99 \text{ Pa} \quad (\text{E.41})$$

Finally, nozzle pressure drop Δp_n , is defined by [16];

$$\Delta p_n = \rho_s u_n^2 = 504 \text{ Pa} \quad (\text{E.42})$$

where u_n is the average velocity at the nozzle.

Therefore total shell side pressure drop is;

$$\Delta p_t = \Delta p_c + \Delta p_w + \Delta p_e + \Delta p_n = 1231 \text{ Pa} \quad (\text{E.43})$$

APPENDIX F

DOUBLE PIPE CALCULATIONS

In this section detailed sample calculations for double pipe heat exchanger is discussed. The properties are evaluated at the average fluid temperature for the annulus side and the tube side. Sample analysis is performed for case B-1 in Table 3-17.

F.1 Detailed Tube Side Analysis

The velocity in the tube side is given by following equation;

$$u_m = \frac{m_h}{\rho A_c} = 0.657 \text{ m/s} \quad (\text{F.1})$$

Corresponding tube side Reynolds number is;

$$\text{Re} = \frac{\rho u_m d_i}{\mu} = 88499 \quad (\text{F.2})$$

Hence the flow is turbulent; Prandtl's correlation is used here with constant properties.

$$\text{Nu} = \frac{(f/2)\text{RePr}}{1 + 8.7(f/2)^{1/2}(\text{Pr}-1)} = 308.14 \quad (\text{F.3})$$

where friction factor is defined by;

$$f = (1.58 \ln(\text{Re}) - 3.28)^{-2} = 0.00462 \quad (\text{F.4})$$

And tube side heat transfer coefficient is;

$$h_i = \frac{Nu \cdot k}{d_i} = 3944 \text{ W/m}^2\text{K} \quad (\text{F.5})$$

The frictional pressure drop in the tube side is given by;

$$\Delta p_f = 4f \left(\frac{L}{d_i} \right) \rho \left(\frac{u_m^2}{2} \right) = 89.67 \text{ Pa} \quad (\text{F.6})$$

F.2 Detailed Annulus Side Analysis

The velocity in annulus:

$$u_m = \frac{m_c}{\rho A_c} = 0.36 \text{ m/s} \quad (\text{F.7})$$

Hydraulic diameter and equivalent diameter for heat transfer for the annulus side are defined by;

$$D_h = \frac{4A_c}{P_w} = D_i - d_o = 0.018 \text{ m} \quad (\text{F.8})$$

$$D_e = \frac{D_i^2 - d_o^2}{d_o} = 0.0414 \text{ m} \quad (\text{F.9})$$

Following equation gives annulus side Reynolds number;

$$\text{Re} = \frac{\rho u_m D_h}{\mu} = 6675 \quad (\text{F.10})$$

Nusselt number for low Reynolds number ($2300 < Re_b < 10^4$) is defined as;

$$Nu = \frac{(f/2)(Re_b - 1000)Pr_b}{1 + 12.7(f/2)^{1/2}(Pr_b^{2/3} - 1)} = 53.38 \quad (\text{F.11})$$

where friction factor is defined by;

$$f = (1.58 \ln(Re) - 3.28)^{-2} = 0.008844 \quad (\text{F.12})$$

And annulus side heat transfer coefficient is;

$$h_o = \frac{Nu \cdot k}{D_e} = 775.28 \text{ W/m}^2\text{K} \quad (\text{F.13})$$

The frictional pressure drop in the annulus is given by following equation;

$$\Delta p_f = 4f \left(\frac{2L}{D_h} \right) \rho \left(\frac{u_m^2}{2} \right) = 152.15 \text{ Pa} \quad (\text{F.14})$$

From Kapale and Chand's work; pressure drop in inlet and outlet nozzles is given by following equation [16];

$$\Delta p_n = \rho \cdot u_n^2 = 982.89 \text{ Pa} \quad (\text{F.15})$$

In Equation F.15, u_n is the average nozzle velocity, and defined by;

$$u_n = \frac{m_s}{\rho A_n} = 0.993 \text{ m/s} \quad (\text{F.16})$$

And total pressure drop in the annulus side is the sum of frictional pressure drop and nozzle pressure drop.

$$\Delta p_t = \Delta p_f + \Delta p_n = 1135 \text{ Pa} \quad (\text{F.17})$$

F.3 Overall Heat Transfer Coefficient Calculation

Assuming no fouling in the heat exchanger, overall heat transfer is calculated by the following equation:

$$\frac{1}{U_o} = \frac{d_o}{d_i h_i} + \frac{1}{h_o} + d_o \frac{\ln(d_o/d_i)}{2k} = 601 \text{ W/m}^2\text{K} \quad (\text{F.18})$$

F.4 Total Heat Transfer Rate Calculation

The log mean temperature difference (LMTD) is defined as the logarithmic average of the temperature differences between the hot and the cold streams at each end of the exchanger. For counter-flow arrangement LMTD is defined by;

$$\Delta T_{lm} = \frac{\Delta T_2 - \Delta T_1}{\ln(\Delta T_2 / \Delta T_1)} \quad (\text{F.19})$$

ΔT_2 and ΔT_1 are the temperature differences at each end of the heat exchanger;

$$\Delta T_1 = T_{h,i} - T_{c,o} = 52.9 \quad (\text{F.20})$$

$$\Delta T_2 = T_{h,o} - T_{c,i} = 54.19 \quad (\text{F.21})$$

Thus, $\Delta T_{lm} = 53.54 \text{ K}$

From general heat exchanger theory available in the literature, total heat transfer rate is calculated as;

$$q = UA\Delta T_{lm} = 7287 \text{ W} \quad (\text{F.22})$$